OXIDATION BEHAVIOUR OF AUSTENITIC STAINLESS STEELS AT HIGH TEMPERATURE IN SUPERCRITICAL PLANT

by

HENRY GEORGE SIMMS

A thesis submitted to

The University of Birmingham

For the degree of

MASTER OF RESEARCH

School of Metallurgy and Materials Engineering

College of Engineering and Physical Science

The University of Birmingham

April 2011

Abstract

Fossil power plant efficiency is improved by increasing steam temperature and pressure. Current martensitic and ferritic steels do not have the required oxidation and spallation properties for boiler tube applications as service conditions increase. Spallation inside the tube can lead to blockage, overheating, creep rupture and turbine erosion. The current steels are limited to 620^{o}C, therefore austenitic stainless steels are proposed for boiler tube applications to enable higher operating conditions. This investigation compared the oxidation and spallation behaviour of the current martensitic steels (T91, T92) with the proposed austenitic stainless steels (super 304H, shot peened super 304H, 347HFG), in air at 600-700^{o}C. Oxide morphology was characterised using SEM and EDX analysis and oxidation kinetics were recorded using specific mass gain and oxide thickness measurements over time. The martensitic steels formed non-protective Fe-rich oxides, which consistently spalled on cooling. The austenitic stainless steels showed little spallation and less mass gain compared to the T92 steel. Double-layered oxides formed on the super 304H and 347H FG steels consisting of an inner protective Cr-rich spinel oxide and an outer Fe-rich oxide. Shot peening increased the oxidation resistance of the super 304H steel forming significantly thinner, single-layer Cr-rich oxides with less mass gain.

Contents

1. Introduction

1.1. Industrial Practice for Power Generation – Steam Plants

Unlike other fossil fuels, there are no imminent dangers of running out of coal and it will remain a vital workhorse for energy generation well beyond the first half of the 21st century. In the UK 74% of the electricity demand is met by fossil-fuelled plants (38% coal- or oil-fired and 36% gas-fired) [1]. Of the gas-fired plants half are combined cycle (i.e., gas turbine + steam turbine), therefore making >50% of UK electricity generation dependent on steam plant [1]. The efficiency of conventional fossil power plants is a strong function of increased steam parameters (i.e., temperature and pressure), with the steam referred to as supercritical when reaching temperatures of 538-565^{o}C and exceeding pressures of 22MPa in the main steam line. Increasing the temperature and pressure in a steam turbine increases the efficiency of the Rankine steam cycle used in power generation. Current state-of-the-art plants in the UK operating at a steam temperature of 565°C and a steam pressure of 17 MPa have a thermal efficiency of approximately 35%. An increase in plant efficiency from 35% to 50% is estimated to decrease CO_2 emissions by 30% [2]. This can be achieved by increasing the service conditions to pressures of 30 MPa and temperatures up to 600-650ºC [3]. Other countries are already starting to build higher efficiency coal plants operating at 600-620^{o}C. Considering the thousands of coal-fired power plants that India and China will build in the coming decades (e.g., China, in 2006 alone, built more electric power plants than the total installed capacity of Great Britain), the global impact that may occur when conventional power plants become nearly twice as efficient is substantial, perhaps cutting green house emissions to levels needed to offset the higher consumption of fuel.

Increasing the efficiency to 60% using ultra-supercritical steam (above 565^{o}C and 27.5MPa in the main steam line) requires a significant increase in operating temperatures and pressures. Long-term research programmes such as USC in the US and THERMIE in Europe target 800°C and 35-39 MPa operating conditions [4]. These operating conditions require new materials that can withstand these extreme temperature and pressure environments. Current ferritic and martensitic steels do not have the required mechanical properties at these temperatures, particularly creep rupture strength and thermal fatigue [5]. Although materials

for these applications are primarily designed on creep properties, oxidation and spallation are key performance parameters in boiler tube applications due to temperature and pressure increases in service conditions that are already extremely harsh. Boiler tube steels have three main requirements; a need for tolerance to all stages of the fabrication process including welding, a need for adequate creep strength, and a need for sufficient fireside corrosion and steam side oxidation resistance [6]. Spallation of a formed steam side oxide can have severe adverse effects such as collection of the spalled material in the bottom of tube bends, leading to blockage, overheating and premature creep rupture as well as transportation of the oxide through the system to the main steam valves and turbine, resulting in erosion damage [7, 8]. Fast scale formation can also lead to the consumption of the steel walls until the load bearing section is reduced and mechanical failure occurs [9]. The main cause of oxide spallation is due to the stresses induced by a temperature drop. This drop in temperature can be due to intermittent service or thermal cycling of the tubes. To reduce the impact of spallation at higher service temperatures these plants should be used for continuous service. Where cyclic service conditions are expected lower peak service temperatures should be used [9]. The mechanism responsible is the build up of internal stresses in the oxide layer due to a difference in thermal expansion coefficients between the different oxide layers and the substrate. However, creep can partly relax these stresses if the cooling rate is low enough [10].

Although improvements continue due to alloying additions, currently available ferritic and martensitic steels will be limited to use at temperatures up to 620°C. The oxidation and hot corrosion behaviour of these alloys in steam limit their temperature of operation as there are no obvious routes for improvement that will not invalidate the compositional restrictions set by the strengthening requirements [7]. Improved understanding of the oxidation and spallation mechanisms in steam is necessary for lifing and progressive degradation assessment of existing materials as well as for future alloy design.

Austenitic steels are currently being used in the highest temperature regions of superheaters and reheaters in conventional stations. There has been a history of spallation events in martensitic steels over many years leading to tube failures. Stations recently built in China operating at higher steam temperatures [11] have reported oxide spallation and tube blockages. With increasing service temperatures (600^{o}C and upwards) more austenitic stainless steel

tubing will be used in superheater and reheaters and more emphasis will be placed on the need for oxidation/corrosion resistance over increased mechanical strength. These higher chromium stainless steels will enable higher operating temperatures beyond the ferritic/martensitic steels' limit, thus allowing the plant to work at higher steam parameters, leading to increased efficiency.

1.2. Project Scope

In this project the oxidation resistance of two candidate austenitic stainless steels (i.e., 304H and 347HFG) will be tested extensively in laboratory air conditions at a temperature range of 600-700^{o}C. Results will subsequently be compared to the previous ferritic/martensitic steels (i.e., T91, T92) that are currently in use.

Therefore the main aims for this project are to;

1) Test the oxidation resistance of selected austenitic alloys in air by recording oxide growth and the spallation activity during and after high temperature exposure.
2) Record the oxide morphology using cross section analysis involving SEM and EDX testing.
3) Record the oxidation kinetics using mass gain and oxide thickness measurements over selected durations.
4) Compare all of the stated oxidation behaviour with that of the alloys currently in use.

2. Literature Review

2.1. Physical Metallurgy of Stainless Steels for Use in High Temperature Plants

2.1.1. The Effect of Alloying Additions on Microstructure and Properties of Stainless Steel

The key materials properties for boiler tubes in power generation are high temperature strength and good corrosion resistance. Optimisation of these properties ensures that these steel components do not fail under working conditions. Although the use of steels is very common in boiler tube applications, additions of varying amounts of different alloying elements provide a range of these required properties in the extreme environments of the application.

2.1.1.1. Austenite Stabilisers

Nickel and manganese are added to steels to stabilise the face centred cubic austenitic structure and they guarantee complete austenitic formation during the austenisation treatment [12, 13]. The addition of chromium alone to a plain carbon steel causes ferrite to form [12]. It should be noted that nickel also accelerates the coarsening of the precipitates causing the long term creep strength to decrease. Manganese is not as strong as nickel at stabilising the austenite but it has the same effect on coarsening of the carbides and reducing the creep strength. They both have a strong solid solution strengthening effect in iron as well [13]. Copper also has an austenitic stabilising effect although its main purpose in the alloy is to improve the creep strength [13]. In type 347H FG the structure is also stabilised by tantalum and niobium additions for service at high temperatures [9]. This austenitic structure is important as these steels are readily fabricated and unlike ferritic steels, they do not undergo the undesirable ductile/brittle transition [12].

2.1.1.2. Solid Solution Strengthening

Nitrogen is added to the stainless steel to increase the tensile strength of the alloy through solid solution strengthening. In service the nitrides can precipitate, which reduces dissolved

nitrogen in the austenitic matrix decreasing the solid solution strengthening [14]. While the formation of nitrides and carbides during service is beneficial for creep resistance, niobium carbonitride phases also precipitate during service helping to strengthen the alloy. Niobium is also a strong and stable carbide and nitride former. Un-dissolved niobium carbides are often wanted as they restrict grain growth during austenisation of the alloy which is desirable for reasons discussed later [13]. For these to dissolve completely they have to be heated above austenising temperatures [13]. Some carbides form on grain boundaries increasing the boundary strength [14]. The formation of chromium carbides causes a depletion of chromium in the matrix reducing the oxidation resistance [13, 15]. In austenitic steels, carbon and nitrogen have high solubility and act as strong austenite stabilisers [13]. Carbon is also added for its solid solution strengthening effect to restrict the movement of dislocations in the metal [16]. Phosphorus is also involved in increasing the hardenability. It segregates to the carbide surface or is integrated in them which slows down the coarsening rate of the carbide stabilising the microstructure [13].

2.1.1.3. Creep Strength

Type 304H austenitic stainless steel is used in conventional power plant where metal temperatures are below 600^{o}C. However, creep resistance of standard 304H is not good enough for temperatures above 600^{o}C in power generation applications. Therefore, copper and other alloying additions of up to 3 wt% are included in the composition to improve the creep strength [13, 14]. This new alloy design is called ‘super 304H’ and its improved creep strength is also due to increased carbon content and certain amounts of niobium and nitrogen which are added. An alternative method of increasing the creep strength is increasing the nickel content, but this also increases the cost of the alloy considerably and so is not desirable [14]. Copper improves the creep strength by the precipitation of the copper rich phase in the matrix during service reducing the motion of dislocations via precipitation hardening. The precipitation of this phase is accompanied by the precipitation of a niobium carbonitride phase [14]. During long term service of the steel, the copper rich precipitates coarsen which means their strengthening effect is reduced. The copper rich precipitates have a critical diameter of around 30 nm after which they are no longer coherent with the austenitic matrix and the creep strengthening is less effective. So the aim is to avoid this effect in service and from this an optimum copper addition of 3 wt% is achieved [14]. Type 347H FG is stabilised with niobium

which can be heat treated to produce NbC carbides which improve creep strength by interacting with dislocations produced throughout creep [12]. Type 304H and 347H FG also contain carbon contents higher than 0.04wt% which enable elevated and reproducible creep rupture strength at high temperatures [9].

2.1.1.4. Oxidation Resistance

The chromium content in the alloy is extremely important for improving the oxidation/corrosion resistance of the steam side of the pipe [13-15, 17], by the formation of a protective, adherent, slow growing Cr_2O_3 (chromia) oxide layer [14]. This oxide is slow growing and blocks the outward diffusion of other alloy elements and the inward diffusion of gaseous impurities [18] as transport processes through this scale are generally slow [19]. The outward diffusion of chromium (Cr^{3+}) along grain boundaries has shown to be faster than the inward diffusion of oxygen by a factor of three and so the chromia scale usually grows outward [20] and can contain small amounts of iron, nickel and manganese [9] as seen on high chromium steels such as 310. Chromium content is important in dictating the oxide formed, lower chromium concentrations e.g. type 304, form the spinel oxide $FeCr_2O_4$ which can be protective to a lesser extent [9]. The greater the chromium content in the alloy the greater its oxidation resistance is [15]. Steels with a chromium content of over 13 wt% show very low oxidation rates and their scales consist of Cr_2O_3, $(Cr, Fe)_2O_3$ or Cr rich $(Cr, Fe\ Mn)_3O_4$ with an outer layer of Fe_2O_3 [21]. However, at temperatures exceeding 900^{o}C, chromia scales can react further with oxygen to form CrO_3 which is a volatile species [19].

Silicon additions are also well known for enhancing the oxidation resistance of stainless steels with the lower silicon concentrations having the highest corrosion rates [9, 15, 21, 22]. This effect has been explained by suggestions such as the formation of the initial chromia layer being facilitated by silicon, or the formation of silica particles beneath the chromia layer which increase the adhesion of the chromia layer, or the formation of a continuous silica layer beneath the chromia preventing outward diffusion of chromium ions [9]. The additions of both chromium and silicon at optimum levels will improve oxidation resistance without adversely affecting the creep strength [15]. The influence of silicon is enhanced at higher temperatures, i.e. above 700°C [15].

Manganese is also an alloying addition seen to affect oxidation resistance, but its effect has been measured both favourably and adversely [15, 23]. In some cases it has been found to be damaging to the oxidation resistance of austenitic stainless steels due to it forming a spinel oxide of $MnO{\cdot}Cr_2O_3$ rather than the protective chromia oxide [23]. Nickel has also been shown to enhance the oxidation resistance by reducing the cation diffusion in the Cr_2O_3 scale and preventing the formation of $FeCr_2O_4 + Fe_2O_3$, having an influence on the adhesion and mechanical properties of the scale [9]. It is very difficult to consider these alloying elements separately due to their complex interactions.

2.1.1.5. Summary of Alloying Addition Functions

The various alloying additions and their role in steel is summarised in table 2.1. All of the alloying elements are added to optimise the steel's properties so that they do not fail in service.

Table 2.1. Review of alloying addition functions.

Alloying Element	Function
Nickel	Stabilises the austenitic structure during the austenisation treatment.
Manganese	Stabilises the austenitic structure during the austenisation treatment.
Nitrogen	Increases the tensile strength through solid solution strengthening.
Niobium	Stabilises carbon and improves the creep strength by forming NbC carbides.
Carbon	Increases the tensile strength through solid solution strengthening.
Copper	Improves the creep strength by the precipitation of a copper rich phase. Also has an austenitic stabilising effect.
Chromium	Improves the oxidation/corrosion resistance. Resistance increases with increasing chromium content.
Silicon	Improves the oxidation/corrosion resistance.
Phosphorus	Involved in increasing hardenability and strength.

2.1.2. The Effect of Surface Modification on Physical Structure

2.1.2.1. Grain Refinement

The grain size also influences the oxidation resistance of the alloy. Short circuit diffusion of ions along the grain boundaries is a lot quicker than through the grains themselves [14, 16, 19, 24-26]. Reducing the grain size increases the grain boundary density which in turn increases the rate at which chromium ions can diffuse through the alloy [27]. This leads to the early formation of the Cr_2O_3 oxide layer, slowing down further growth of the oxide layer due to its low permeability [14] [26]. A study on 304 stainless steel in wet air revealed catastrophic breakaway oxidation on coarse grained samples due to the formation of a non-protective iron-rich scale; samples with fine grain structure did not show breakaway oxidation due to the dense network of grain boundaries increasing the chromium diffusion which promoted stable growth of the protective chromium-rich scale [26]. A study in laboratory air of TP347 showed a similar grain size effect; Cr_2O_3 formed on the fine grained variant but the coarse grained equivalent formed non-protective iron based oxides [24]. Grain refinement is an alternative method to adjusting alloy composition to help protect against oxidation [26] and also increases the strength by impeding the motion of dislocations [16].

2.1.2.2. Shot Peening

Another technique used to increase the oxidation resistance of the stainless steels is a surface modification technique called shot peening [9, 14]. This method involves inducing compressive stresses in the surface via impact of peening beads [28]. This treatment causes the grain boundary density and twin boundaries near the surface (~50μm) to increase through cold deformation [14]. The grains are refined via dislocations from sub-micron to nano-sized grains [28]. As with the grain refinement method, this increases the chromium diffusion to the surface to produce a protective Cr_2O_3 oxide scale [9, 14, 29]. A study by Tan et al. in 2008 [28] also showed the shot peening treatment to improve oxidation resistance. In this study alloy 800H displayed improved oxidation resistance in supercritical water after shot peening. This was due to the shot peened surface having a deformed surface zone consisting of two microstructural regions; an ultra fine grained region at the surface and a transition region at the sub surface [28]. The shot peened samples had thinner oxide scales that mainly consisted of

chromia due to the enhanced chromium diffusion and less scale exfoliation was seen compared to the samples with no surface treatment [28]. Shot peening not only increases oxidation resistance but also increases fatigue life, hardness/durability, closing of porosity and stress corrosion cracking resistance [28].

2.2. General Principles of Oxidation in Air

2.2.1. Principles of Oxidation

The general chemical equation for an oxidation reaction between a metal (Me) and oxygen (O_2) is shown below.

$$aMe + b/2\ O_2 \rightarrow Me_aO_b \qquad \text{(Eq. 2.1)}$$

It is a simple equation but it depends on several factors and can become more intricate [30].

The first step in this metal-oxygen reaction involves the adsorption of gas on the clean metal surface. The adsorbed oxygen dissolves into the metal and the oxide forms as separate oxide nuclei or as a continuous oxide film. The solid reaction product (metal oxide) separates the two reactants, and for the reaction to continue further, one or both reactants have to penetrate the oxide layer (scale) by solid-state diffusion. This can happen by either oxygen going through to the oxide-metal interface and reacting there, or the metal being transported through the oxide to the oxide-gas interface and reacting there as shown in Figure 2.1 [31]. For thick compact scales, the reason for transport through the oxide is due to the chemical potential gradient across the scale, and for thin films it may be due to electric fields across the film. In porous oxides solid-state diffusion is limited and can be restricted to diffusion occurring at phase boundaries, or mass transport occurs through gas diffusion. Oxide layers at very high temperatures can also be volatile or liquid [30].

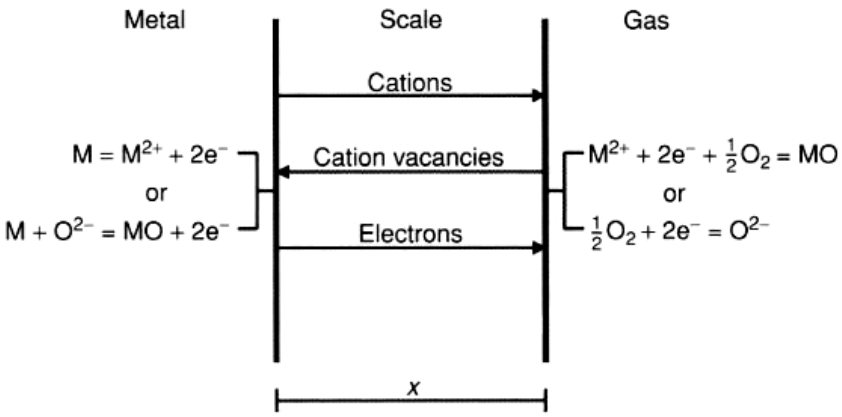

Figure 2.1. Schematic showing a simplified diffusion controlled process of oxidation where the cations and cation vacancies have to penetrate the oxide scale for the reaction to continue [31].

2.2.2. The Initial Stages of Oxidation

The adsorption of gas onto the metal surface is the very first stage of oxidation. This process involves a decrease in free energy and entropy which means enthalpy decreases and makes this process normally exothermic. There are two types of adsorption, chemical (chemisorption) and physical. Chemisorption involves the adsorbed species forming a chemical bond with surface atoms via the transfer of electrons. Physical adsorption involves physical or van der Waals forces bonding the gases to the surface and is reversible [32]. Chemisorption tends to take place at much higher temperatures and may involve an activation energy. Very rapid chemisorption can be seen with gases and clean metals where there appears to be no activation energy. It continues only until a monolayer of the adsorbent is created on the surface [30].

After the adsorption where the surface has been covered by chemisorbed oxygen, isolated oxide nuclei nucleate at random points for instance at impurity atoms, surface imperfections etc. on the metal surface. The growth of individual crystallites enables the oxidation of the surface to continue until oxide patches grown from individual nuclei connect and the entire surface is covered with oxide which acts as a diffusion barrier [17, 30].

2.2.3. Oxide Transport Mechanisms

The formed oxide separates the metal from the gas and the only way for oxidation to proceed is via solid-state diffusion of the reactants. This type of diffusion can only take place due to the presence of defects in the oxide structure. Point defects such as vacancies, interstitial atoms and misplaced atoms are required for solid-state diffusion in the oxide [17, 30]. Scale growth occurs by the diffusion of the cations and anions. Cation diffusion causes oxide formation at the oxide-gas interface and anion diffusion leads to oxide growth at the metal-oxide interface as shown in Figure 2.2. Oxides can show nonstoichiometry and either mainly contain cation defects or mainly contain oxygen defects.

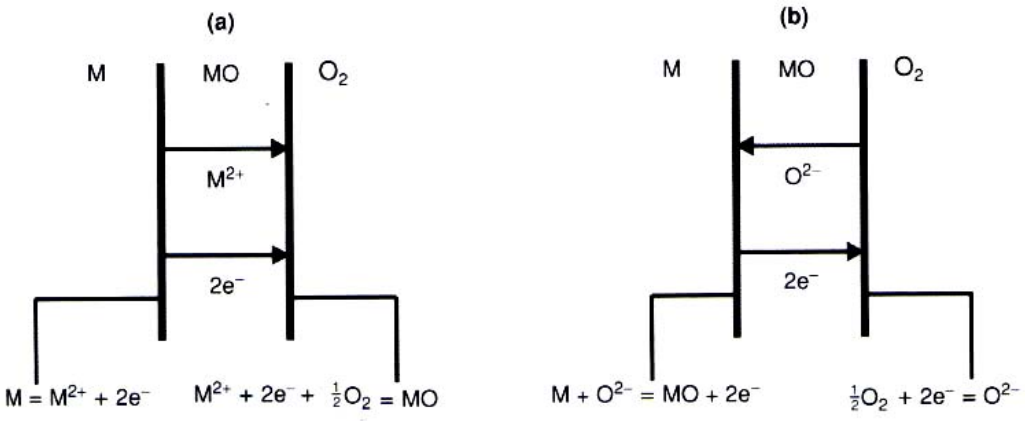

Figure 2.2. Schematic of high temperature oxidation mechanisms, showing the reactions at the metal interface and transport routes of ions where the cation is mobile (a) and the anion is mobile (b) [31].

2.2.4. Reaction Kinetics

The rate of oxidation can be measured experimentally by using three methods. These involve measuring the amount of oxygen consumed, the amount of metal consumed or the amount of oxide produced. The method used to find the amount of metal consumed is the least preferable as it is a destructive method which is indirect and not continuous. The method chosen in this project is to record the amount of oxide produced by weight change measurements and oxide thickness measurement. All of these variables are measured as a function of time to show the

rate of oxidation [31]. From experimental data three main rate laws have been observed as follows;

1.) The linear law: this is where the rate of reaction is constant with time and independent of the quantity of metal or gas consumed up to that time. The initial surface reaction step (adsorption) or the diffusion through the gas phase controls the oxidation process and is said to be rate determining. The linear rate law can be observed at the very initial stages of oxidation when the metal surface is exposed to the atmosphere for the first time. It can be described by the following equation,

$$x = k_l t \qquad \text{(Eq. 2.2)}$$

where x is the scale thickness, k_l represents the linear rate constant and t is the time [31].

2.) The parabolic law: this is where the rate of reaction is inversely proportional to the square root of time [31]. Many metals at high temperatures show this rate law where the diffusion of ions, either metal or gas, through the compact scale is the rate determining process [30]. The parabolic law can be described by the following equation,

$$x^2 = 2k't \qquad \text{(Eq. 2.3)}$$

where k′ is the scaling constant [31]. These two laws can be displayed graphically so the oxidation kinetics can be observed easily as shown in Figure 2.3.

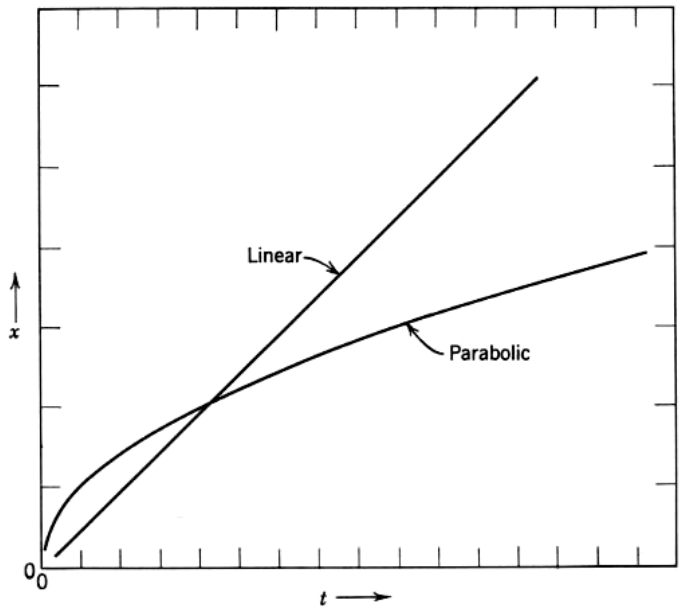

Figure 2.3. A graph showing linear and parabolic oxidation where oxide growth (x) is a function of time (t) [30].

3.) The logarithmic law: this is characteristic of the oxidation of a lot of metals at low temperatures (usually below 300-400^{o}C) and for the formation of very thin oxide films below tens of nm thick [32]. The reaction starts off rapidly and then slows down as it proceeds, this rate law can be described by two equations,

$$\text{Direct logarithmic: } x = k_{log} \log (t + t_0) + A \qquad \text{(Eq. 2.4)}$$

$$\text{Inverse logarithmic: } 1/x = B - k_{il} \log t \qquad \text{(Eq. 2.5)}$$

where k_{log} and k_{il} are rate constants and A and B are constants [30]. These laws can also be shown graphically as seen in Figure 2.4.

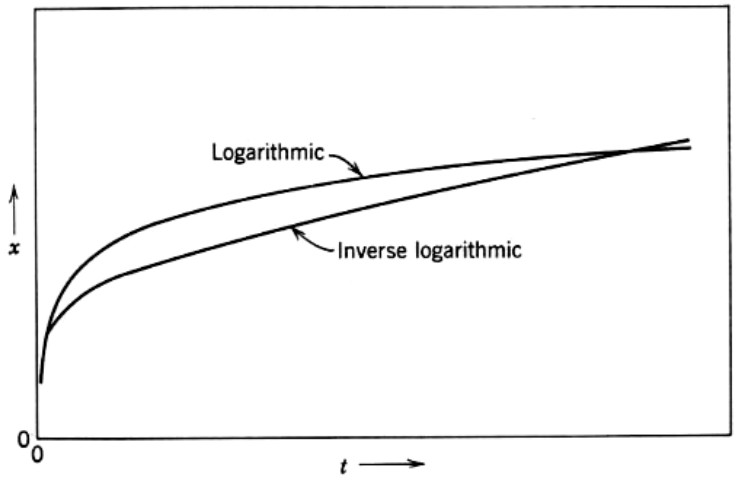

Figure 2.4. A graph showing the logarithmic and inverse logarithmic oxidation kinetics where oxide growth (x) is a function of time (t) [30].

Oxidation reactions often tend to follow a mixture of different rate laws as described above. This is due to the rate determining mechanisms changing during the reaction due to the scale itself changing or the reaction having concurrent mechanisms and one dominating at the start and then the other mechanism taking over later on [30]. An example of this is the transition from linear to parabolic law. The reaction starts off at constant rate when the oxide is just forming and is thin so diffusion through the film is very fast. Here the surface reaction is the rate determining mechanism. As oxidation continues and the scale becomes thicker there is less ion flux through the scale and the reaction rate decreases. The diffusion of ions through the oxide is now the rate determining step and the rate decreases as the reaction proceeds displaying the parabolic law [31].

The parabolic relationship is the most desirable as the oxide formed is slow growing and less likely to spall. This relationship is shown by curve OAD in Figure 2.5. However, depending on conditions (alloy composition, time and environment) breakaway oxidation can occur where there is a sudden increase in the growth rate shown by curve AB [9]. In the case of stainless steels, this is where iron rich oxides are forming instead of chromia due to alloy depletion as discussed later. The growth of oxide can continue shown by curve BE, possibly due to the environment where volatilisation of the oxide occurs, or from cracking in the scale

leading to additional outbursts of quick oxidation [9]. Alternatively, the oxidation rate can decrease again, BC, if a protective oxide reforms.

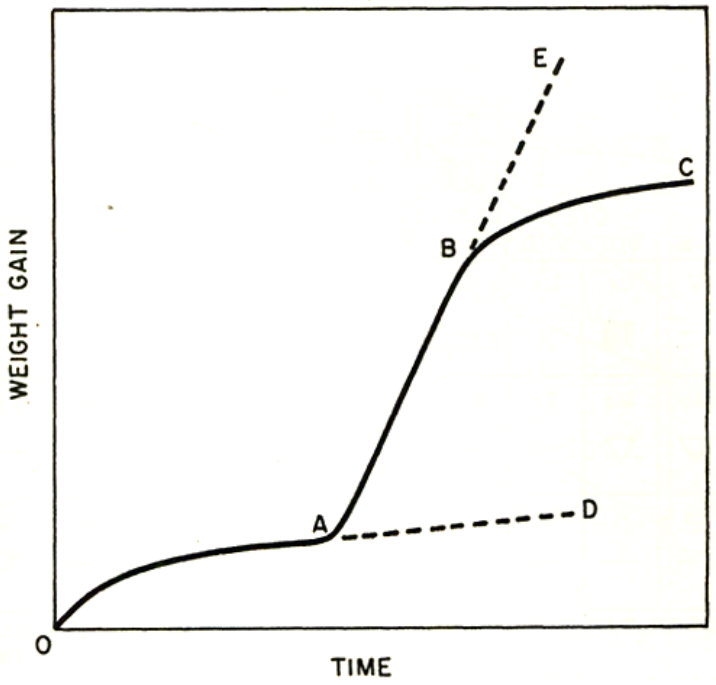

Figure 2.5. A graph showing typical stainless steel oxidation kinetics [9].

2.2.5. Oxidation of Alloys

All of the principles that have been described previously have been for simple oxidation of pure metals but this theory can also be applied to alloys. However, the oxidation of alloys can be a lot more complex due to the metals in the alloy having differing affinities to oxygen because of the different free energies of formation of the oxides. The different metals will also have varying diffusivities in the alloy and their ions will have different mobilities in the oxide phases [31]. This makes the prediction of oxidation behaviour much more difficult for alloys.

To have effective oxidation resistance the alloy needs to form a continuous scale via external oxidation. Ineffective protection can occur by precipitates forming inside the alloy during oxidation, this is called internal oxidation [32]. To achieve effective oxidation resistance, alloys aim to form compact scales with small rates of diffusion of the reactant ions [30].

The oxidation of alloys generally produces more than one oxide. Selective oxidation occurs where the least noble alloying element in the alloy is oxidised first to form the outer protective layer [30]. The alloying elements have oxides which demonstrate large differences in stability; however, the temperature, partial pressure of the oxygen and concentration of the active alloying element also affect selective oxidation [30]. Selective oxidation has lead to alloys being designed to have certain alloying additions in them to increase their oxidation resistance in high temperature applications. However, adding elements that help form protective oxide scales tends to have a negative effect on other alloy properties such as mechanical properties, and so these element additions need to be as low as viably possible [31]. Chromium, aluminium and silicon are the three main elements that when added constantly form protective scales. Their oxides have the lowest diffusion rates making them the optimum protective oxides [31]. For most industrial high temperature alloys, the base metal consists of iron, nickel or cobalt which all form moderately stable oxides, and additional alloying elements such as chromium, aluminium and silicon which form highly stable oxides [31]. Silicon additions have been found to reduce the weldability and toughness of steels and nickel based alloys, and so its concentration has to be limited to reduced levels where the formation of silica alone cannot be attained [18].

Iron-chromium alloys are a very common commercial alloy for high temperature applications. When there are small concentrations of chromium in the alloy both iron and chromium rich oxides form on the surface. The chromium solubility in the FeO phase is limited and so only some chromium will enter this phase [31]. If the chromium content is increased in the alloy the Fe^{2+} ions are blocked by the $FeCr_2O_4$ islands so the FeO layer gets thinner compared to the Fe_3O_4 layer. At a low concentration of chromium the reaction rate is still quite low [31]. If the chromium content is further increased then the parabolic rate constant is lowered due to a mixed spinel of $Fe(Fe,Cr)_2O_4$ forming. Iron ions appear to be more mobile than chromium ions in this oxide because at longer durations pure iron oxides are formed on the outer surfaces of the scale [31]. When the chromium content increases to a critical concentration the scale formed initially is Cr_2O_3 which reduces the parabolic constant further. This protective scale can only be formed at chromium concentrations which surpass this point. This is taken into consideration when designing heat resistant alloys such as stainless steels [31].

When designing the alloy and its composition for oxidation resistance the Ellingham diagram can be very helpful as it displays and compares the stability of the possible oxides forming under stated conditions. This helps show which elements in the alloy will oxidise preferentially over the others and which will oxidise next when the initial element becomes depleted. The Ellingham diagram shown in Figure 2.6 has different lines for different oxidation reactions. The lines represent the standard free energy of oxidation of pure metals versus time [32]. The lower the line on the diagram, the more stable the oxide formed is and the lower its dissociation partial pressure [31]. Chromium, silicon and aluminium are all low down in the diagram, below the iron oxides, and they are all capable of forming stable protective oxides when present in the right concentrations in the alloys.

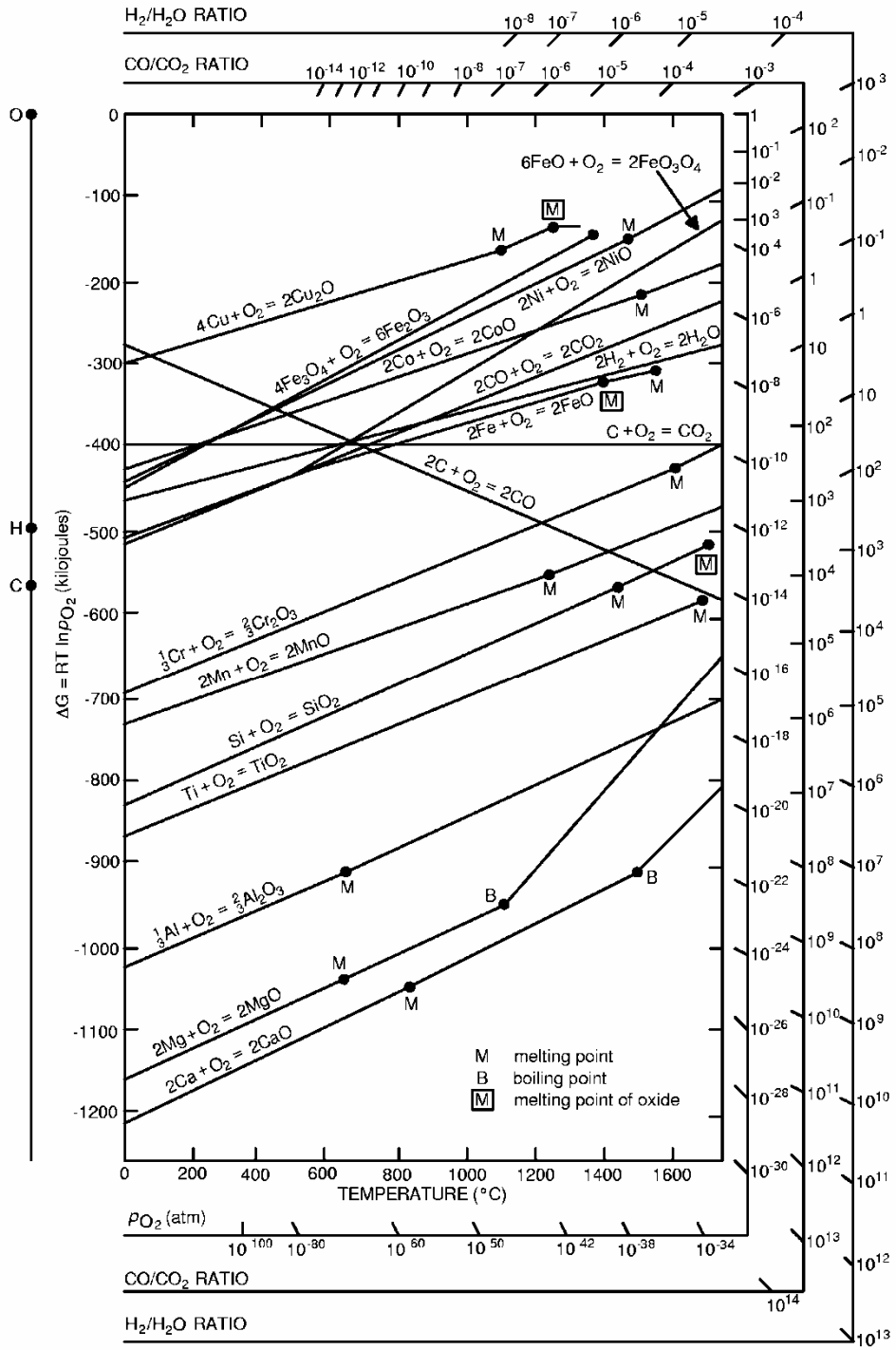

Figure 2.6. An Ellingham diagram displaying common oxides [33].

2.2.6. Alloy Depletion

As the oxidation reaction occurs at high temperature the oxide formation needs to be provided with a supply of the active elements from the substrate. If the active element is not in the adjacent area to the oxide then this will become the rate determining factor. The active element is consumed in the substrate during the reaction via diffusion towards the oxide. The region of substrate beneath the oxide layer then becomes depleted of this active element. Further depletion could lead to the protective oxide being unable to be maintained due to concentration of the active element becoming too low. This can lead to breakaway oxidation [34, 35].

The chromium depletion zone can have a positive effect on spallation resistance as this de-alloying can change the microstructure and therefore mechanical properties. If the depleted zone is weaker than the substrate then creep will occur here and reduce stresses built up from thermal cycling and thermal expansion coefficient mismatches. These relaxed stresses help prevent spallation [34].

2.2.7. Scale Spallation

The scales formed from the oxidation reaction usually experience mechanical stress which is what causes fracture, microcracking, scale delamination and spallation. When the stress in the scale increases to the limit accommodated by elastic strain, it will deform or fracture [18]. The spallation of the scale removes its protective function allowing direct access of the environment to the metal beneath and leads to a rapid increase in oxidation [36, 37]. Therefore it is desirable to design and use alloys that form oxides which do not fracture and spall [18]. Repeated spallation in alloys with a low chromium concentration can lead to alloy depletion where the protective chromia oxide will no longer form [19]. The stresses in the oxide are influenced by the stresses changing in both the metal and the oxide. These stresses can grow during oxidation itself, called growth stresses[1] where the specific volume of the oxide is

[1] Growth stresses can be caused when the volume changes caused by oxidation can be inhibited by the shape of the alloy or structure, which can cause the oxide to incur strain or start to deform. This is due to the fact that the specific volume of the oxide is usually not the same as the volume of the metal being consumed in the reaction

usually not the same as the volume of the metal being consumed in the reaction, which can also be influenced by specimen geometry; see Figure 2.7 [18, 31, 38]. Concurrent radial stresses also grow in the oxide as seen in Figure 2.7. Compositional changes due to depleted elements as discussed in the alloy depletion section can also cause growth stresses in the scale but also relieve stress by creep. Generally any deformation to the substrate material will be transferred to the adherent oxide [18].

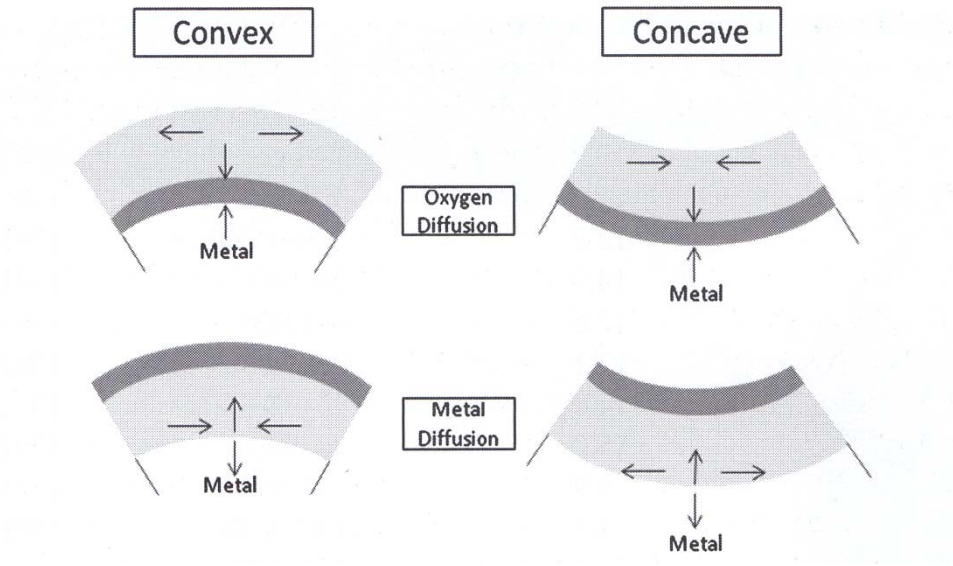

Figure 2.7. The effects of specimen geometry on scale growth stresses with the dark grey shading signifying newly grown oxide [18].

[31]. The specimen geometry is highly influential on growth stresses as additional stresses can occur during oxidation of curved metal surfaces such as tubing. The type of stresses that arise will depend on the type of curvature and the mechanism of scale growth [31]. There are four different scenarios shown in Figure 2.7 that could occur when the common condition where the volume of oxide/volume of metal > 1 exists: convex surfaces experiencing anionic oxidation, convex surfaces experiencing cationic oxidation, concave surfaces experiencing anionic oxidation and concave surfaces experiencing cationic oxidation [31, 38]. For the convex surface experiencing oxygen diffusion (anionic), the metal-oxide interface recedes and the oxide is compressed tangentially into the smaller volume where the metal was previously [18].

The second type of stresses that arise in the oxide layer are thermal stresses caused by differential thermal expansion or contraction in the oxide and the substrate during temperature change [31]. The extent of thermally induced stresses is dependent on the size of the temperature change and the difference in thermal expansion coefficients of the oxide and the substrate. These usually put the scale formed under compressive stress on cooling causing fracture and spallation [18]. Thus, cyclic exposure tends to be harsher than isothermal exposures [19, 31]. The following equation [39] expresses the magnitude of these thermal stresses when the alloy cools from temperature T_1 to temperature T_2;

$$\sigma = \frac{E_c (T_1 - T_2)(\delta_m - \delta_c)}{1 + 2\left[\frac{E_c}{E_m}\right]\left[\frac{y_c}{y_m}\right]} \qquad \text{(Eq. 2.6)}$$

where E = elastic modulus, δ = thermal expansion coefficient, y = thickness, and c, m = subscripts referring to oxide and metal respectively.

If $\delta m > \delta c$ then the stresses are compressive and quickly induced leading to scale failure [19].

The component or specimen responds to these stresses by either the oxide cracking or spalling from the substrate exposing fresh metal to the oxidising gas, or by plastic deformation of the substrate or the oxide [31]. Oxide cracking occurs when it is under tension, but most oxides are under compression due to the growth and thermal stresses being compressive. Spallation due to compressive stresses can occur by either buckling or wedging shown in Figure 2.8 [40]. This will depend on factors such as scale thickness, defect size in the oxide and the fracture toughness of the scale or scale/metal interface [41]. Wedge cracking occurs when the scale is less resistant to rupture than the substrate-scale interface. Compressive shear cracks form in the scale first then decohesion at the interface occurs [40]. Buckling occurs when decohesion occurs first at the interface without through thickness cracking of the scale. The compressive stresses causes the scale to buckle during cooling until finally tensile cracks propagate at the points of greatest curvature in the scale to relax the stress and strain [40].

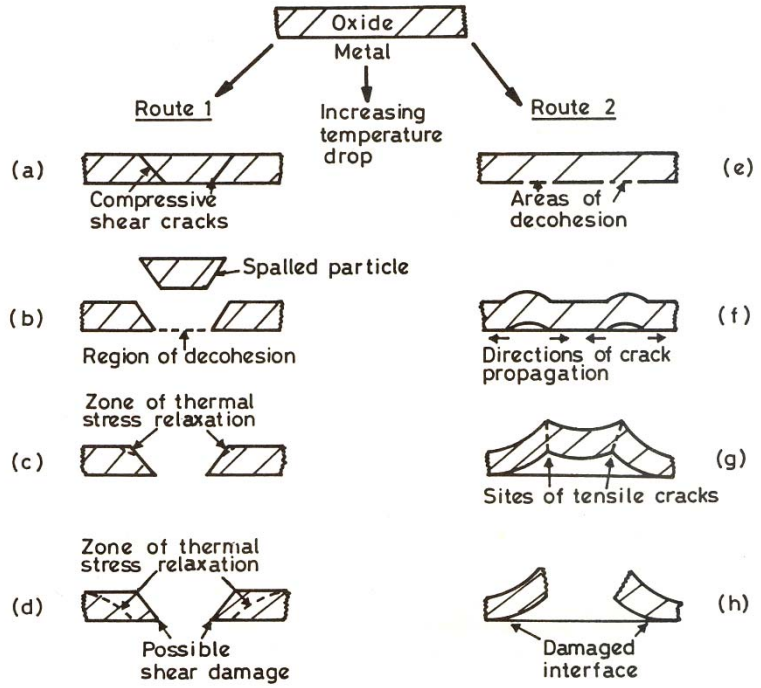

Figure 2.8. Schematic representation of oxide under compression fracturing via wedging (Route 1) and buckling (Route 2) [19].

2.3. Oxidation in Water Vapour and Steam

For a detailed description of the oxidation of steels in water vapour and steam, and the associated mechanisms, see Appendix 1.

3. Experimental Procedure

3.1. Materials

The materials studied in this project were a selection of four steels ranging from materials that are currently in use in plant (i.e., martensitic steels), and the proposed new materials which are the '18/8' austenitic (300 series) stainless steels with higher chromium content. In addition, a variant on the super 304H was also tested; these specimens had a shot peened inner bore. All of the steels were received in tube form as they would go into the RWE Npower plant. These steels designations and composition in weight percentage are shown in the Table 3.1.

Table 3.1. Steel Composition in wt% (white) and at% (grey).

	C	Si	Mn	P	S	Ni	Cr	Mo	W	Cu	V	Nb	Al	B	N
T91	0.11	0.31	0.46	0.015	0.0038	0.09	9.46	0.88	-	-	0.2	-	-	-	-
	0.51	0.55	0.46	0.03	0.0065	0.08	9.98	0.51	-	-	0.22	-	-	-	-
T92	0.098	0.29	0.42	0.007	0.0013	0.13	9.5	0.36	1.74	-	0.19	0.062	0.009	0.002	0.0462
	0.46	0.55	0.43	0.01	0.0022	0.12	10.06	0.21	0.53	-	0.21	0.04	0.02	0.01	0.18
Super 304H	0.1	0.2	0.8	-	-	9	18	-	-	3	-	0.4	-	-	0.1
	0.46	0.39	0.84	-	-	8.29	19.35	-	-	2.60	-	0.24	-	-	0.39
347H FG	0.08	0.75	2	0.04	0.03	11	18	-	-	-	-	0.82	-	-	-
	0.36	1.64	2.18	0.07	0.05	10.38	19.13	-	-	-	-	0.48	-	-	-

All steel tubes were supplied in the as-received condition, i.e. as they go into plant, except for the T91 which was a post-service sample that had been exposed to steam at temperatures of 580^{o}C ±20^{o}C for a duration of approximately 79000 hours. This tube was studied solely for morphological comparison. The T91 and T92 tubes are both martensitic and are currently used in plant. The super 304H and 347H FG are both austenitic stainless steels and are being proposed for future plant use at higher steam parameters. It should be noted that the chromium concentration of these austenitic stainless steels are similar. The dimensions of the tubes received from RWE Npower are shown in Table 3.2.

Table 3.2. Tube dimensions.

Steel	Outside Diameter / mm	Wall Thickness / mm
Super 304H shot peened	41.3	6.5
Super 304H	42.4	5.6
347H FG	38.1	4.5
T92	51.5	8.0
T91 post service	53.0	8.9

The tubes were sectioned into rings approximately 25mm in length. These were further sectioned into six radial sections producing specimens, as shown in Figure 3.1, for examination and oxidation testing. Cut edges were removed/smoothed using 1200 grit SiC paper with a water lubricant. One specimen from each batch was examined in the as-received condition.

3.2. Isothermal Air Oxidation Tests

The inner surfaces of all the specimens were tested in their as-received condition except T92. The T92 specimens were found to retain some residual oxide on the inner surface in the as-received condition. To assess its affect, half of this surface was abraded with a series of silicon carbide papers; 240, 400, 800 and finishing with 1200 grit paper. The other half of the inner surface was left in the as-received condition with the original oxide layer as shown in Figure 3.1. Each sample was weighed using a highly sensitive electronic scale, accurate to ±0.000005g. The dimensions of each sample were measured and recorded using a digital micrometer so that the surface area of each specimen could be calculated. Finally, each sample was cleaned just prior entering the furnace in an ultrasonic bath with acetone.

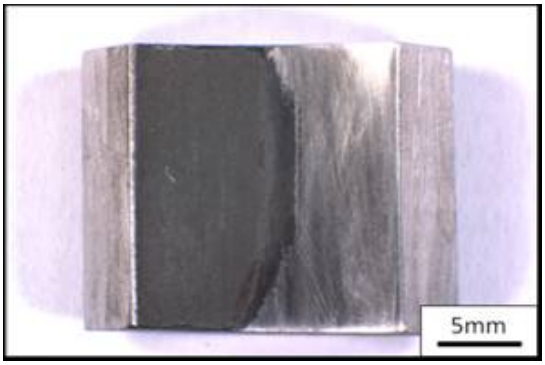

Figure 3.1. T92 sample with half the inner surface abraded to 1200 grit (right side) as it would go into the furnace.

The samples were tested in batches of four, one from each tube, with their inner surfaces facing uppermost. The furnaces used were Elite Thermal Systems Ltd tube furnaces (Figure 3.2) which were calibrated using and an external calibrated thermocouple and voltmeter. In each case the size of the heat zone was confirmed by taking calibrated temperature readings along the furnace tube. The furnace was set to the required temperature before inserting the samples. The tests were conducted at 600^{o}C, 650^{o}C and 700^{o}C in laboratory air for 100h, 250h, 500h and 1000h. On completion the specimens were removed and left to cool in laboratory air. Once cooled, the samples were re-weighed and the mass change per unit surface area was calculated without including the spalled oxide mass.

Figure 3.2. Photograph of the tube furnaces used for isothermal oxidation testing.

Samples were visually inspected for signs of gross spallation. Images were taken with an Axiovision Macroscope of the inside surface of each sample to record the oxide surface appearance. The inner surface of each tube, in the as-received condition, was also examined using Scanning Electron Microscopy.

3.3. Sample Preparation and Cross Sectional Metallography

The samples were prepared for cross-sectional analysis using standard techniques. To prevent damage to the oxide scale the oxidised samples were vacuum impregnated with a low viscosity Epofix resin. Once the resin had cured the sample was transversely sectioned at the mid length using a silicon carbide cutting disc and an especially slow feed rate of 0.015mm/s to prevent damage to the oxide scale. The sectioned sample was then mounted in a Tri Hard resin to aid the polishing process. The samples were manually ground under tap water using successive silicon carbide paper of 120, 240, 400, 800 and then 1200 grit. All samples were cleaned between stages with tap water and degreaser, with a further clean in ethanol and fan dried before the polishing stage. The samples were manually polished to 6μm using a Mol cloth and 6μm diamond suspension, followed by polishing using a Nap cloth and 1μm diamond suspension. The final polish was performed on an automatic Syton Polisher using OP-S colloidal silica suspension which provides a 0.04μm finish. The same cleaning process was also used between all of the polishing stages.

To observe the different grain structures of the steels, selected samples were etched and examined using optical microscopy. The martensitic steel (T92) was etched by swabbing the sample in Viella's solution for 5 seconds. The austenitic steels were etched electrolytically in 10% oxalic acid for 30 seconds each. Digital optical microscopy of up to 100x magnification was used to observe and record the microstructure of each steel.

For examination using Scanning Electron Microscopy (SEM) and Energy Dispersive Spectroscopy (EDS) the samples were sputtered with gold to produce an electrically conductive layer, and subsequently painted with silver to increase the conductivity further and reduce charge build up in the scanning electron microscope (SEM).

The Jeol 6060 tungsten filament and Philips XL 30 LaB_6 SEM were used to take micrographs of inner surface region of each sample at different magnifications along the whole oxide to get representative images. All SEM work was performed using a 20 keV accelerating voltage throughout. Back scattered electron images were preferred over secondary electron images as the oxide was more visible and composition changes could be observed.

3.4. Oxide Thickness Measurements

For each image a scale calibration was made, and ten equidistant oxide thickness measurements were made using ImageJ software (Figure 3.3). The specimen surfaces were rarely flat and so measurements were made perpendicular to the substrate surface, i.e. the growing direction. This produced 60 oxide thickness measurements for each sample so that the mean and standard deviation could be gained for a thorough assessment of thermally grown oxide (TGO) thickness.

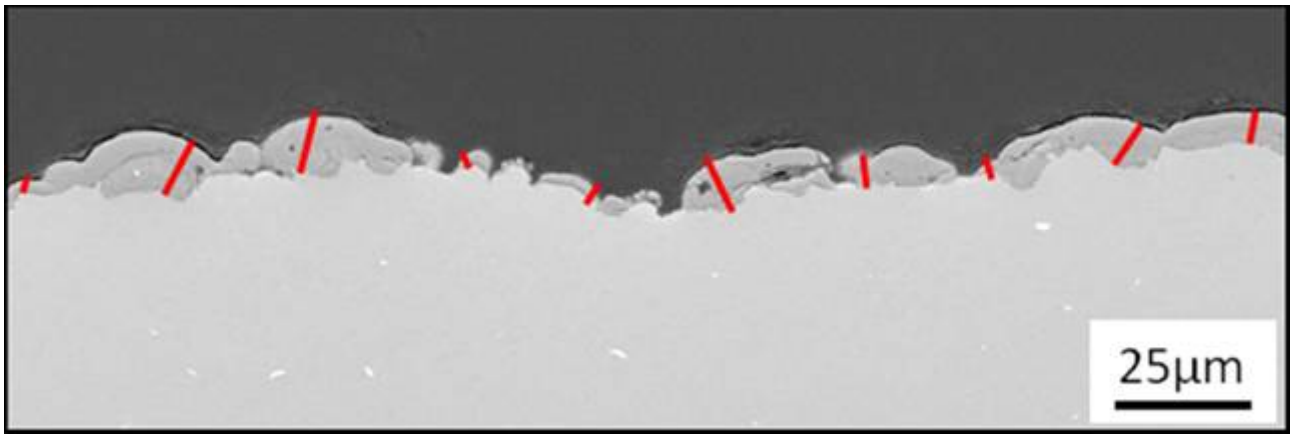

Figure 3.3. A SEM image showing an example of where the oxide thickness measurements would be made using ImageJ, depicted by the red pointers.

3.5. Energy Dispersive X-Ray (EDX) Chemical Analysis

Chemical analysis of the sample cross section was performed using Oxford Instruments energy dispersive X-ray spectroscopy (EDX) with the INCA software. Several point scans were made along the oxide layer/layers and averages calculated to help identify the different

oxide layers forming. Line scan analysis was also performed to gain compositional information through the depth profile of the oxide formed. Six line scans were completed on each sample, with one scan covering the adjacent substrate region also. The line scans were made perpendicular to the alloy surface, starting in the base alloy then going through the oxide and finishing in the resin. Each line scan was run for 20 minutes.

4. Results

4.1. Materials Characterisation

4.1.1. Composition

Table 4.1 shows the quantitative EDX results for the four alloys examined in this research programme. Also included is the composition of the super 304H samples which had a shot peened inner bore, demonstrating that the two alloy samples were of the same nominal composition. There is a significant difference in the Cr content when comparing the two steel types, i.e. the martensitic steels (T91 and T92) with the austenitic steels (super 304H and 347H FG). Some minor compositional differences can be seen between the martensitic steels and similarly for the austenitic steels. The main difference between the super 304H and the 347H FG is the copper content, added for creep strength, and niobium content, which is added to 347H FG for creep strength as well. The niobium in the super 304H is used for solid solution strengthening.

Table 4.1. The compositions of alloys tested in wt-%, determined by EDX.

Alloy (wt-%)	Si	V	Cr	Mn	Fe	Ni	Nb	Mo	W	Cu
T91 post service	0.3	0.3	9.3	0.4	89.6	0.1	-	-	-	-
T92	0.1	0.3	9.3	0.7	86.8	0.3	-	0.5	2.0	-
Super 304H	0.2	-	19.0	1.0	68.1	8.6	0.5	-	-	2.6
Super 304H shot peened	0.3	-	19.3	1.0	67.5	8.5	0.7	-	-	2.8
347H FG	0.5	-	19.2	1.8	66.4	10.8	1.4	-	-	-

The appearance of the inner surfaces of the tubes in the as-received condition is shown in Figure 4.1. All inner surfaces are shiny except the T92 sample which is covered by a dark oxide (Fig 4.1a.).

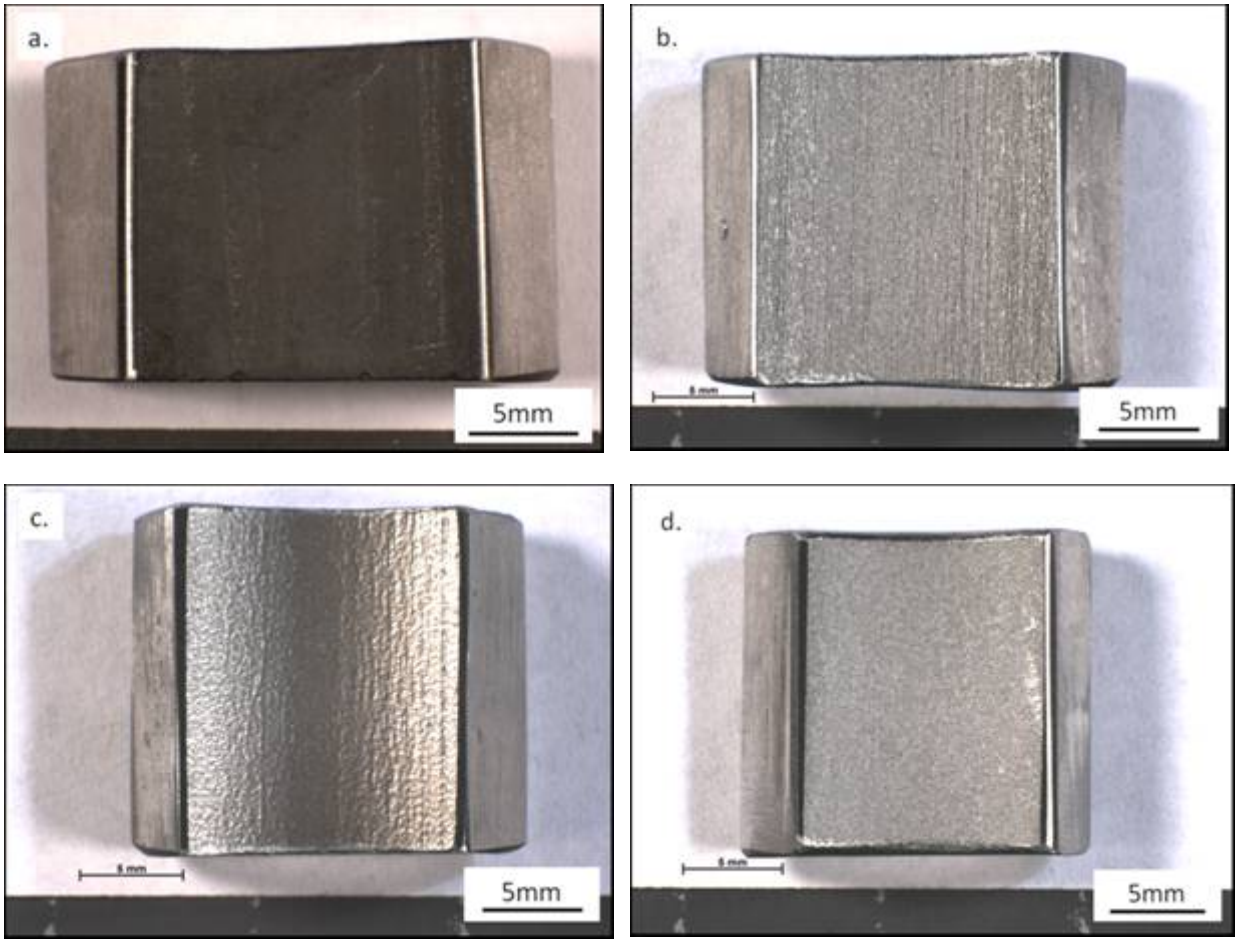

Figure 4.1. Optical macrographs of the inner surfaces of the as-received tubes, a.) T92 with pre-existing dark oxide, b.) super 304H, c.) shot peened super 304H which is shinier than the standard super 304H surface, and d.) 347H FG.

Figure 4.2 shows electron micrographs of the inner surfaces of the three austenitic stainless steel tubes. The super 304H and 347H FG have a very similar rough surface finish, the inside of the tubes are almost identical. This is likely due to a pickling process in manufacture. However, super 304H had intermittent small grooves running along the length of the tube. The difference between the super 304H and shot peened super 304H inner surfaces is very apparent, the later is much smoother without grooves and the granular roughness. The shot peened surface also has overlapping dimples as seen in Fig 4.2b.

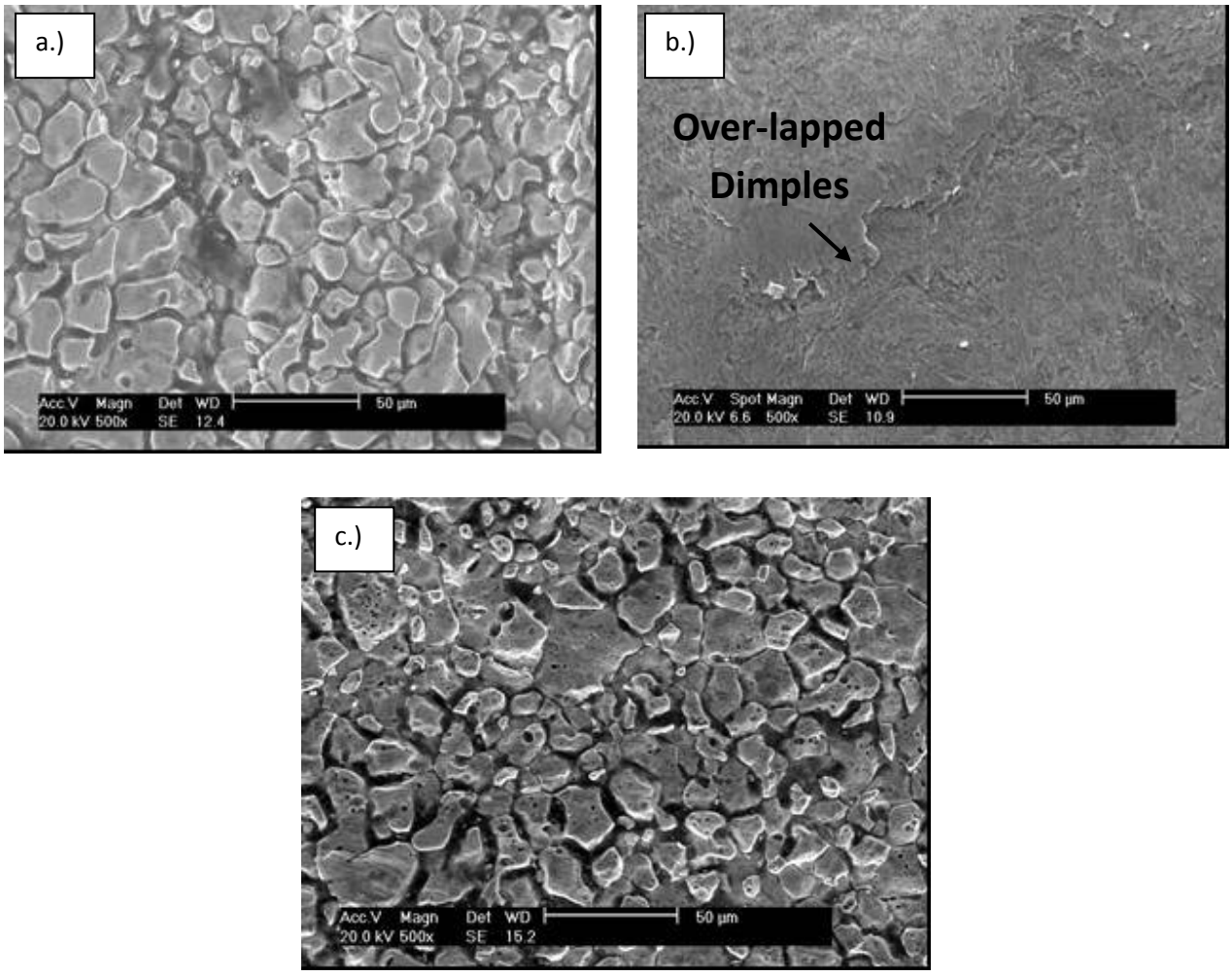

Figure 4.2. Secondary electron micrographs of the as received inner surfaces of a.) super 304H b.) shot peened super 304H and c.) 347H FG. The surfaces of the super 304H and the 347H FG look similar.

4.1.2. Grain Structure As-Received

Cross-sectional optical micrographs of the etched steels in the as-received condition are shown in Figures 4.3 to 4.6. The etch with Viella's solution clearly shows the uniform equiaxed grain structure of the T92 alloy in Figure 4.3. The surface was uneven and covered in a continuous uniform oxide.

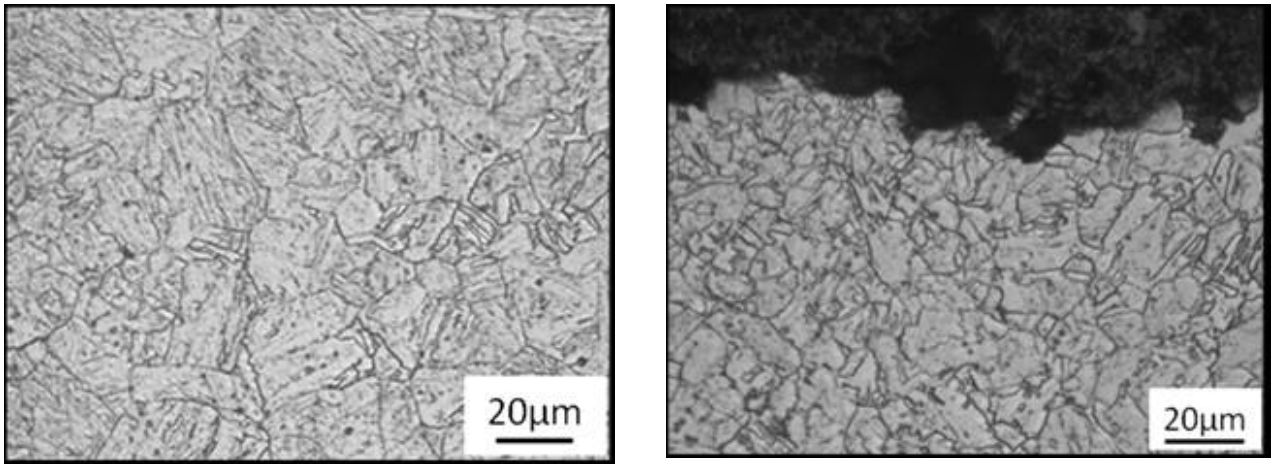

Figure 4.3. Optical micrographs of the as received T92 cross sectioned and etched in Viella's solution showing grain boundaries and the martensitic structure within.

The 347H FG was electrolytically etched in 10% oxalic acid at 5V to reveal the twinned austenitic equiaxed grain structure shown in Figure 4.4. This was uniform throughout the sample up to the sample edge, which was uneven and did not already have an as received oxide formed.

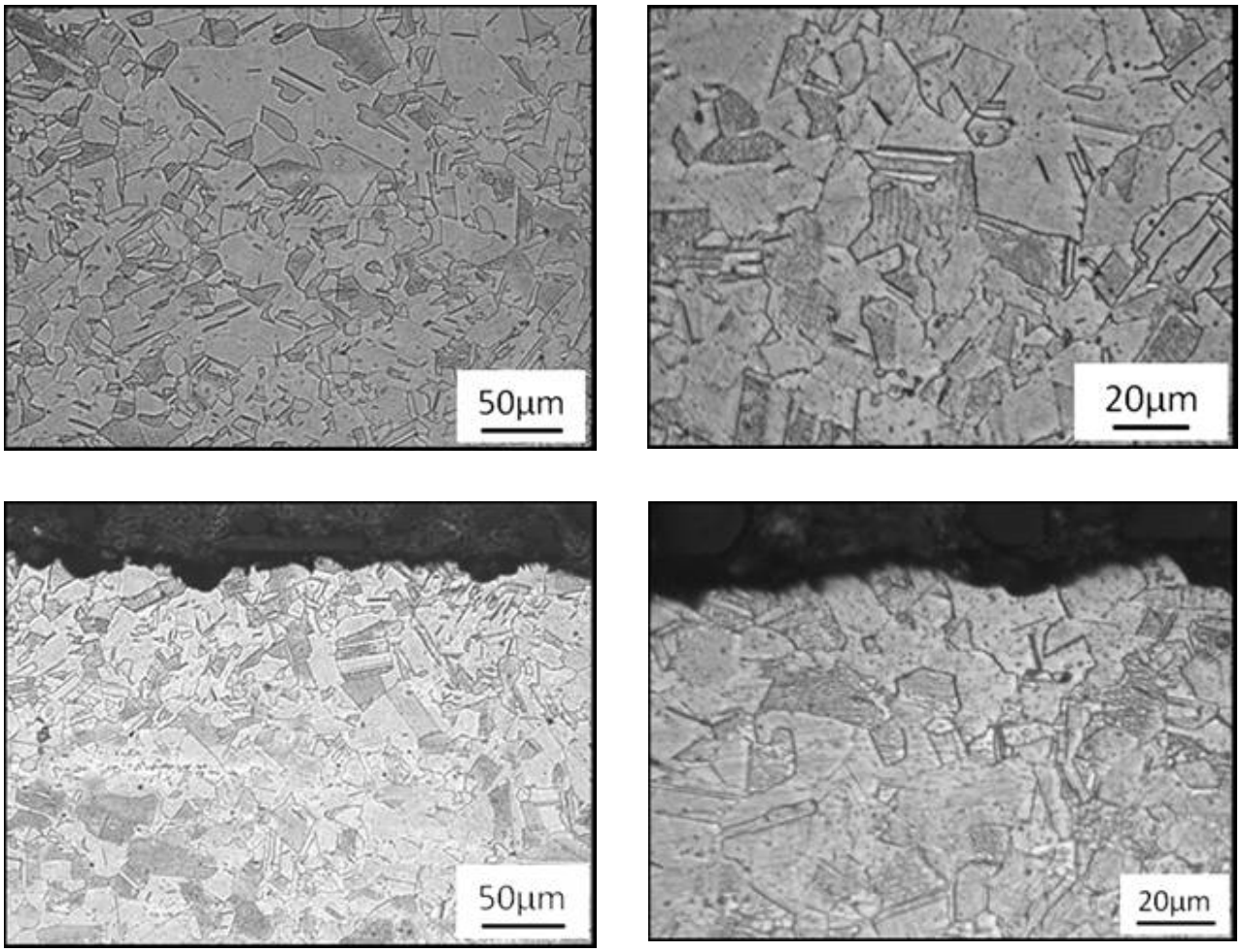

Figure 4.4. Optical micrographs of the as received 347H FG electrolytically etched in 10% oxalic at 5V acid showing austenitic grain structure and boundaries.

The super 304H was etched electrolytically to reveal the twinned austenitic equiaxed grain structure shown in Figure 4.5. The inner surface was very uneven and contained no as received oxide.

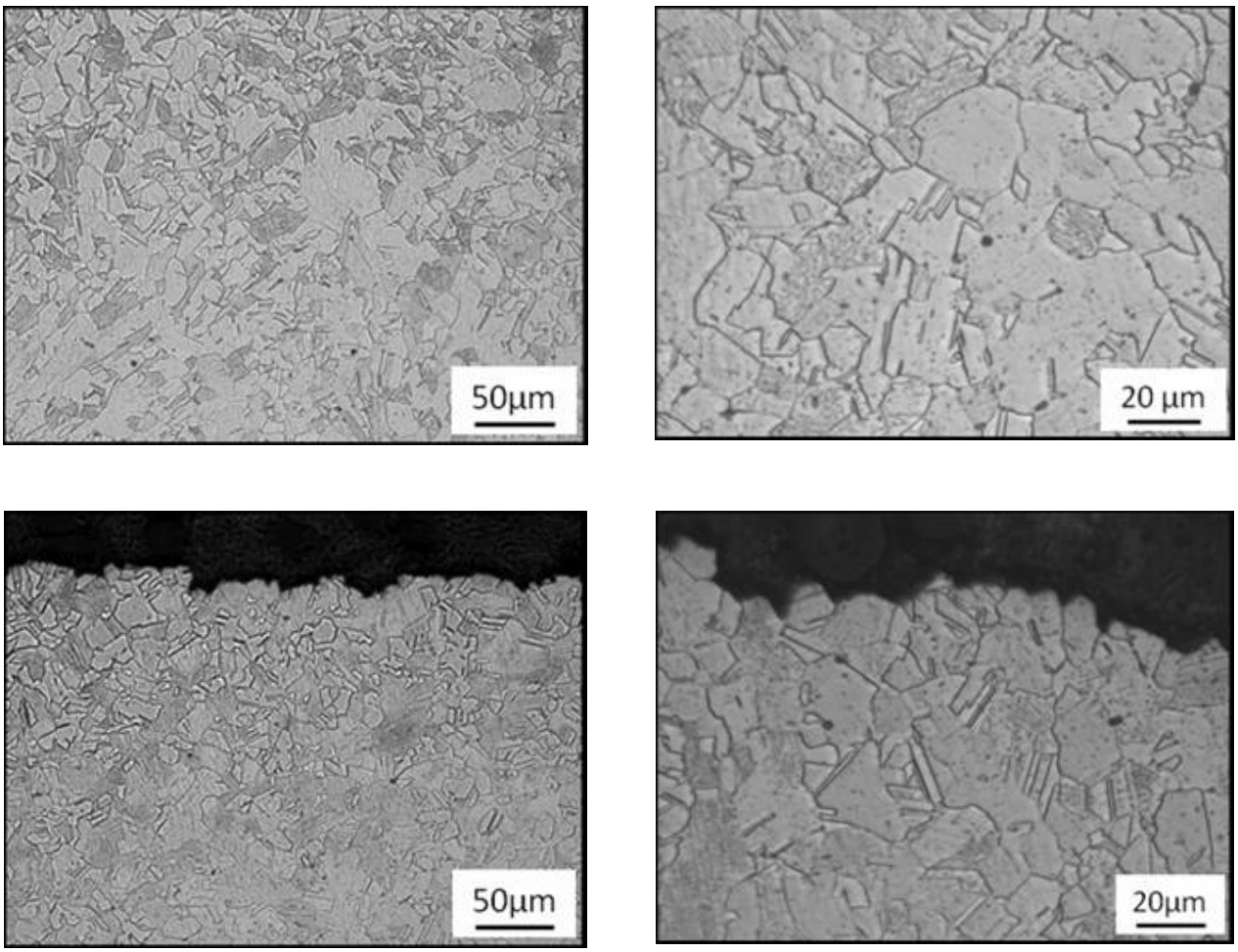

Figure 4.5. Optical micrographs of the as received super 304H electrolytically etched in 10% oxalic acid at 5V revealing austenitic grain structure.

Comparison of Figure 4.6 to Figure 4.5 shows that the effect of shot peening the super 304H penetrates to approximately 30µm, where the grain boundary density has increased. The surface is much smoother with intermittent overlapping dimples as seen on the surface images.

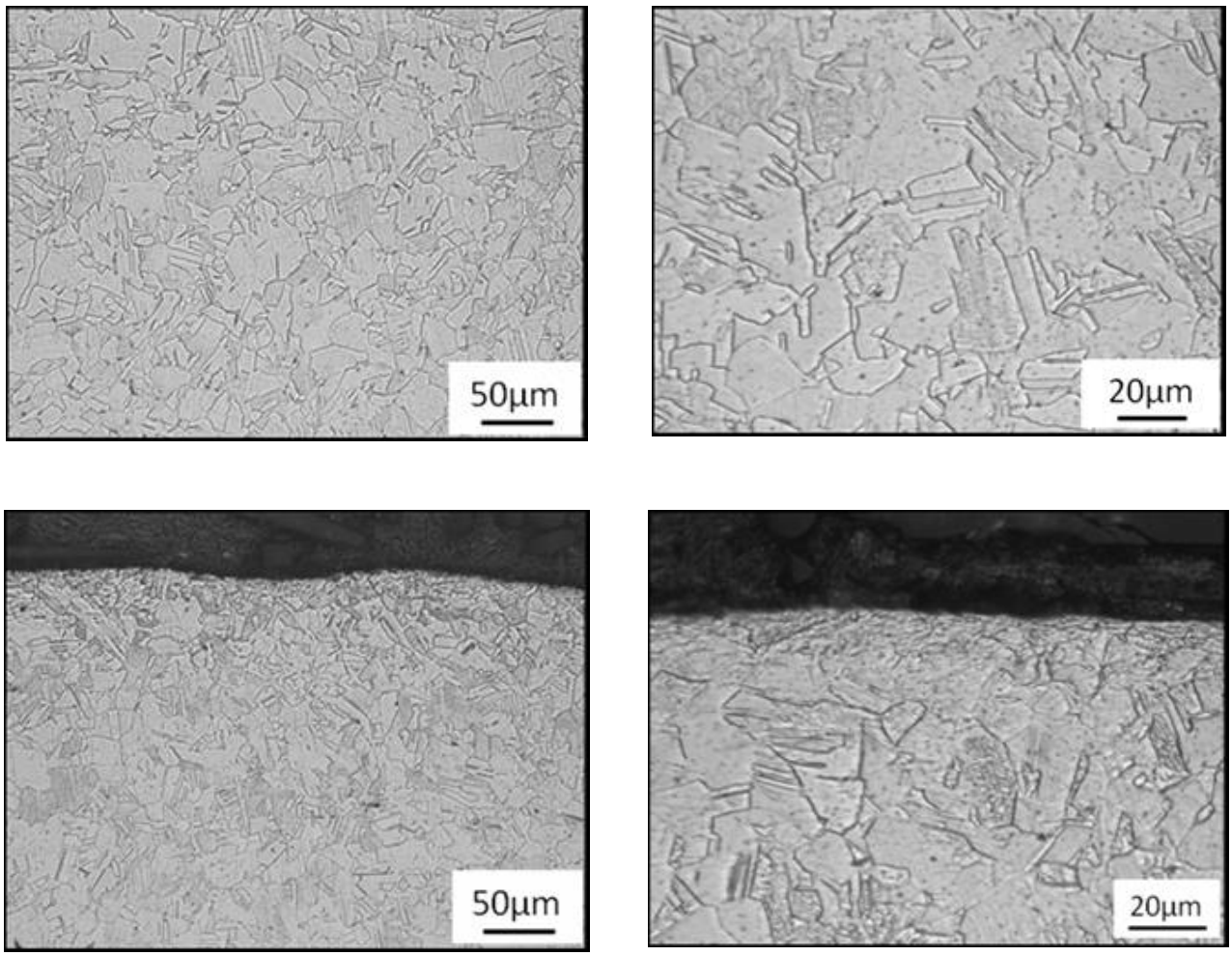

Figure 4.6. Optical micrographs of the as-received shot peened super 304H electrolytically etched in 10% oxalic acid at 5V showing the austenitic grain structure and compressed surface region.

4.2. Oxidation in Air

4.2.1. Mass Change Results

All three austenitic steels follow a similar gradual mass gain when exposed in air at 600°C, Figure 4.7. At 500 hours the mass gain appears to level out and even slightly decrease with types 304H and shot peened 304H. The shot peened super 304H consistently shows the least mass gain. At this temperature the 347H FG appears to show the greatest mass gain and worse performance (in terms of oxidation resistance) than the super 304H samples, Figure 4.8. This is not the case at 650 and 700°C where they appear to be equal. The martensitic T92 steel did not show any mass gain, Figure 4.7, and showed an increasing mass loss over time with substantial mass loss (-1.45 $mgcm^{-2}$) after 1000 hours. This significant mass loss represents large scale spallation of the non abraded side on the inner surface of the tube.

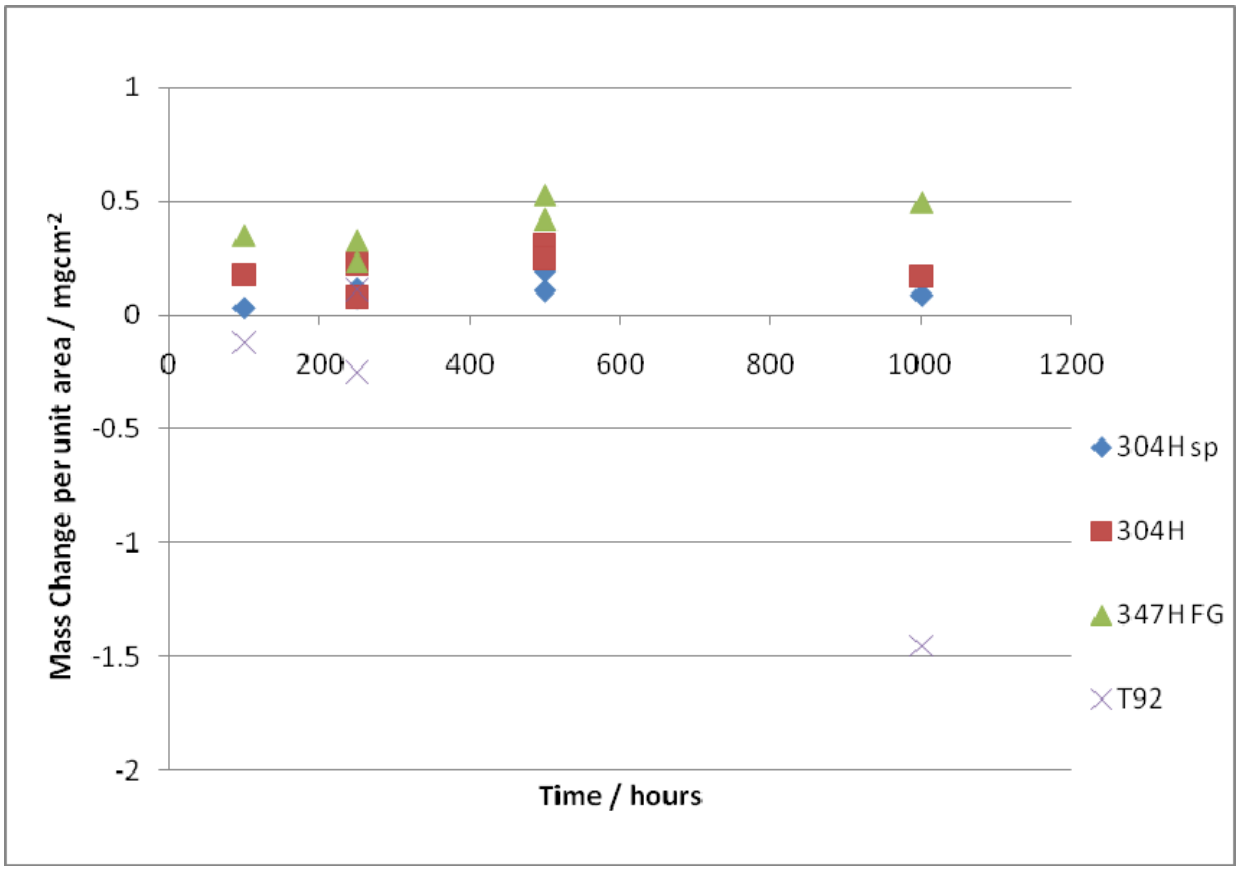

Figure 4.7. A graph showing the mass change per unit area for selected steels at varying durations at 600°C.

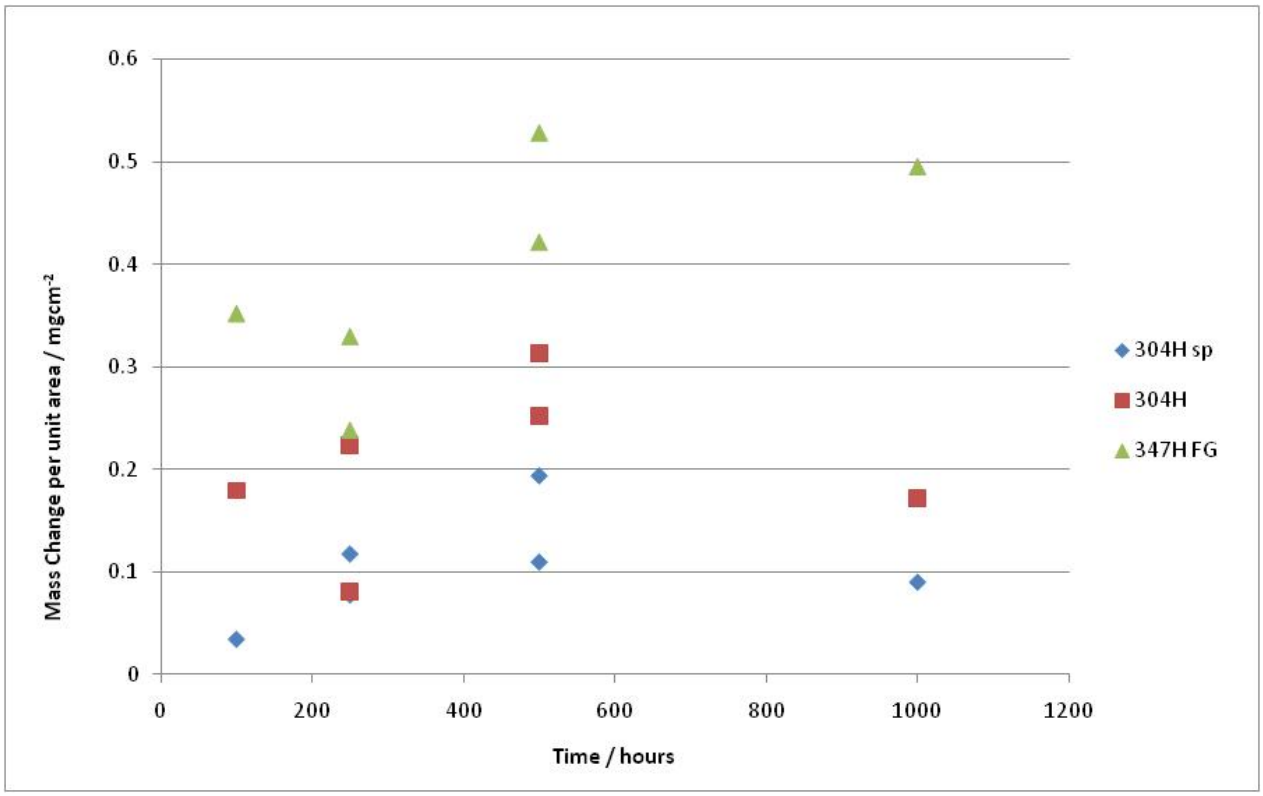

Figure 4.8. A graph showing the mass change per unit area for just the austenitic stainless steels at varying durations at 600^{o}C.

Figure 4.9 shows selected samples after 600^{o}C air exposure. The T92 sample shows widespread oxidation on both abraded and non-abraded sides, however, much of the abraded side still remained shiny. At 1000 hours T92 shows severe cracking and spallation on the non-abraded (left) side after cooling. No observable spallation was seen on the austenitic steels, just a change from shiny to a dull appearance from oxidation. However, the shot peened super 304H was the only steel to still remain shiny in appearance.

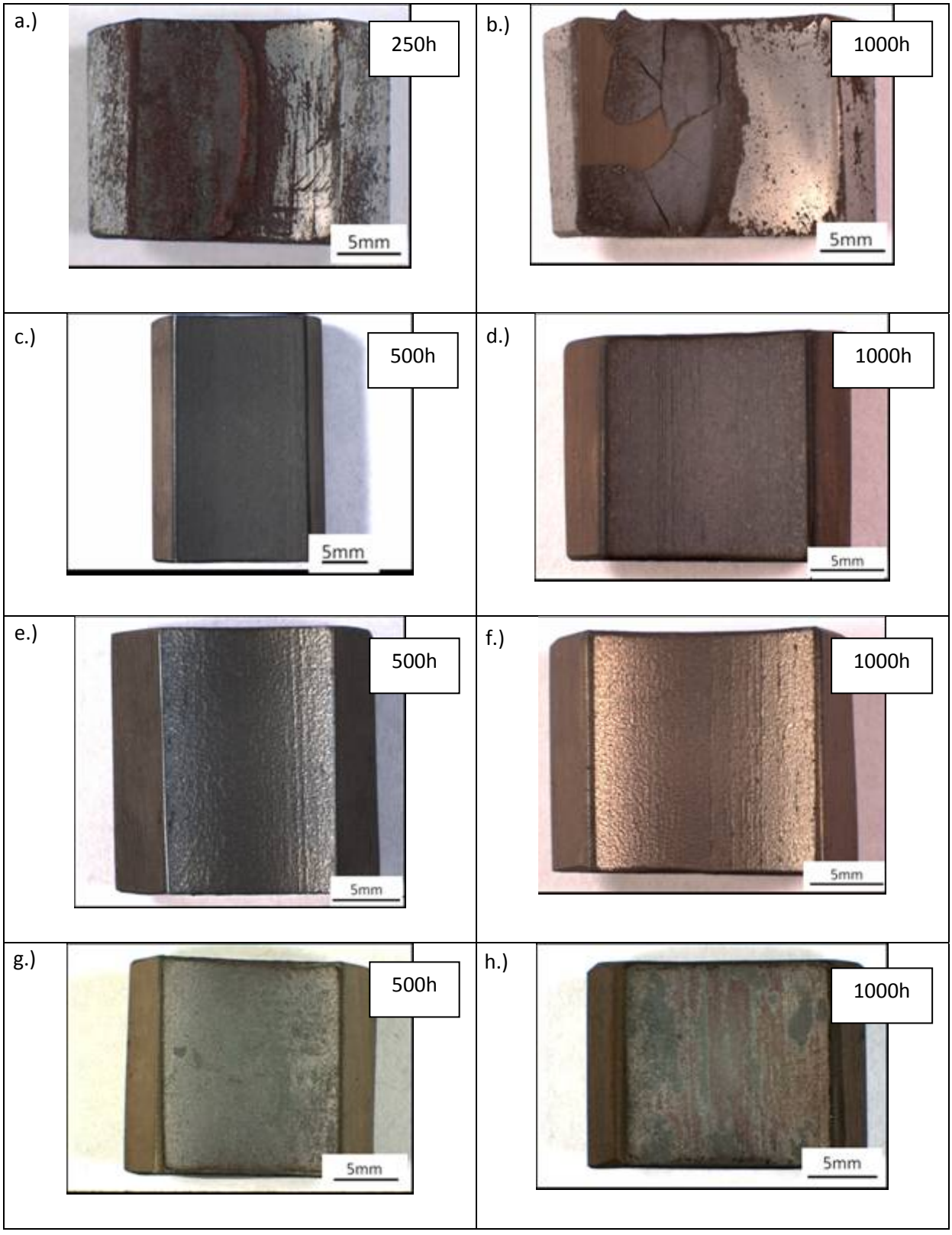

Figure 4.9. Optical macrographs showing the following sectioned samples after being exposed to 600^{o}C a.) T92, 250h, b.) T92, 1000h, c.) super 304H, 500h, d.) super 304H, 1000h, e.) super 304H shot peened, 500h, f.) super 304H shot peened, 1000h, g.) 347H FG, 500h, h.) 347H FG, 1000h.

The mass gain at 650°C for the austenitic steels shows a similar increasing trend to before, and a significant mass loss for the T92 martensitic steel, Figure 4.10. The mass gain of the austenitics again plateaus after 500 hours with the shot peened samples consistently having the smallest mass gain and the standard super 304H having the greatest, Figure 4.11.

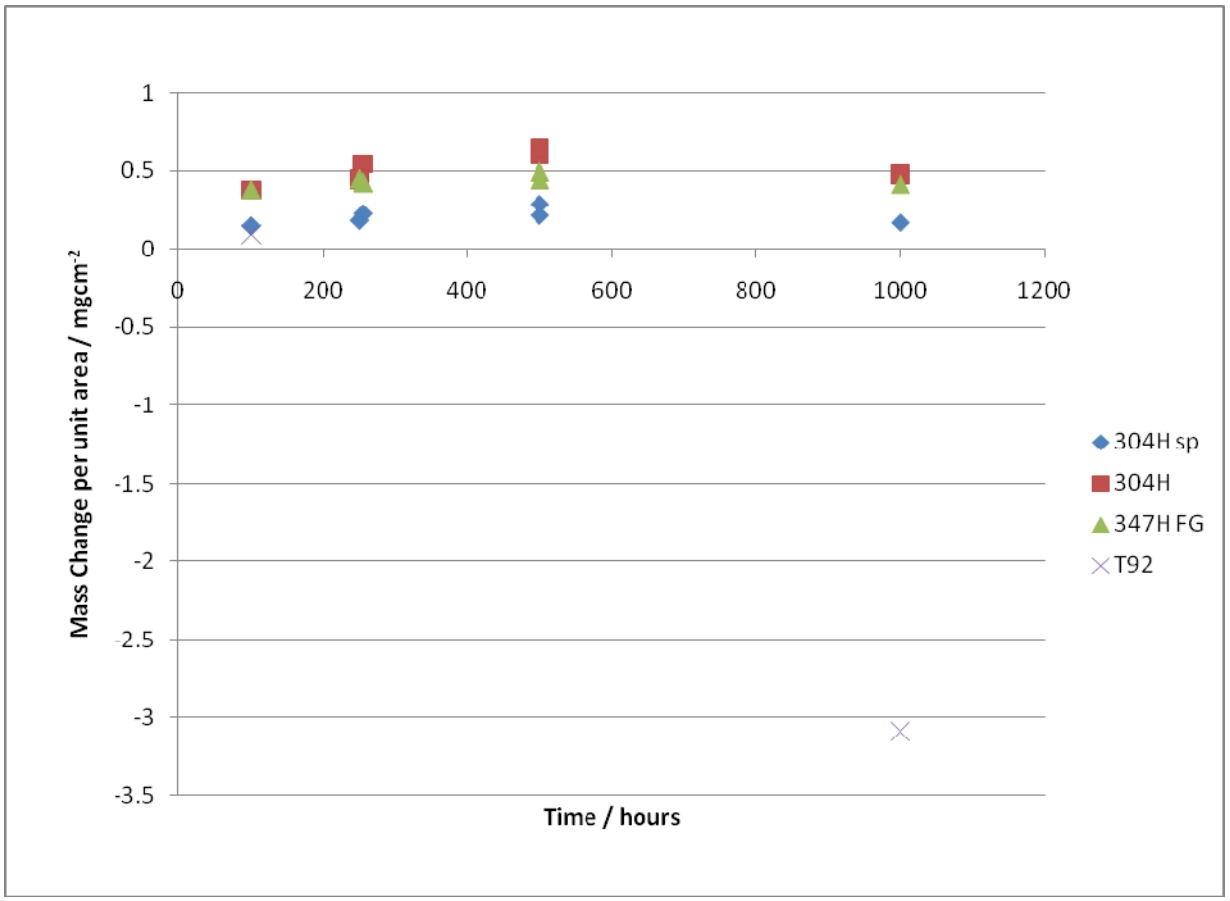

Figure 4.10. A graph showing the mass change per unit area for steels at varying durations at 650°C.

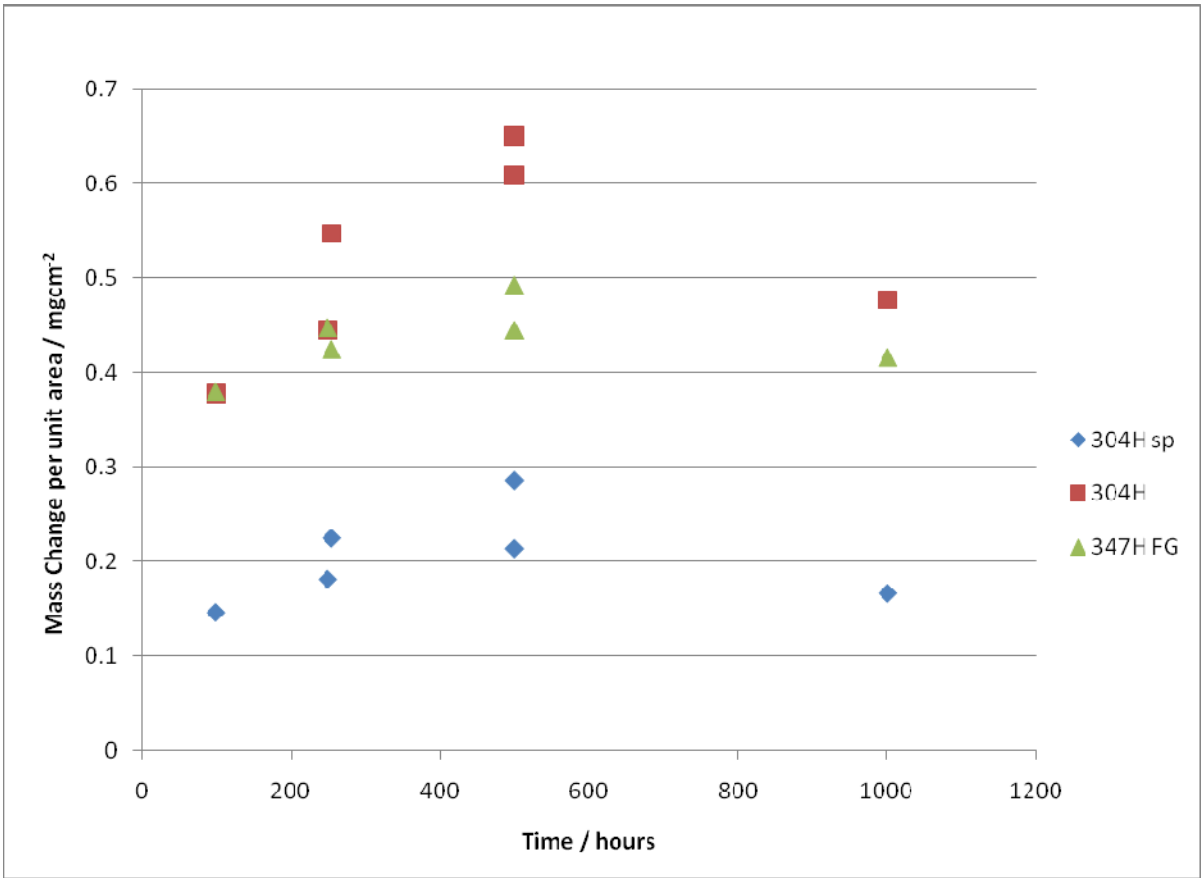

Figure 4.11. A graph showing the mass change per unit area for just the austenitic stainless steels at varying durations at 650°C.

The optical macrographs shown in Figure 4.12 illustrate the oxidised inner surfaces of the samples after exposure to 650°C. Both T92 samples show large scale cracking and spallation on the non abraded (left) side after cooling. After 1000 hours the T92 abraded side now has a dull appearance, indicating a thicker oxide growing. The austenitic steels show a dark/dull appearance due to oxide formation with no observable spallation. The 347H FG after 500 hours had a slightly uneven contrast appearance compared to the other samples.

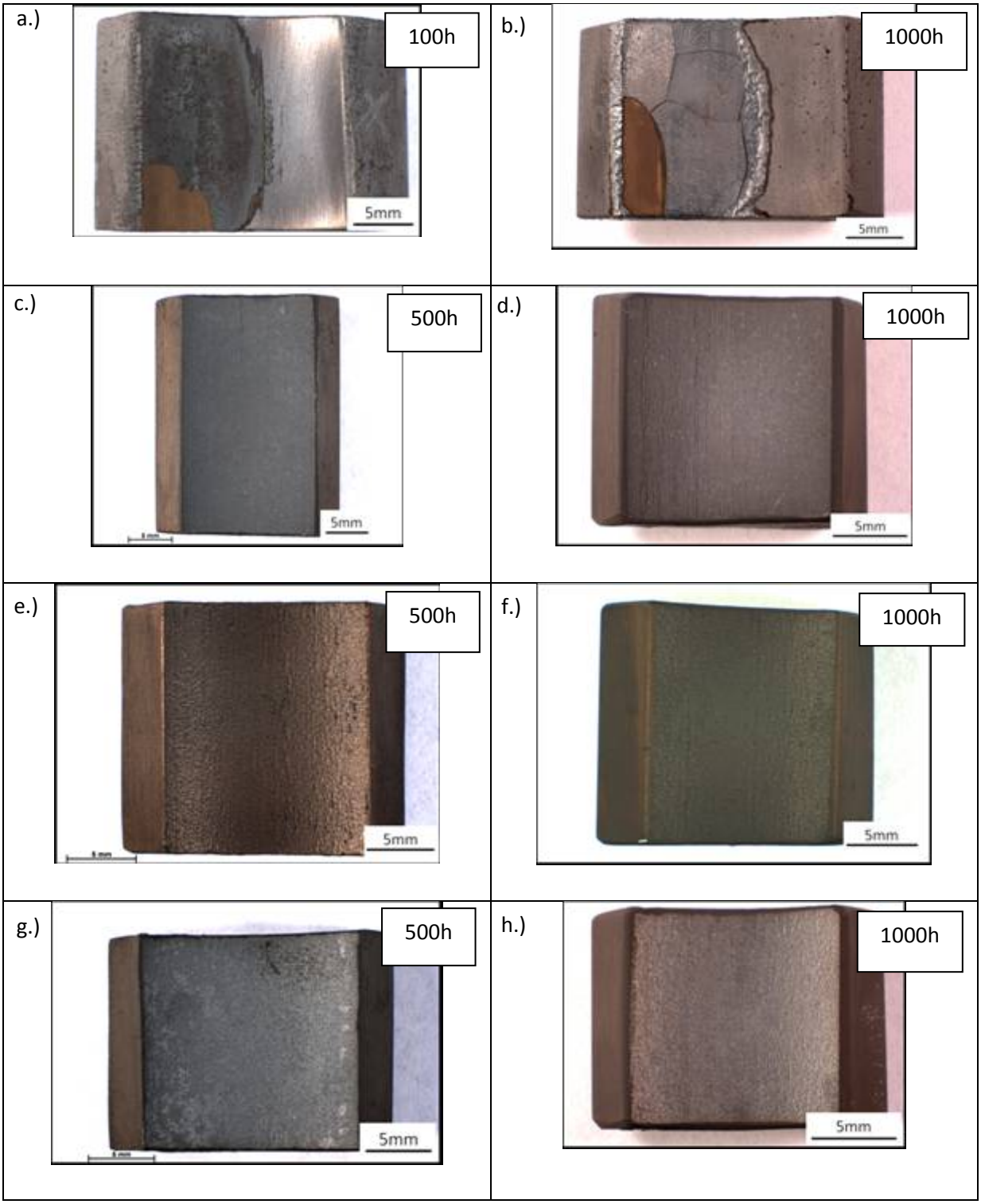

Figure 4.12. Optical macrographs showing the following sectioned samples after being exposed to 650^{o}C a.) T92, 100h, b.) T92, 1000h, c.) super 304H, 500h, d.) super 304H, 1000h, e.) super 304H shot peened, 500h, f.) super 304H shot peened, 1000h, g.) 347H FG, 500h, h.) 347H FG, 1000h.

At 700°C the mass gain of the austenitic steels was similar to before. Mass gain was the least for the shot peened super 304H, with the austenitics appearing to level off after 500 hours (Figure 4.13). However, the T92 showed a different trend in mass change to the lower temperatures. It showed a mass loss after 100 hours but after the longer durations showed a considerable mass gain much greater than that of the austenitic steels (Figure 4.14).

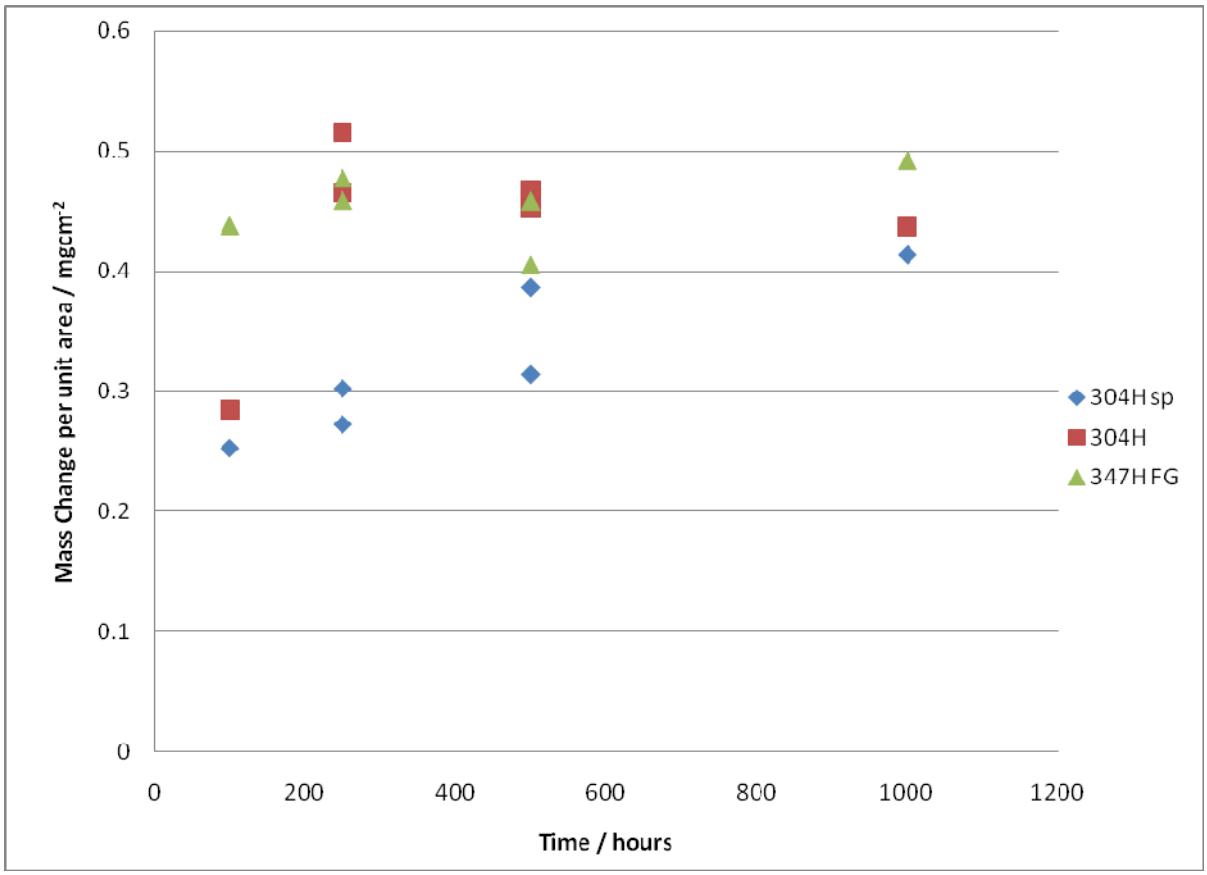

Figure 4.13. A graph showing mass change per unit area for just the austenitic stainless steels at varying durations at 700°C.

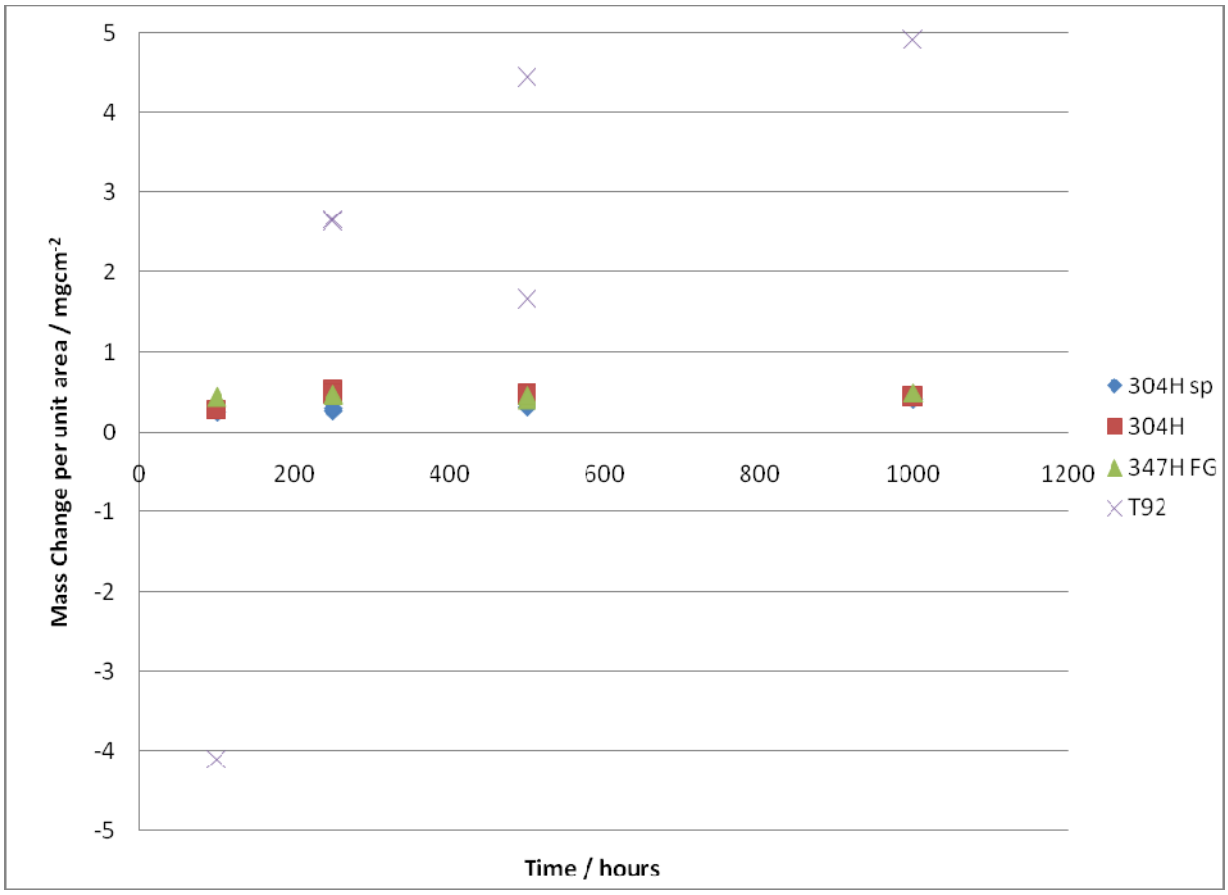

Figure 4.14. A graph showing mass change per unit area for selected steels at varying durations at 700°C.

The T92 samples after cooling from 700°C show no large scale cracking or spalling of oxide scale on either the non abraded (left) or abraded (right) side, Figure 4.15. This is consistent with the greater mass gain. However, at 700°C the abraded side is no longer shiny and was dull/dark in appearance. The oxide on the non abraded side has remained adherent to the substrate on cooling. The austenitic stainless steels all appear darker after the oxide has formed.

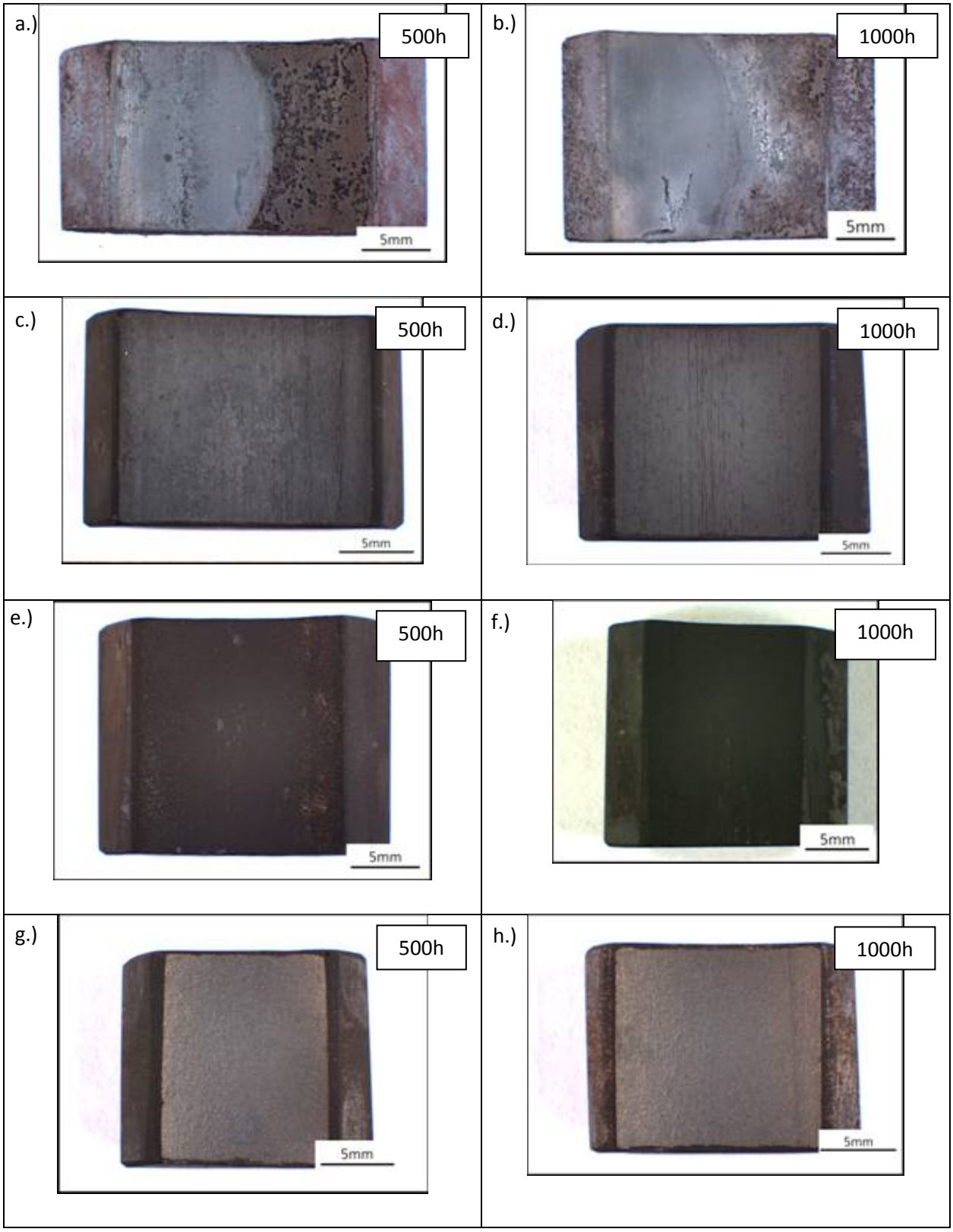

Figure 4.15. Optical macrographs showing the following sectioned samples after being exposed to 700°C a.) T92, 500h, b.) T92, 1000h, c.) super 304H, 500h, d.) super 304H, 1000h, e.) super 304H shot peened, 500h, f.) super 304H shot peened, 1000h, g.) 347H FG, 500h, h.) 347H FG, 1000h.

4.2.2. Overall Thickness Analysis

The average inner surface oxide thickness measurements were taken for each sample. The oxides forming on the samples were initially nodular and discontinuous resulting in high standard deviations for the initial duration thickness measurements (see Appendix A.2). All oxide growth was initailly fast and then slowed down after 100 hours. The oxide formed on the shot peened super 304H samples was not thick enough to be measured on many of the samples especially at lower temperatures and shorter durations. The oxide growth on the T92 samples could also not be measured due to mass spallation on the non abraded side on cooling, and the relatively thin oxide grown on the abraded side.

At 600°C there was a rapid initial growth in oxide thickness, which then slows down for the super 304H and 347H FG samples. Both samples showed a slight decrease in growth of the oxide after 250 hours (Figure 4.16). The oxide formed on the 347H FG inner surface was consistently thicker than that formed on the super 304H.

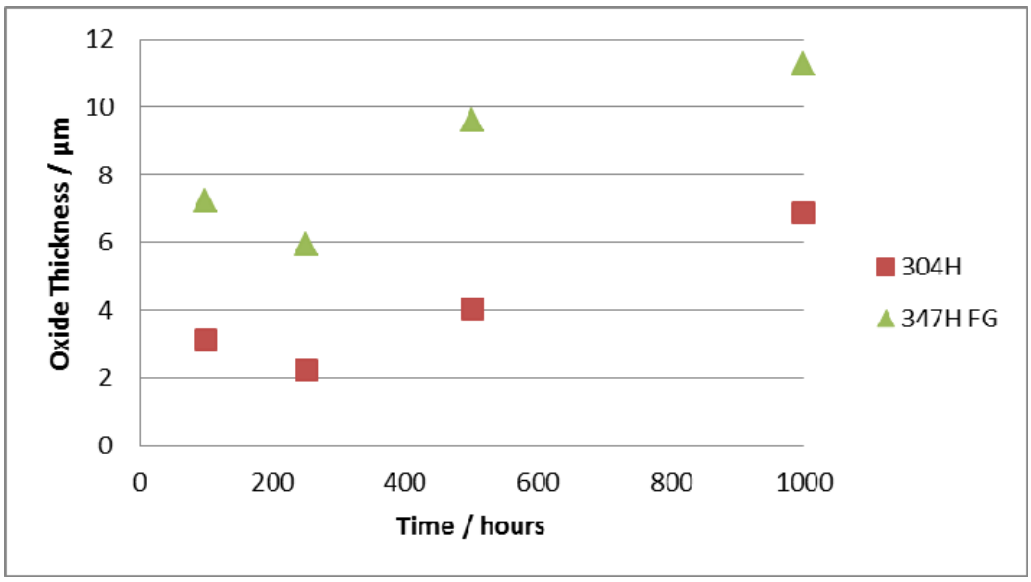

Figure 4.16. Graph showing the average oxide growth for durations up to 1000h at 600°C. Measurements for the shot peened samples could not be taken due to their minute size.

At 650°C the super 304H and 347H FG samples showed a slow growth in oxide thickness after initial rapid growth (after 100h); see Figure 4.17. At this temperature however, the super 304H samples appear to have a thicker oxide growing on them than the 347H FG which is opposite behaviour to these samples at 600°C. The oxide forming on the shot peened sample after 1000 hours was thin but measurable.

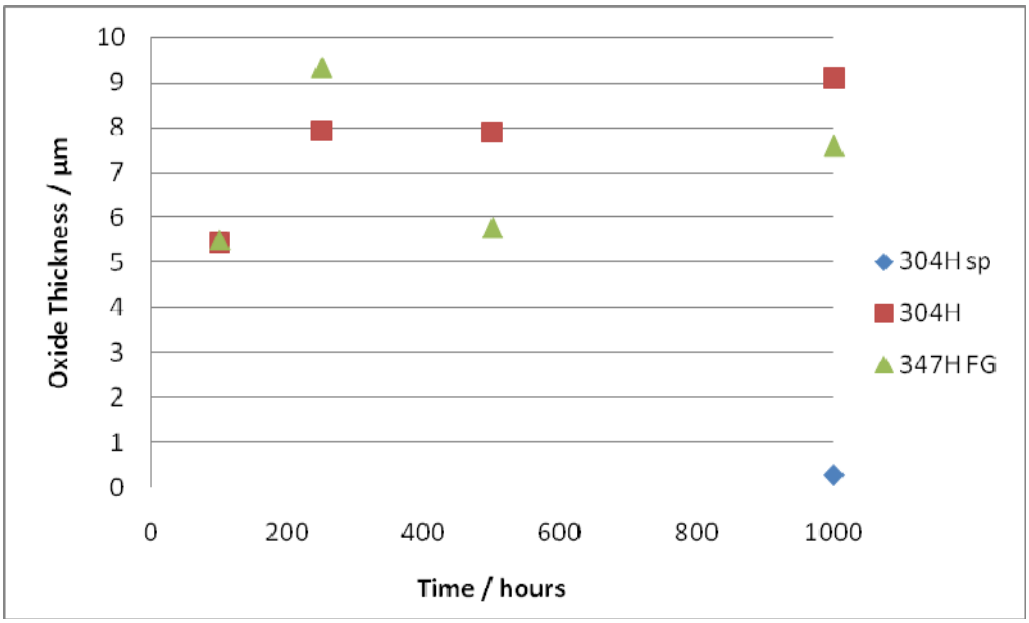

Figure 4.17. Graph showing the oxide growth for durations up to 1000h at 650°C. Measurements for the shot peened samples could not be taken due to their minute size (except at 1000h).

The samples at 700°C also showed a slow increase in thickness after an initial rapid growth with the oxides formed on the super 304H being consistently thicker than the oxides on the 347H FG, Figure 4.18. The oxides formed on the shot peened super 304H were measurable after 500 hours, however no increase in oxide thickness was seen.

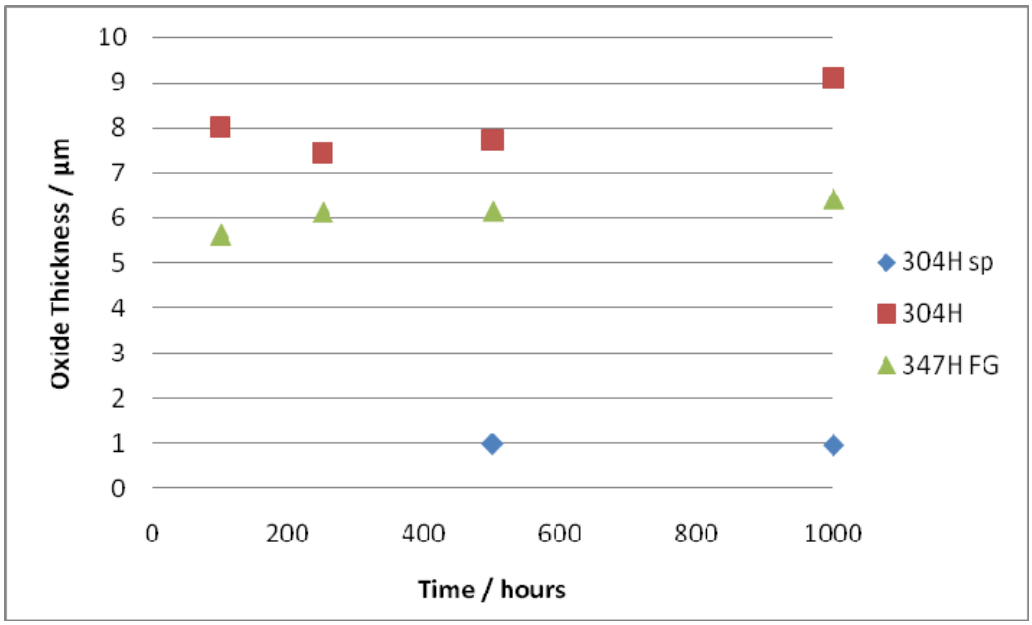

Figure 4.18. Graph showing the oxide growth for durations up to 1000h at 700°C. Measurements for the shot peened samples could not be taken due to their minute size (except at 500h and 1000h).

Figure 4.19 shows cross section examples of the oxide formed on the T92 non abraded side after 100 and 1000 hours at each temperature. At 600°C the T92 non abraded side spalled severely after each duration. Image a.) shows the cross section through a sample oxidised for 100 hours which has remained adherent. The oxide is approximately 70µm thick. Whereas image b.) at 1000h shows a spallated region showing only an inner subscale remaining adherent, of approximately 5µm thick. This remaining adherent inner oxide is also present in image d.) and e.) but is not as obvious in f). The oxide has remained adherent in the cross section area at 650°C after 100h in image c.); however, there is extensive cracking between the inner and outer oxide layers, which will increase the risk of spallation. The oxide consistently spalled on cooling from 600°C and 650°C but remained adherent on most of the T92 700°C samples, including after 1000h as seen in image f.). Here there are small cracks starting to form between the substrate and oxide. The thick oxide remaining on T92 samples is porous and therefore less protective than a dense thinner oxide.

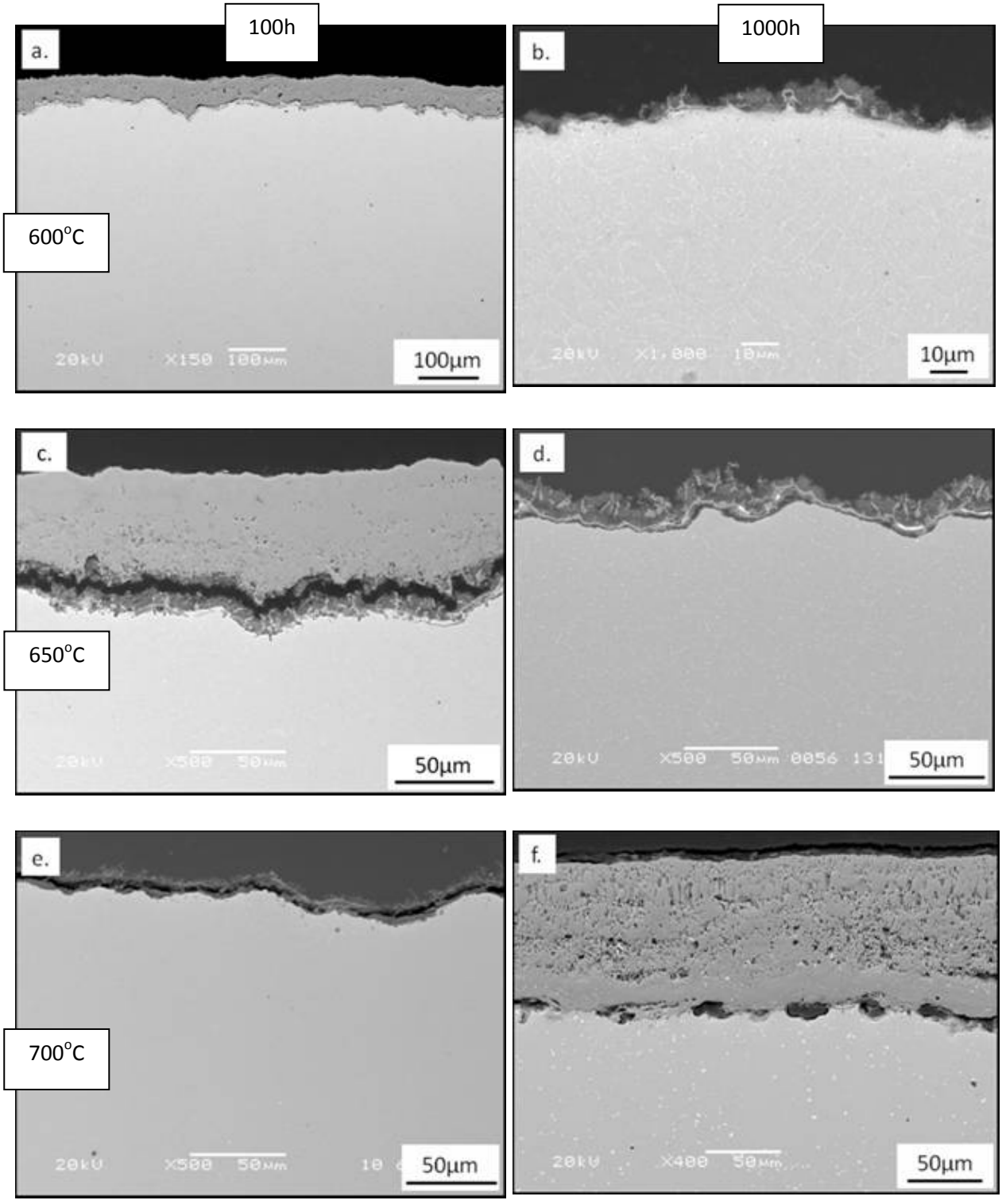

Figure 4.19. Back scattered electron images of the T92 oxides formed on the non abraded side at 600°C after 100h and 1000h (a and b), at 650°C after 100h and 1000h (c and d), and at 700°C after 100h and 1000h (e and f).

Figure 4.20 shows the cross sectional micrographs of oxide formed on the super 304H samples after 100 and 1000 hours at each temperature. It is apparent that after 100 hours the oxide forming in nodular and discontinuous in morphology (a., c., e.). At higher temperatures the oxide nodules are larger and starting to join together. For longer durations such as 1000 hours, the oxide continues to grow both vertically and laterally, so that the intermittent nodules coalesce to form a more continuous, uniform oxide layer as seen in images b.) d.) and f.).

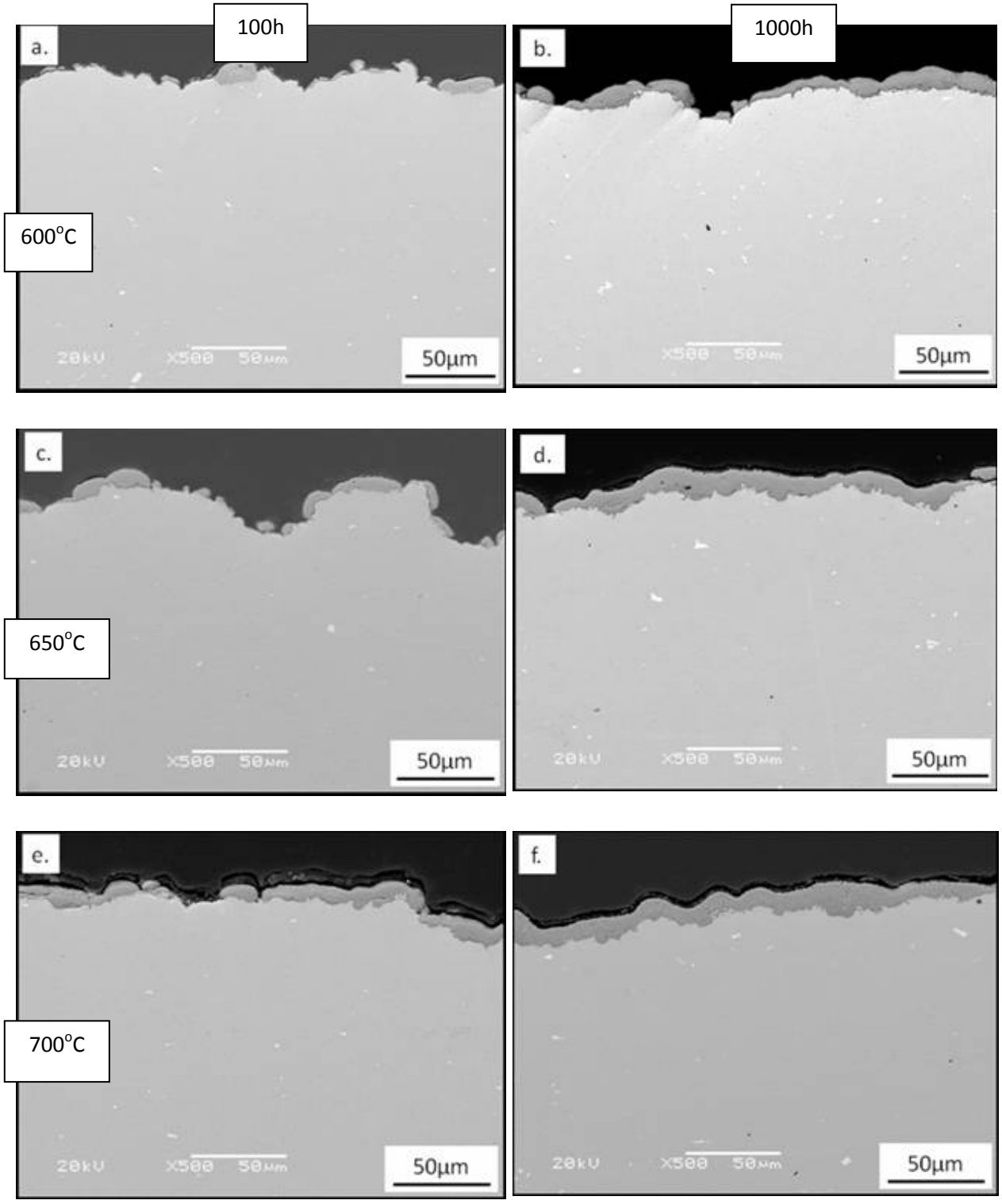

Figure 4.20. Back scattered electron images of the super 304H oxides formed at 600°C after 100h and 1000h (a and b), at 650°C after 100h and 1000h (c and d), and at 700°C after 100h and 1000h (e and f).

The cross sectional analysis of etched super 304H samples revealed the early nodular oxide growth morphology, Figure 4.21. The nodules appear to grow on the individual grains, with the edges of the nodules associated with the grain boundaries in the substrate. At grain boundaries on the substrate surface no visible oxides are apparent at the magnifications and resolution of the SEMs used.

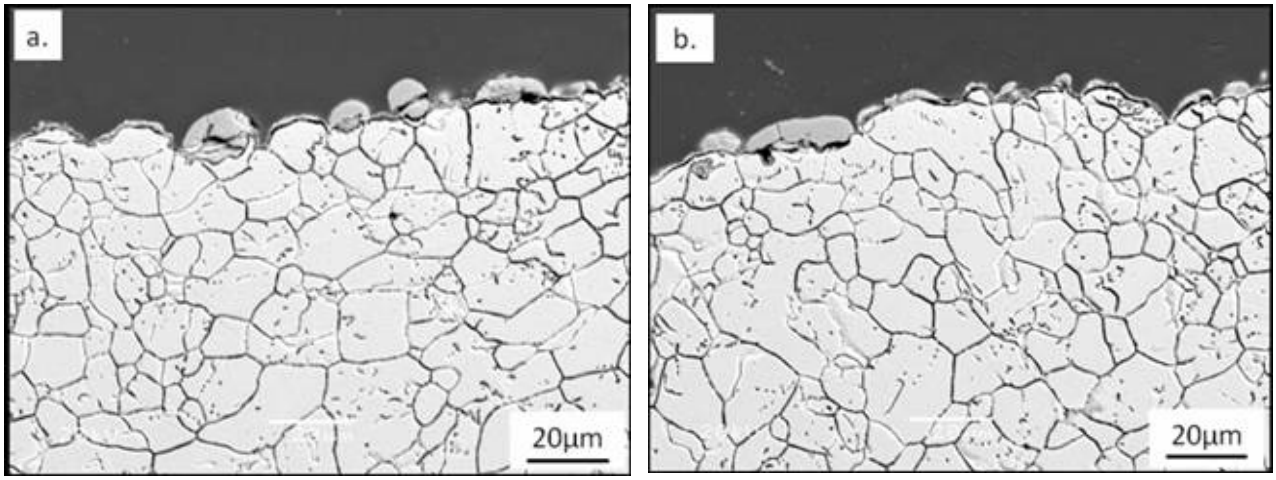

Figure 4.21. Cross-sectional back scattered electron images of super 304H oxidised at 600^{o}C for 100h and electrolytically etched in 10% oxalic acid showing nodular oxide growth in between grain boundaries with no obvious oxides at the grain boundaries.

EDX analysis, Figure 4.22 and Table 4.2, shows that these initial nodules are Fe-rich oxides with a suggested FeO composition containing minimal chromium. The standard deviations for the elements with smaller concentrations are large due to EDX sampling elements from the rest of the alloy. This has been observed for small element concentrations throughout EDX analysis.

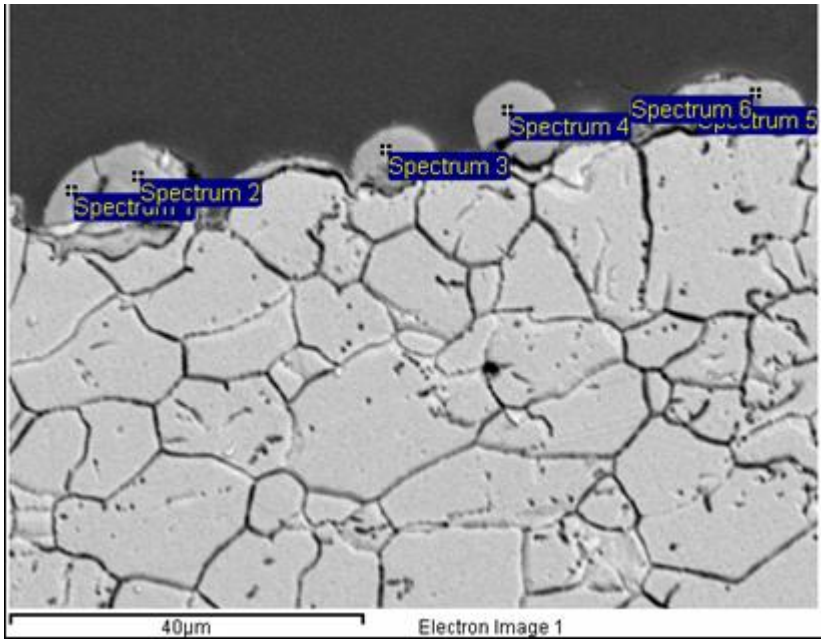

Figure 4.22. The site of interest for the EDX point scans completed on the oxide nodules formed on the super 304H after 100h at 600°C.

Table 4.2. The average EDX point scan results of the super 304H oxide after 100h at 600°C in atomic %.

	O	Si	Cr	Mn	Fe	Ni	Cu
Oxide	47.8 ±2.4	-	2.7 ±3.0	-	49.0 ±2.5	0.5 ±0.5	0.6 ±1.3

The images in Figure 4.23 show cross sectional micrographs of the shot peened super 304H samples after 100 and 1000 hours at each temperature. The smooth shot peened surfaces show little visible oxide forming after most durations. The majority of the cross sectioned samples show a crack to have formed between the resin and the sample surface which was filled with polishing debris and possibly broken oxide. However, at higher temperatures after longer durations visible oxide was recorded (Figure 4.23, f.). This oxide was up to 1µm in thickness and partially delaminated.

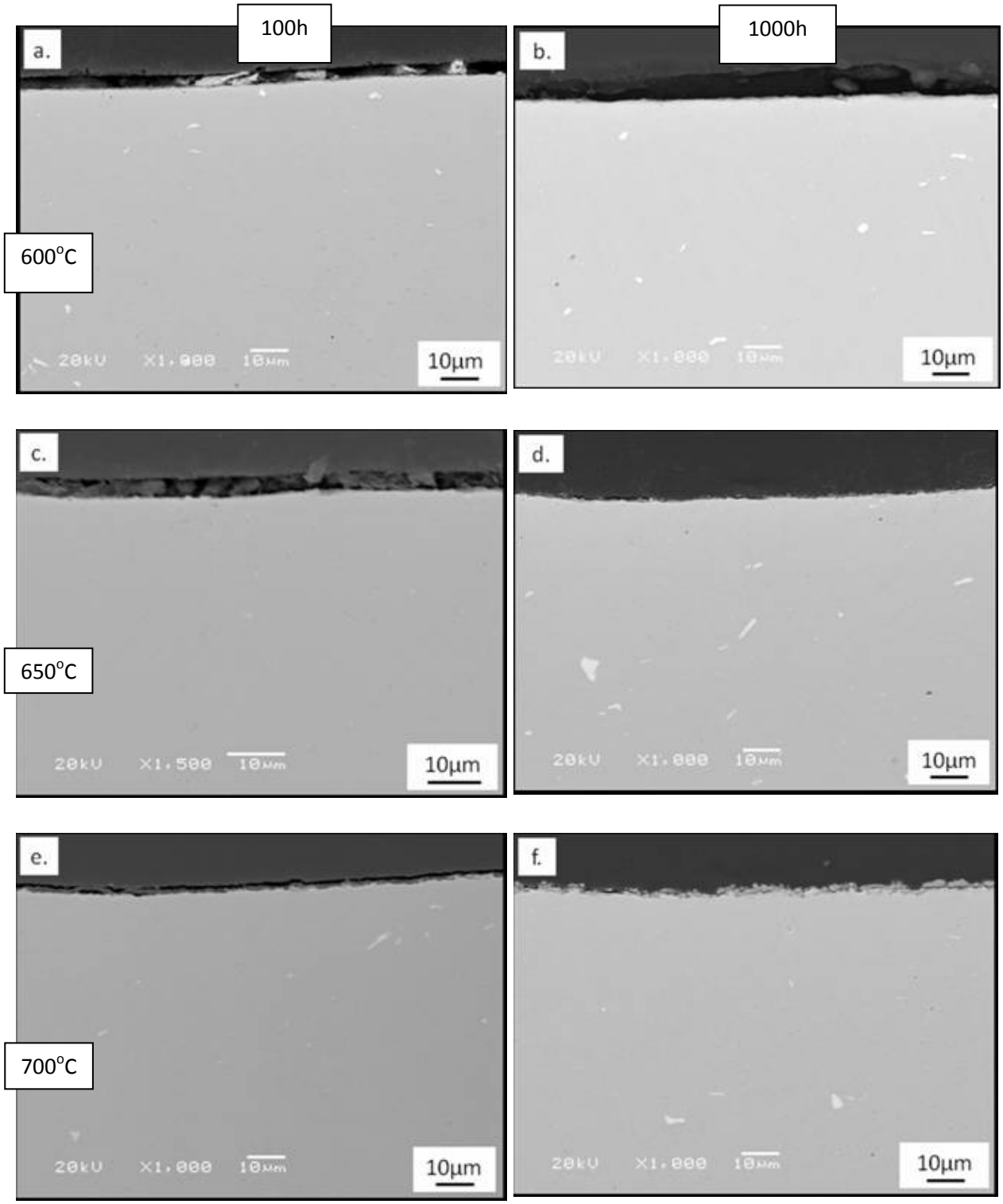

Figure 4.23. Back scattered electron images of the shot peened super 304H oxides formed at 600°C after 100h and 1000h (a and b), at 650°C after 100h and 1000h (c and d), and at 700°C after 100h and 1000h (e and f).

At certain points along the inner surface of the shot peened super 304H tube, indents into the alloy surface were observed, which were full of oxide. Figure 4.24, shows examples of these small crevices or cracks in the surface which experienced large oxide growth which is not consistent with the rest of the smooth shot peened surface. These examples clearly demonstrate the effect of shot peeing on oxidation and the limitations of the process on some features of the tubes.

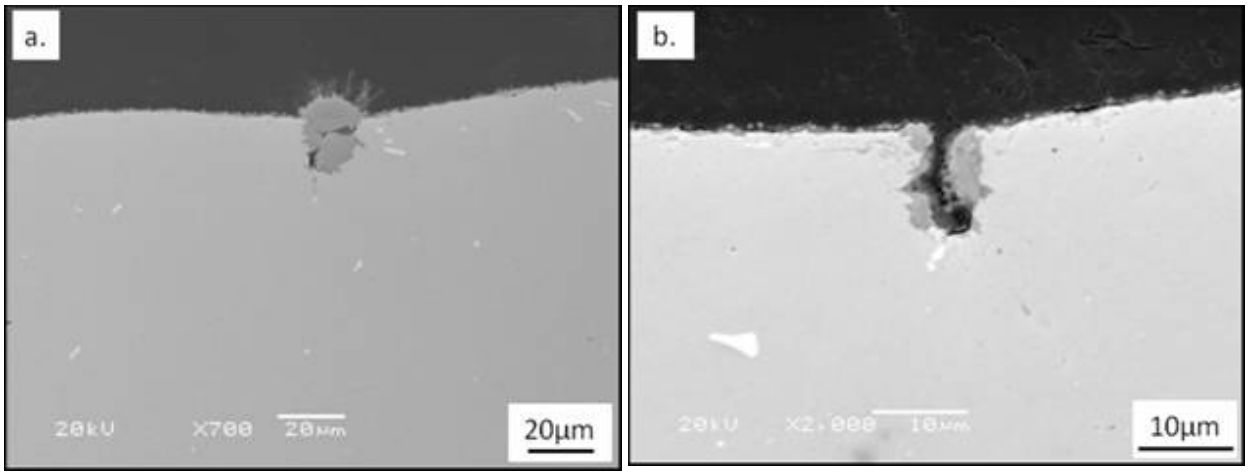

Figure 4.24. Back scattered electron images of the shot peened super 304H showing examples of regions on the surface where the shot peening process has not reached some cracks and crevices showing a pronounced increase in oxidation. Image a.) from exposure to 700^{o}C after 250h and b.) 650^{o}C after 1000h.

Figure 4.25 shows the morphology of the oxide formed on the 347H FG samples after 100 and 1000 hours at each temperature. The thickness and geometry of the oxide is similar to that of the oxides formed on the super 304H samples, however the lateral growth of the nodules formed on the 347H FG appears to occur earlier. After 1000 hours the oxide on the 347H FG becomes more uniform in thickness as it grows. These samples did not suggest a thicker oxide with increasing temperature.

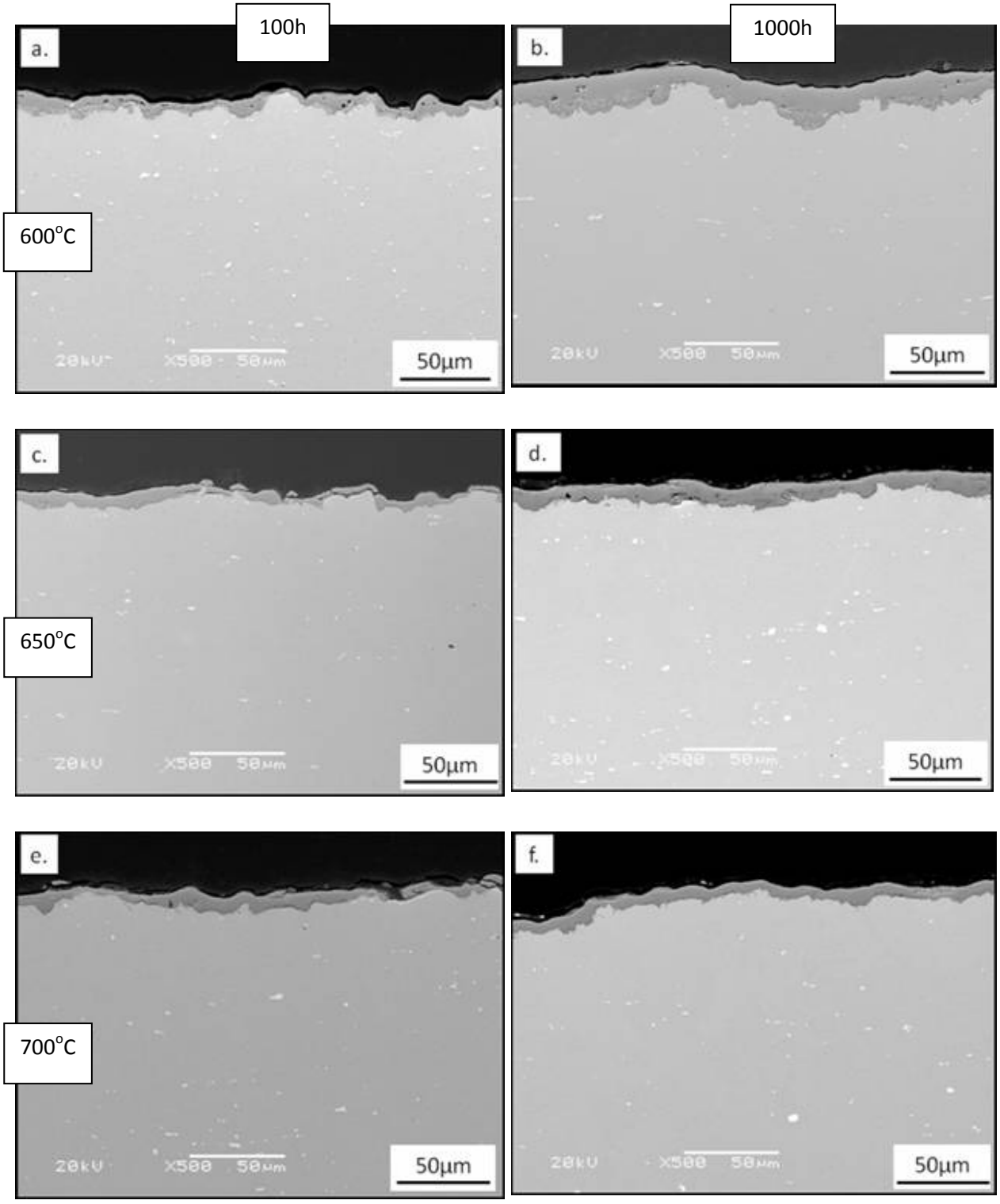

Figure 4.25. Back scattered electron images of the 347H FG oxides formed at 600°C after 100h and 1000h (a and b), at 650°C after 100h and 1000h (c and d), and at 700°C after 100h and 1000h (e and f) showing a more uniform oxide.

4.2.3. EDX Chemical Analysis

Comprehensive EDX cross sectional analysis was performed on each sample to identify the oxides formed after 500 and 1000 hour durations. Elemental line scans were used to ascertain depth profiling as well as point scans to help identify each individual oxide layer (i.e., subscales).

4.2.3.1. T91 Post Service

The post service T91 sample had been exposed to high pressure/temperature steam for thousands of hours and so the oxide formed is much thicker and uniform in appearance. The line scan from the cross sectioned post service T91 (Figure 4.26) showed two distinct subscales equal in thickness, an inner Fe-rich oxide containing Cr, adjacent to the substrate, and an outer Fe-rich oxide containing no Cr. There was also cracking at the interface between the two subscales as seen in Figure 4.27.

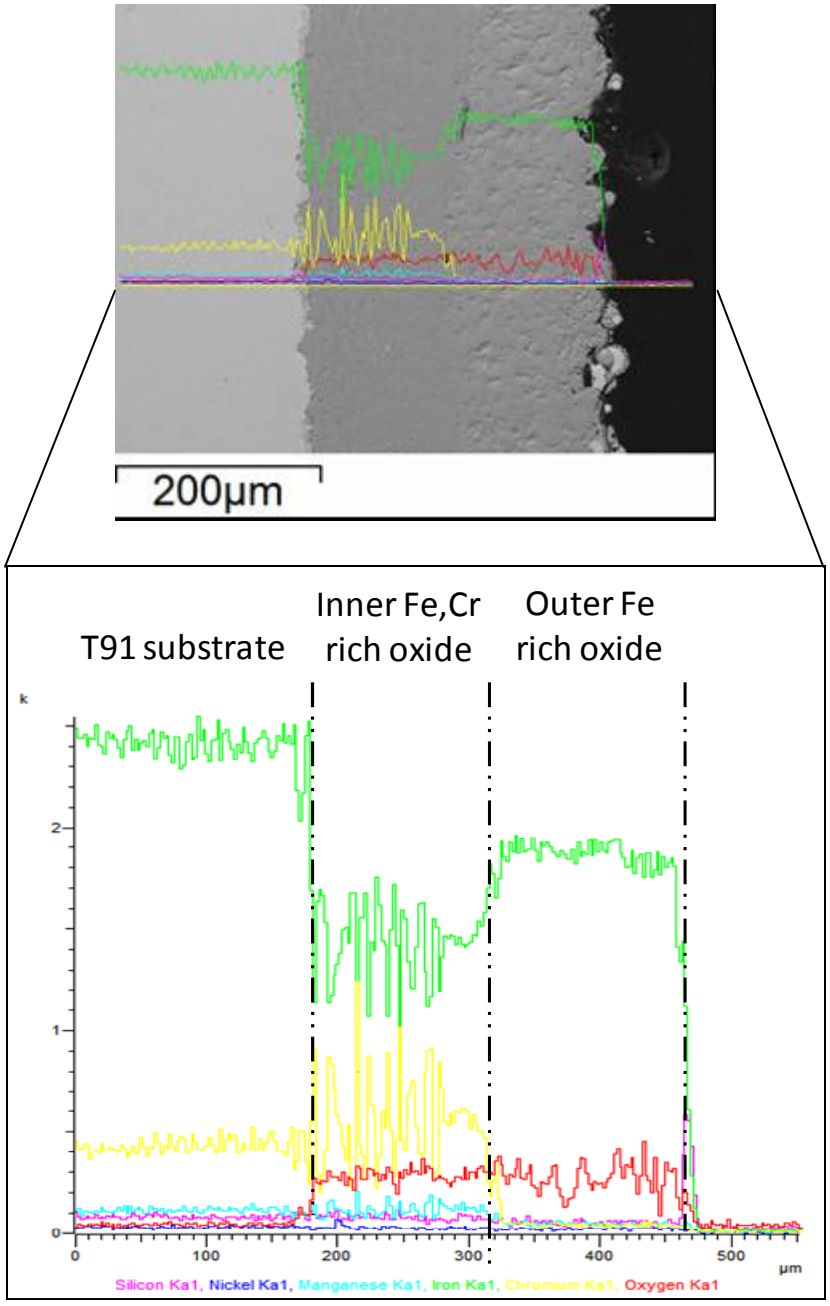

Figure 4.26. An elemental line scan across the T91 post service oxide layer, showing the site of interest and profiles of each element.

The point scans from Figure 4.27 and Table 4.3 could suggest that the inner oxide layer consists of an Fe-rich inner oxide with levels of approximately 10 at-% Cr being detected, and that an outer layer of Fe_2O exists.

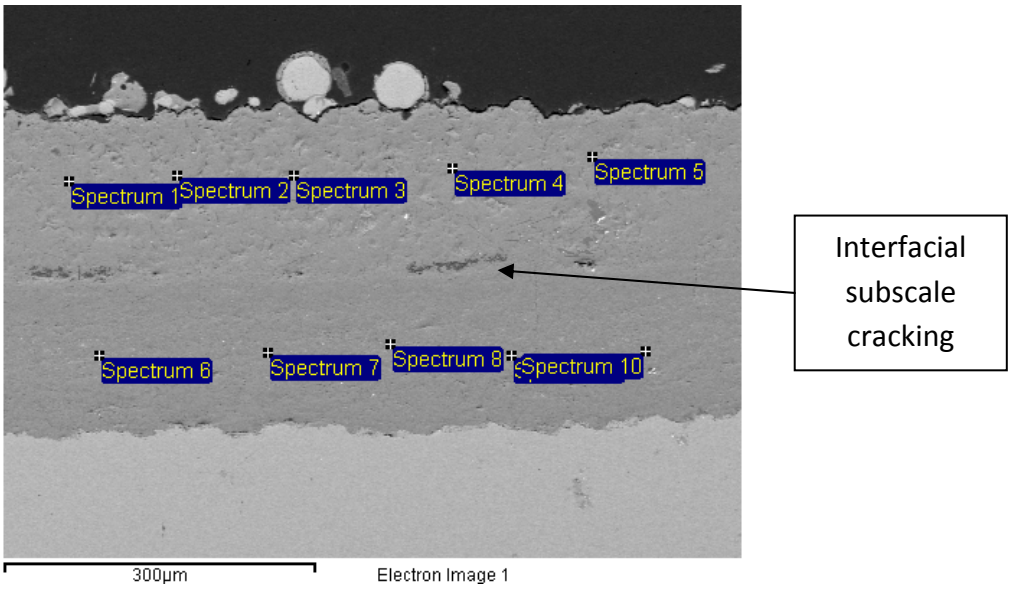

Figure 4.27. The site of interest for the EDX point scans completed on the post service T91 oxide layer along the outer and inner layers.

Table 4.3. The average EDX point scan results of the T91 post service oxide in atomic %.

	O	**Si**	**V**	**Cr**	**Mn**	**Fe**
Outer Layer	31.9 ±1.7	-	-	-	0.3 ±0.0	67.8 ±1.7
Inner Layer	32.4 ±1.7	1.1 ±1.4	0.2 ±0.1	11.8 ±6.7	0.5 ±0.3	54.2 ±7.7

4.2.3.2. T92

4.2.3.2.1. Chemical Analysis of T92 As-Received Sample

The structure of the pre-existing oxide present on the T92 tube in the as received condition was a thick continuous scale with a porous structure, Figure 4.28

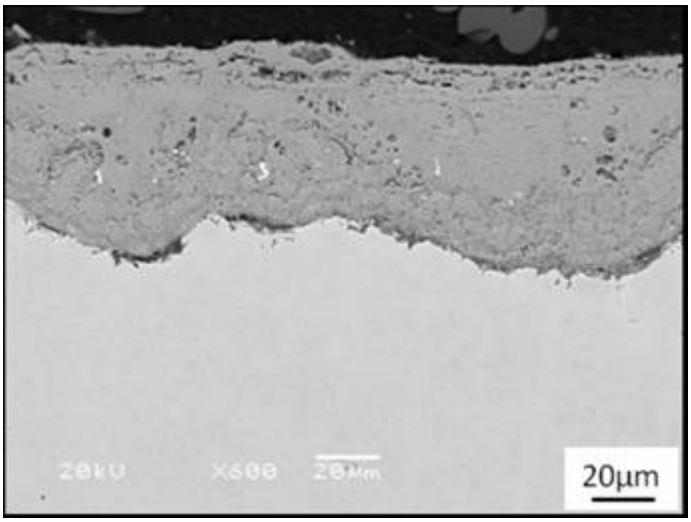

Figure 4.28. Cross section image of the as received T92 sample showing an oxide layer approximately 60µm in thickness, formed prior to being exposed at temperature or put into service.

The line scan through the structure, Figure 4.29, shows a similar two scale oxide morphology as seen in the T91 post service sample. The point scans performed on this oxide, Figure 4.30, Table 4.4, suggest an inner Fe-rich oxide with levels of approximately 11 at-% Cr and an outer FeO oxide layer. These layers are approximately equal in thickness but thinner than the oxide layers formed on the post service T91 sample. Depletion of Cr content in the substrate directly adjacent to the inner oxide layer was detected. A peak in Si was also detected at the outer surface but this was almost certainly polishing debris.

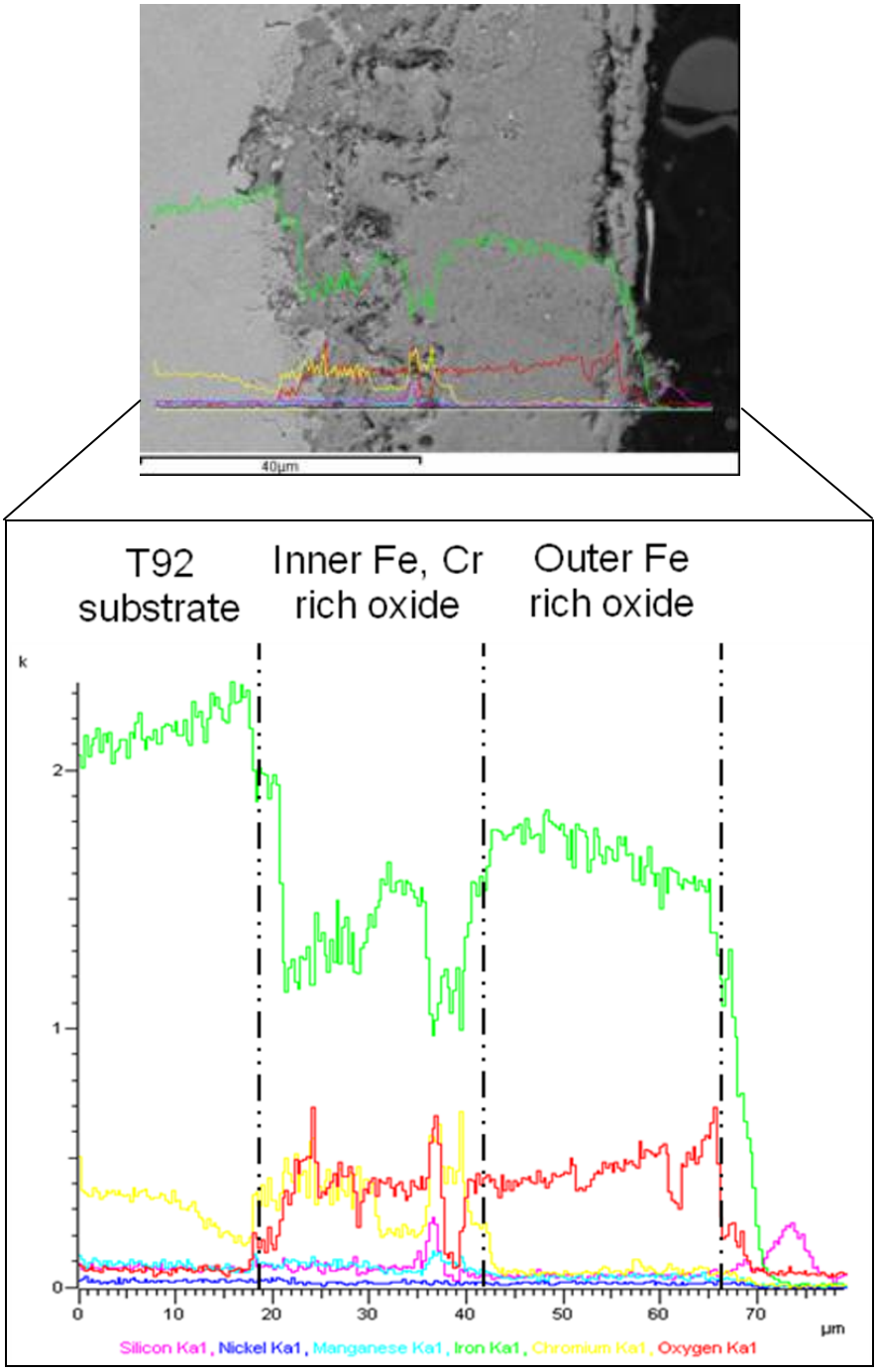

Figure 4.29. An elemental line scan across the T92 as received oxide layer, showing the site of interest and profiles of each element.

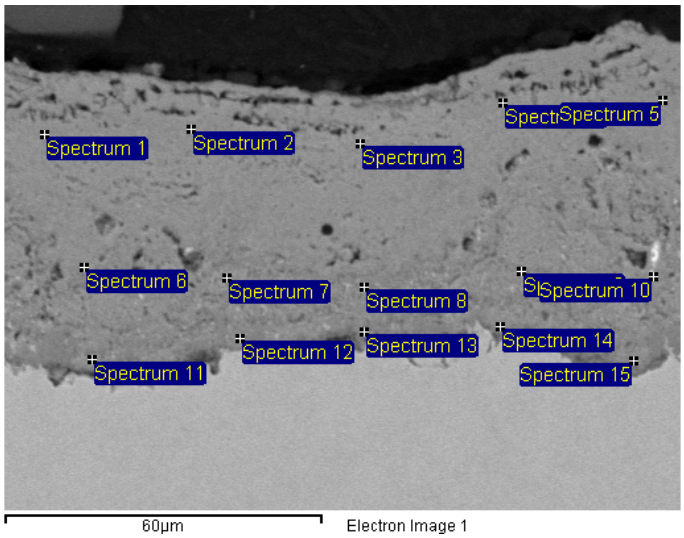

Figure 4.30. EDX point scans completed on the as received T92 oxide layer along the outer and inner regions, and directly adjacent to the substrate.

Table 4.4. The average EDX point scan results of the as received T92 oxide in atomic %.

	O	**Si**	**V**	**Cr**	**Mn**	**Fe**	**Ni**	**W**
Outer Region	45.2 ±2.8	-	-	0.3 ±0.3	-	54.4 ±2.9	-	-
Inner Region	44.0 ±2.1	0.3 ±0.5	0.3 ±0.1	11.0 ±4.9	0.6 ±0.3	43.1 ±6.5	-	0.7 ±0.3
Adjacent to Substrate	44.0 ±3.7	0.1 ±0.2	0.4 ±0.2	14.6 ±7.4	0.9 ±0.4	39.3 ±7.1	-	0.7 ±0.2

4.2.3.2.2. T92 after Exposure

The T92 non abraded side spalled consistently on cooling from 600 or 650^{o}C. However, on cooling after being at 700^{o}C, spallation was drastically reduced. Oxidation on the abraded side was minimal and difficult to detect with the SEM at the lower temperatures, but oxides were noticeable at 700^{o}C after longer durations and showed similar morphology to the double layered as received T92 oxide.

For the T92 samples that did spall on cooling, there was always a remaining oxide layer adherent to the substrate (Figure 4.31). This layer was a Cr-rich oxide and did not appear to consist of any smaller individual layers. The slight etch from the colloidal silica polish revealed grain boundaries (lighter regions) in this remaining oxide which, from the elemental line scan, appear to be associated with Cr-rich peaks. Alloy depletion in Cr and Fe was observed in the substrate.

EDS point analysis (Figure 4.32, Table 4.5) suggests a Cr-rich oxide with levels of approximately 50 at-% Cr being detected. Cr and Fe would suggest mixed oxides or a spinel.

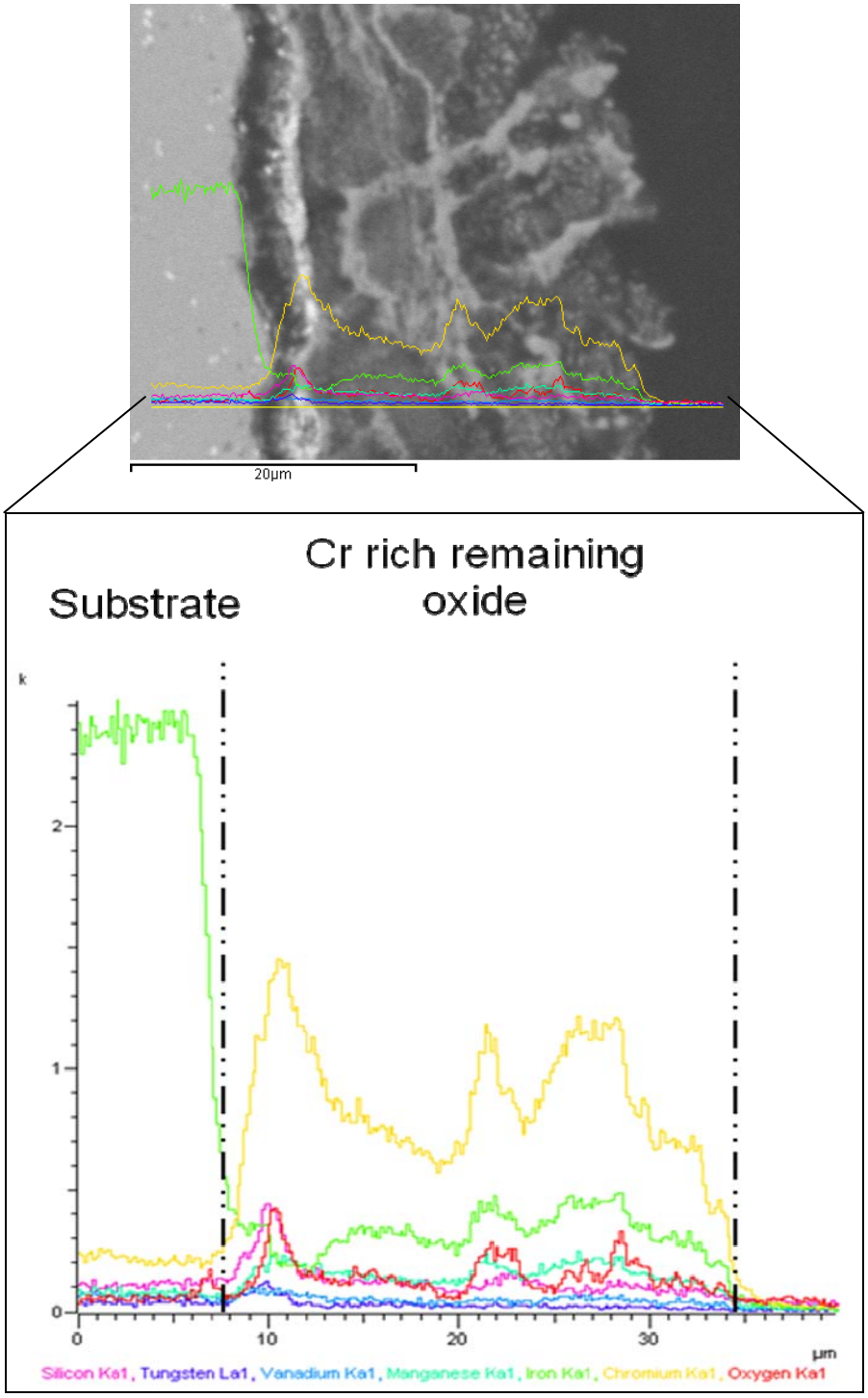

Figure 4.31. An elemental EDX line scan across the oxide formed and remaining after spallation on the T92 non abraded side after 1000h at 650^{o}C showing the site of interest and profiles for each element.

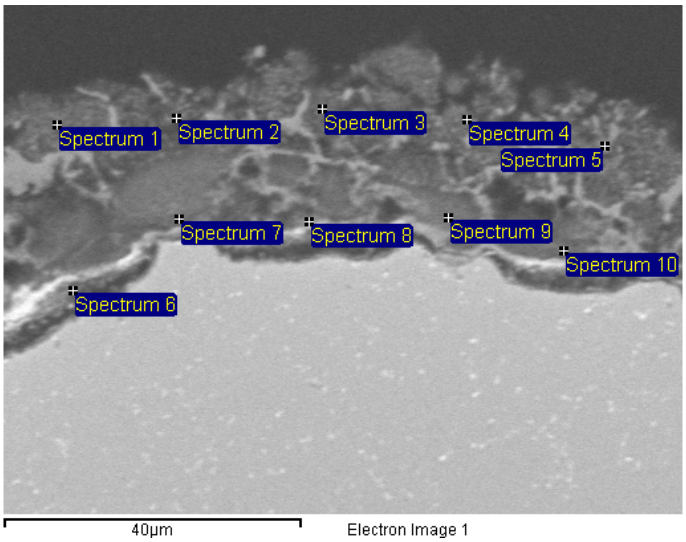

Figure 4.32. The site of interest for the EDX point scans completed on the T92 oxide layer remaining adherent after the non abraded side spalled on cooling after 1000h at 650^{o}C.

Table 4.5. The average EDX point scan results of the T92 oxide after 1000h at 650^{o}C in atomic %.

	O	**Si**	**V**	**Cr**	**Mn**	**Fe**	**W**
Outer Region	22.5 ±2.2	2.4 ±0.4	0.4 ±0.3	47.3 ±1.4	1.6 ±0.3	25.9 ±1.0	-
Inner Region	22.5 ±3.6	1.0 ±0.6	1.3 ±0.8	48.8 ±2.7	1.0 ±0.7	22.5 ±4.2	2.9 ±3.9

Figure 4.33 shows the adherent oxide on the unspalled T92 samples tested at 700 °C and line scan, revealing the same morphology as the original as received T92 oxide. The oxide had two subscales an inner Fe, Cr rich layer and an outer Fe-rich oxide layer.

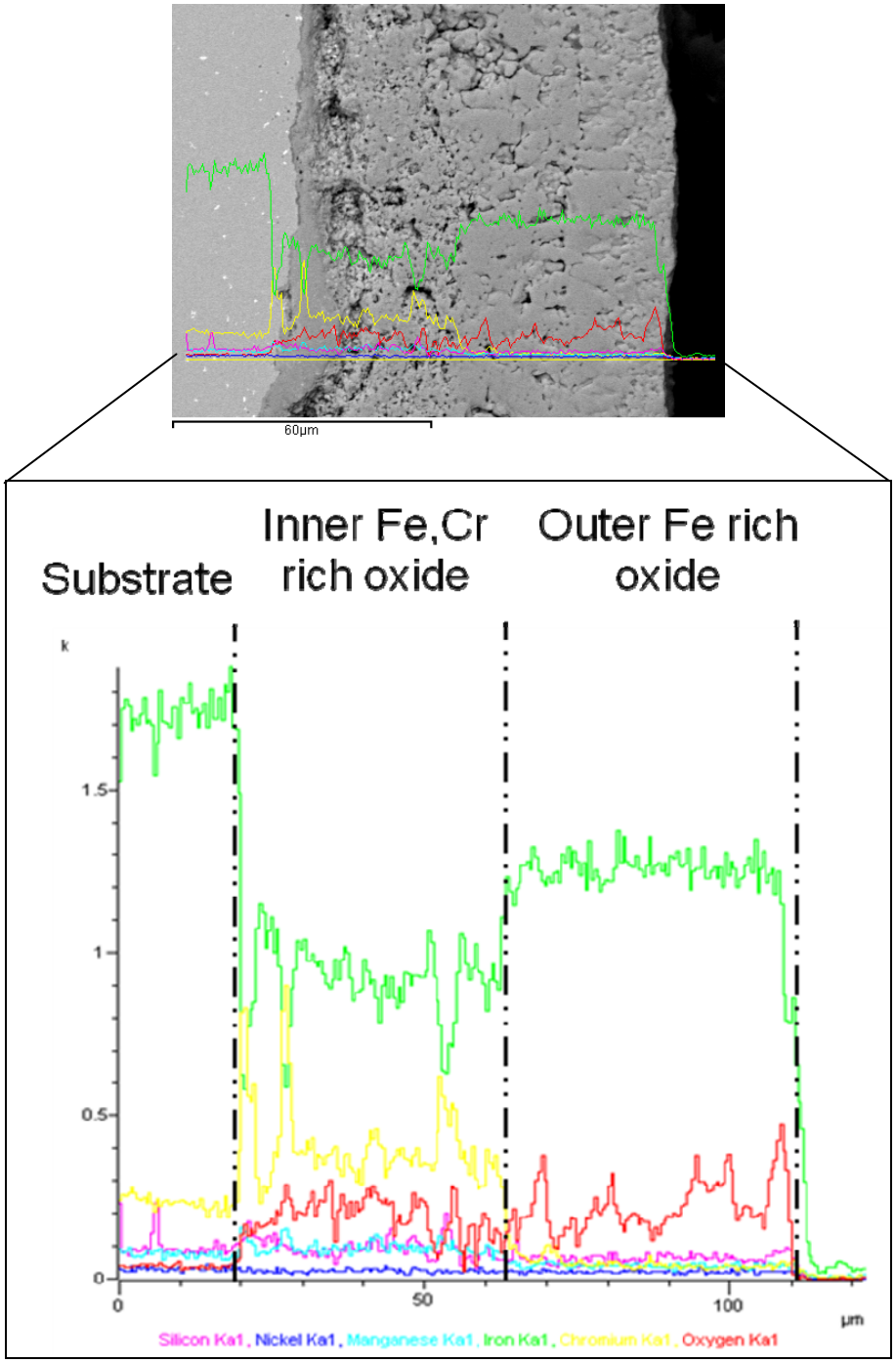

Figure 4.33. An elemental EDX line scan across the oxide formed on the T92 non abraded side after 1000h at 700^{o}C showing the site of interest and profiles for each element.

The point scans (Figure 4.34) on the adherent oxide suggested the inner layer to consist of an Fe-rich oxide containing ~10 at-% Cr, and the outer layer resembling FeO after considering the standard deviations (Table 4.6).

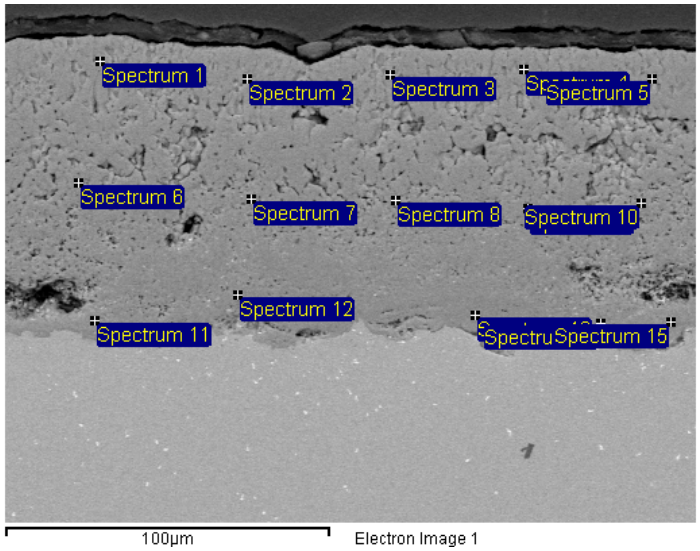

Figure 4.34. The site of interest for the EDX point scans completed on the T92 oxide layer (non abraded) after 500h at 700°C.

Table 4.6. The average EDX point scan results of the T92 oxide (non abraded) after 500h at 700°C in atomic %.

	O	**Si**	**V**	**Cr**	**Mn**	**Fe**
Outer Layer	40.2 ±5.5	-	-	-	0.1 ±0.2	59.7 ±5.5
Inner Layer	34.5 ±3.8	1.8 ±1.3	0.1 ±0.2	12.7 ±4.0	0.6 ±0.0	50.3 ±3.7
Adjacent to Substrate	28.4 ±2.7	0.4 ±0.5	0.4 ±0.3	24.6 ±11.2	0.4 ±0.4	45.8 ±12.5

4.2.3.3. Super 304H after Exposure

The oxide formed on the super 304H samples after testing for 500 and 1000 hours was not uniform. Some areas were thicker containing two subscales of oxide and other areas were thinner with a single oxide layer (Figure 4.35). Line scans were completed through both areas of these oxides.

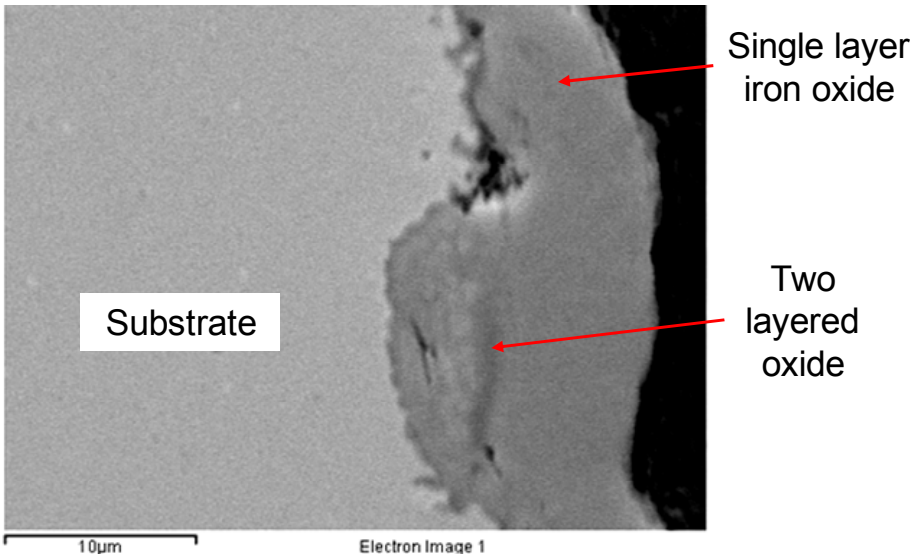

Figure 4.35. Secondary electron micrograph of the oxide formed on the super 304H after 500 hours at 600^{o}C showing the two regions of oxide; the intermittent two layered oxide and the single layer iron oxide.

Regions of the oxide which contained two subscales are represented in Figure 4.36. Similar to the martensitic steels, the oxide consisted of an outer Fe-oxide, however, the inner layer now has a significantly higher Cr content with the ratio of Cr to Fe in this layer from the line scan being greater than the previous martensitic steels. The super 304H oxides also consistently showed a peak in Cr in the inner subscale closest to the substrate. The elemental profile of the inner layer also shows the presence of Ni and Mn. Alloy depletion of Cr can be seen in the substrate adjacent to the inner layer and an oxygen gradient is apparent in the oxide, peaking at the outer surface where oxygen is most abundant.

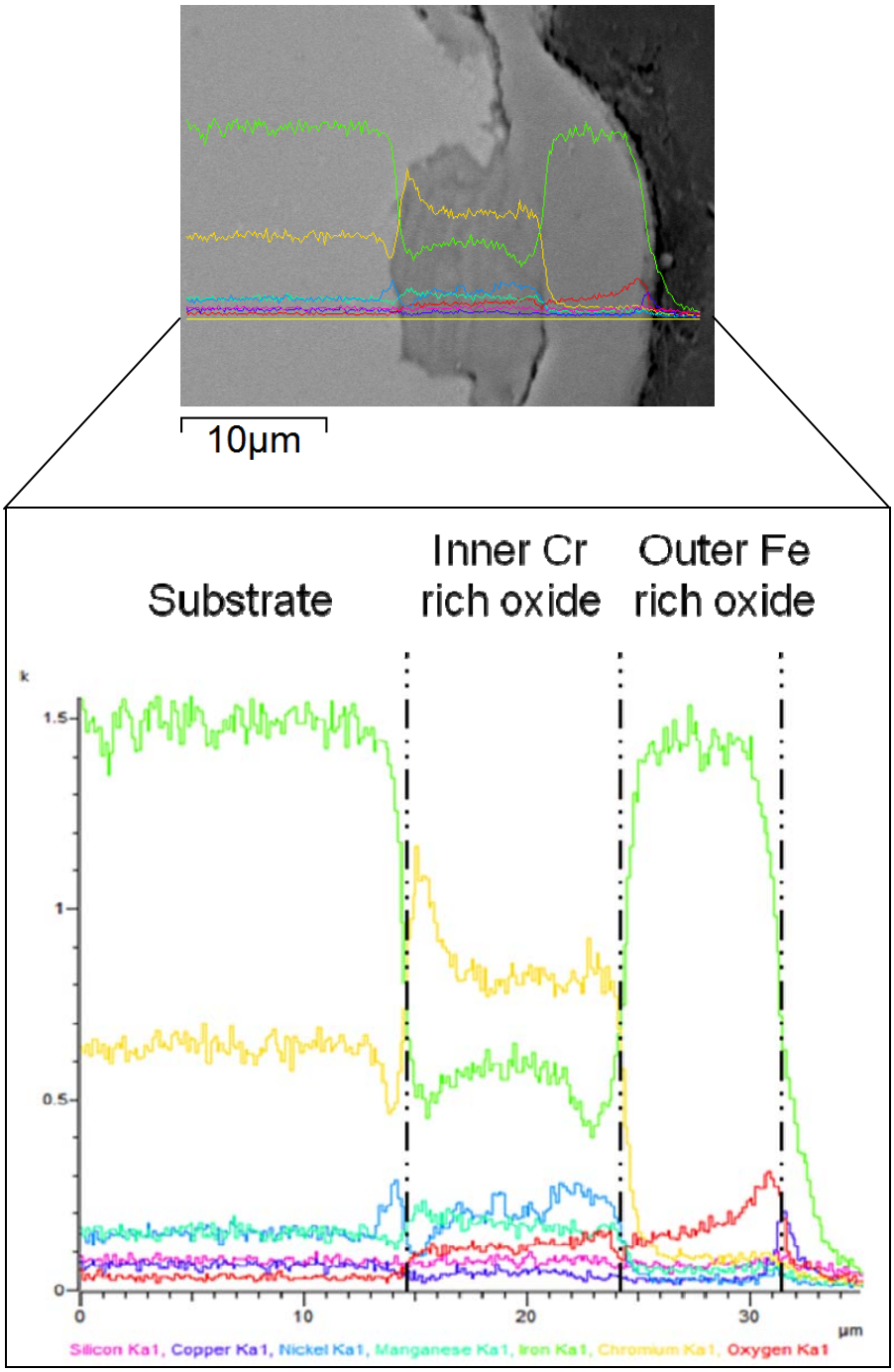

Figure 4.36. An elemental line scan across the double layered oxide formed on the super 304H after 500h at 600°C showing the site of interest and profiles for each element.

EDS point analysis, Figure 4.37 and Table 4.7, suggests the inner oxide resembles a Cr,Fe,Ni spinel type oxide, and the outer layer Fe_3O_2.

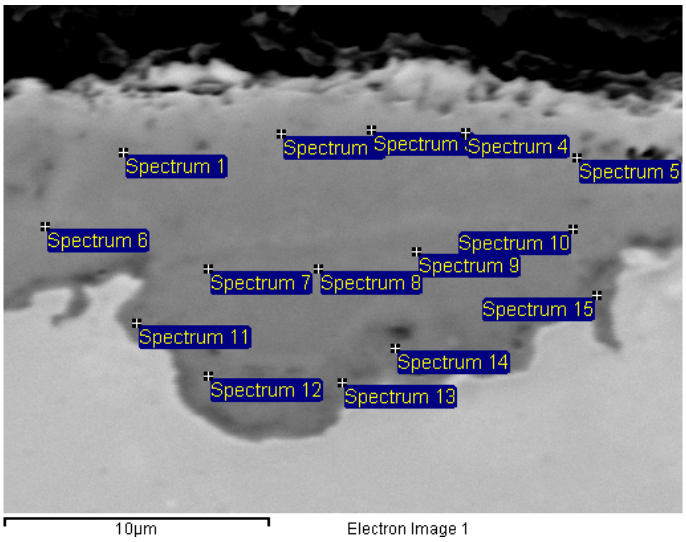

Figure 4.37. The site of interest for the EDX point scans completed on the super 304H oxide layer after 1000h at 650°C.

Table 4.7. The average EDX point scan results of the super 304H oxide after 1000h at 650°C in atomic %.

	O	**Si**	**Cr**	**Mn**	**Fe**	**Ni**	**Cu**
Outer Layer	37.0 ±2.3	-	1.5 ±0.3	0.4 ±0.1	61.1 ±2.4	-	-
Inner Layer	29.9 ±1.1	0.2 ±0.2	29.1 ±2.3	1.1 ±0.1	28.4 ±0.3	9.7 ±0.8	1.6 ±0.4
Adjacent to Substrate	26.5 ±2.7	0.3 ±0.3	44.5 ±2.1	1.2 ±0.5	22.8 ±3.5	4.3 ±2.0	0.4 ±0.4

EDX line scans of the thinner oxide regions on the super 304H specimen show a single oxide consisted solely of an Fe-oxide with a suggested composition of Fe_3O_2, Figure 4.38. The oxygen gradient is present but there is no Cr depletion in the substrate.

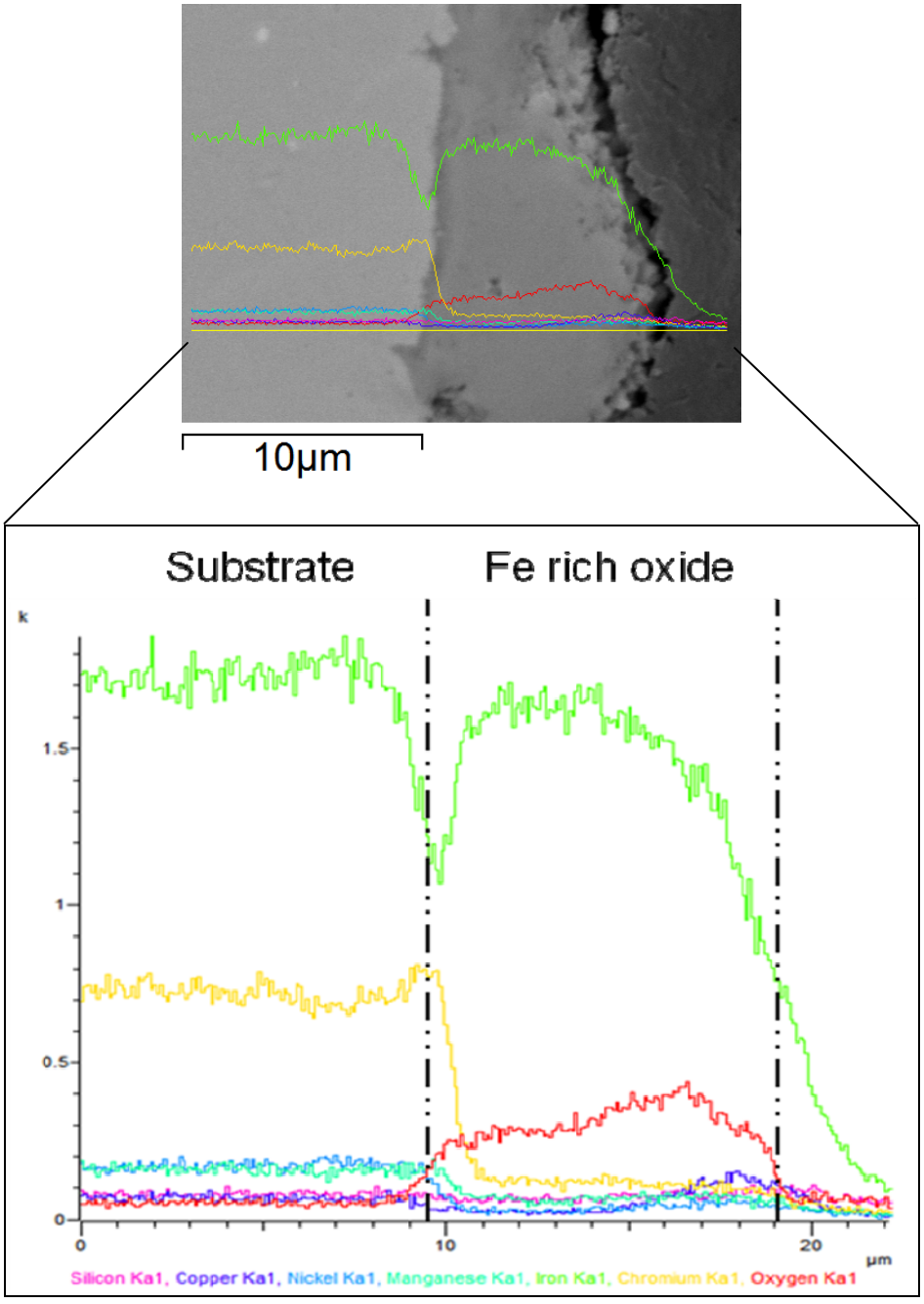

Figure 4.38. An elemental line scan across the single layered oxide formed on the super 304H after 500h at 650°C showing the site of interest and profiles for each element.

4.2.3.4. Super 304H Shot Peened after Exposure

The oxide formed on the shot peened surface of the super 304H exposed at 600°C was irresolvable using the microscopes available. This was consistent with the weight gain data. Due to the smooth shot peened surface, cracking would often occur between the sample and the resin (Figure 4.39) possibly during the sectioning and polishing processes. The Si peak in between the sample and resin can be assumed to be the debris from the polishing procedure.

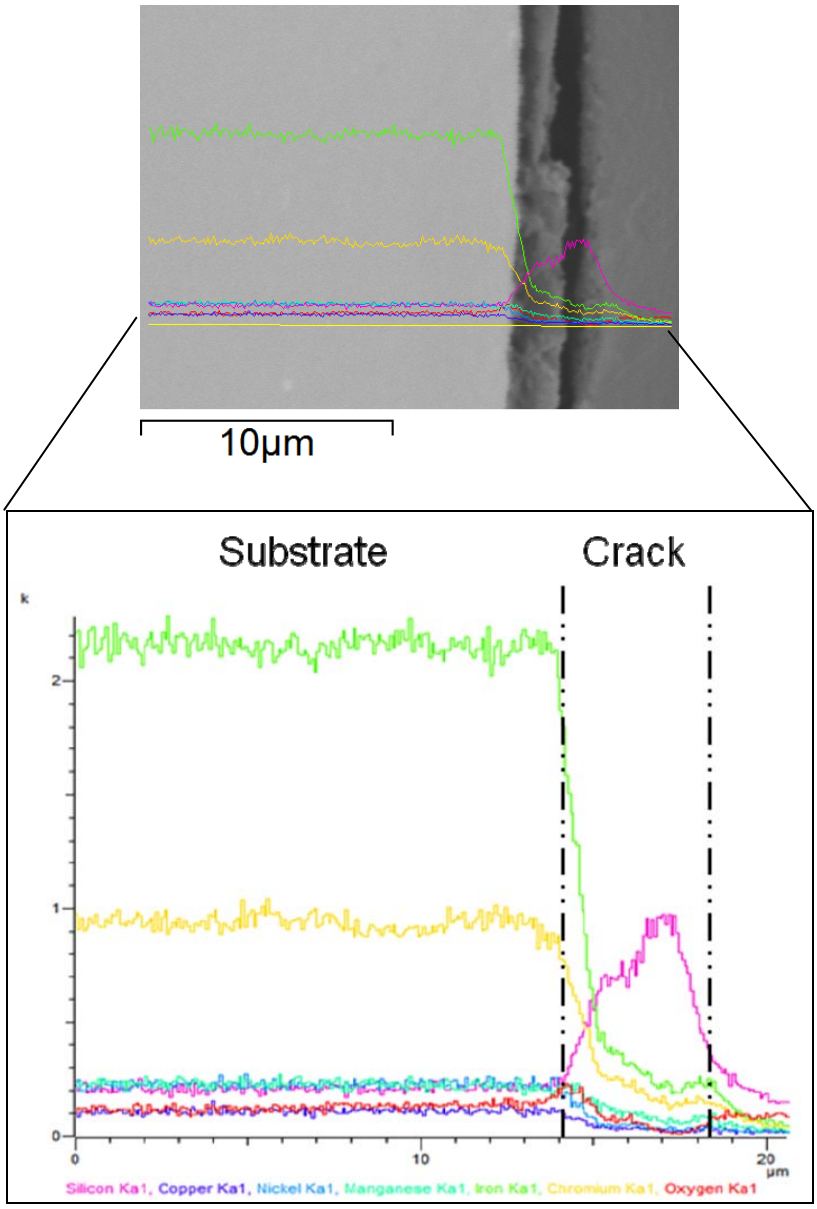

Figure 4.39. An elemental line scan through the oxide formed on shot peened super 304H after 500h at 600°C showing the site of interest and profiles for each element.

At two sites spaced irregularly along the shot peened surface after 700°C exposure, there were regions of thicker oxide forming, Figure 4.40. These sites developed where the shot peening process was ineffective, similar to sites seen in Figure 4.24 and in certain areas of Fig 4.1c. These sites covered an extremely minute percentage of the sample surface and were found on the sample that averaged 1µm in oxide thickness. Line scans revealed a thin two layered oxide, with a Cr-rich inner layer and a Fe-rich outer layer similar to the standard super 304H oxides but on a smaller scale. No significant depletion of chromium was noted in the substrate adjacent to the scale.

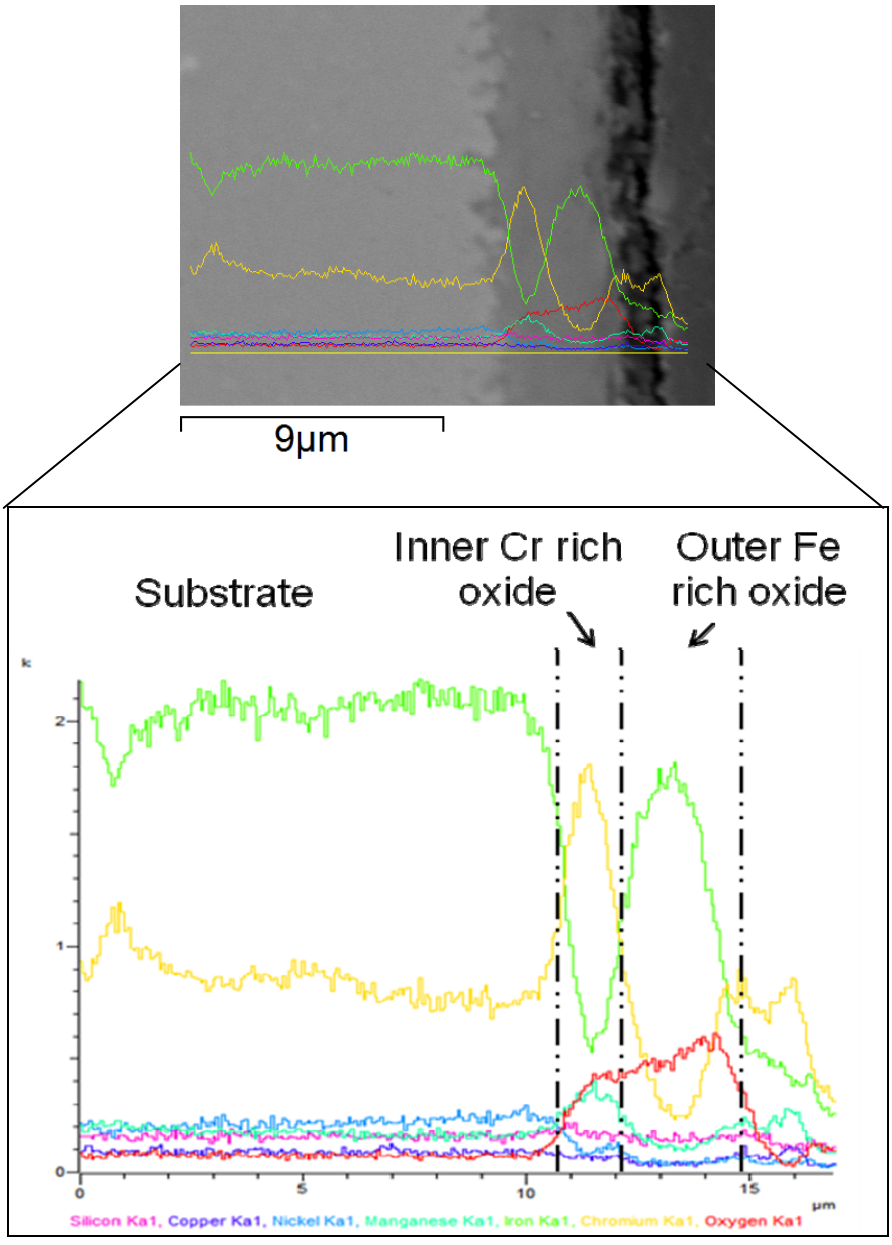

Figure 4.40. An elemental line scan through a region of thicker oxide formed on shot peened super 304H after 500h at 700°C showing the site of interest and profiles for each element.

The EDS point analysis showed two distinct oxide compositions with a significant Cr content in the outer Fe-oxide also as seen in Figure 4.41 and Table 4.8. The inner oxide composition could also contain substrate information, due to its proximity.

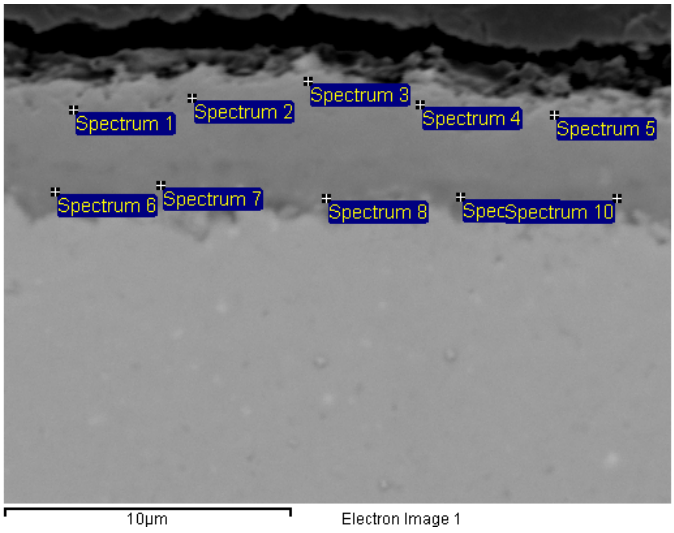

Figure 4.41. The site of interest for the EDX point scans completed on the shot peened super 304H oxide layer after 500h at 700°C.

Table 4.8. The average EDX point scan results of the shot peened super 304H oxide after 500h at 700°C in atomic %.

	O	**Si**	**Cr**	**Mn**	**Fe**	**Ni**	**Cu**
Outer Region	43.2 ±4.4	-	13.0 ±5.8	1.4 ±0.4	41.0 ±10.9	0.7 ±0.6	0.8 ±0.8
Inner Region	34.7 ±2.2	0.3 ±0.3	21.0 ±5.3	1.9 ±0.6	36.7 ±7.2	4.0 ±1.9	1.3 ±0.7

The oxide formed on the shot peened super 304H surface after longer durations (1000 hours) at 700°C was a visible Cr-rich single layered oxide (Figure 4.42). The scan also revealed a slight peak in Mn in this Cr-rich oxide.

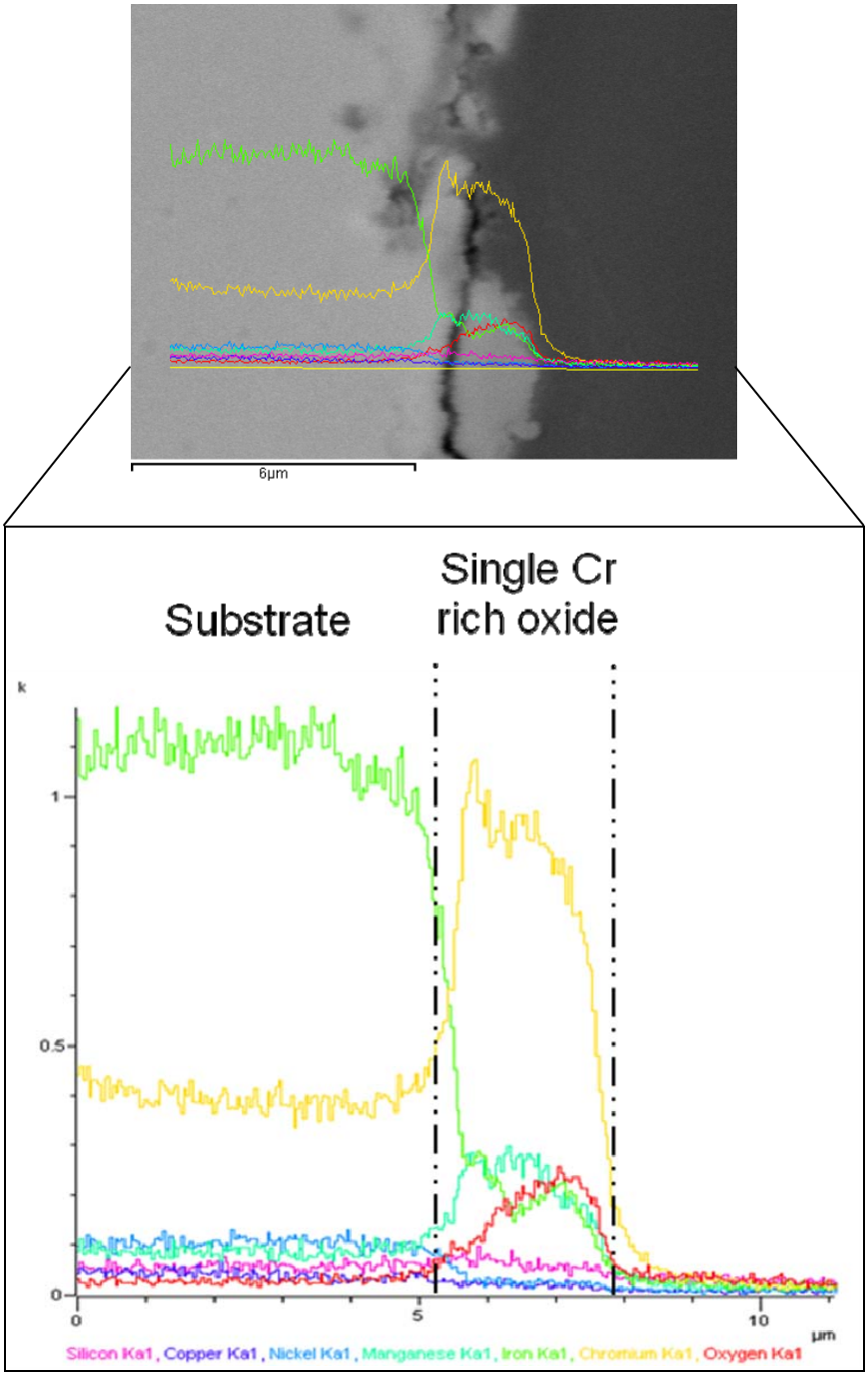

Figure 4.42. An elemental line scan through the single layer oxide formed on shot peened super 304H after 1000h at 700°C showing the site of interest and profiles for each element.

The point scan (Figure 4.43) on this Cr-rich oxide showed a Cr content of approximately 40 atomic % (Table 4.9) which is greater than the previous Cr-rich inner layers seen on the standard super 304H samples, with a suggested an inner oxide layer rich in both Fe and Cr.

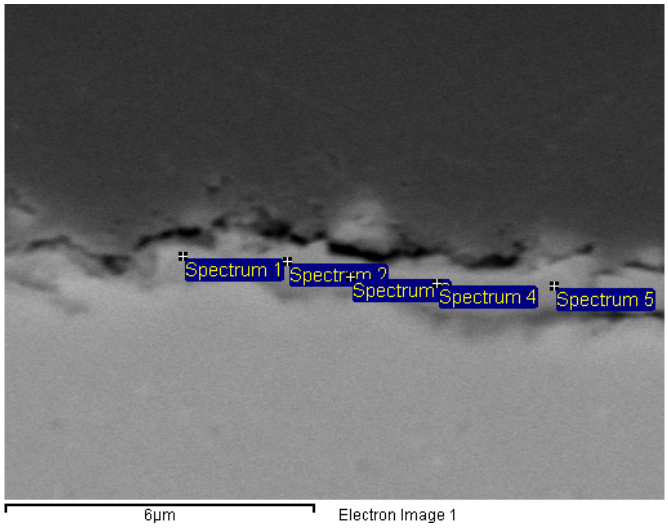

Figure 4.43. The site of interest for the EDX point scans completed on the shot peened super 304H oxide layer after 1000h at 700°C.

Table 4.9. The average EDX point analysis of the shot peened super 304H oxide after 1000h at 700°C in atomic %.

	O	**Si**	**Cr**	**Mn**	**Fe**	**Ni**	**Cu**
Oxide Layer	33.8 ±2.6	3.9 ±1.8	36.1 ±4.9	2.6 ±1.3	20.3 ±2.9	2.1 ±0.4	1.2 ±0.8

4.2.3.5. 347H FG after Exposure

The oxides formed on the 347H FG differed from the 304H oxides, as they were continuous along the surface with a more uniform thickness. The line scans performed on the 347H FG oxides were consistent at both 500 and 1000 hours, with the only difference being thickness, as the oxides grew with time. The oxides had two distinct subscales similar to the 304H samples, with an inner Cr-rich oxide and an outer Fe-oxide layer. The ratio of Cr to Fe in the inner layer was very high compared to the martensitic steels. At 600°C the inner oxide layer also contained Ni peaks suggesting that this layer is a Fe,Cr, Ni oxide (Figure 4.44). In the outer layers the only elements found were Fe and oxygen. An oxygen gradient was seen and no Cr depletion in the substrate.

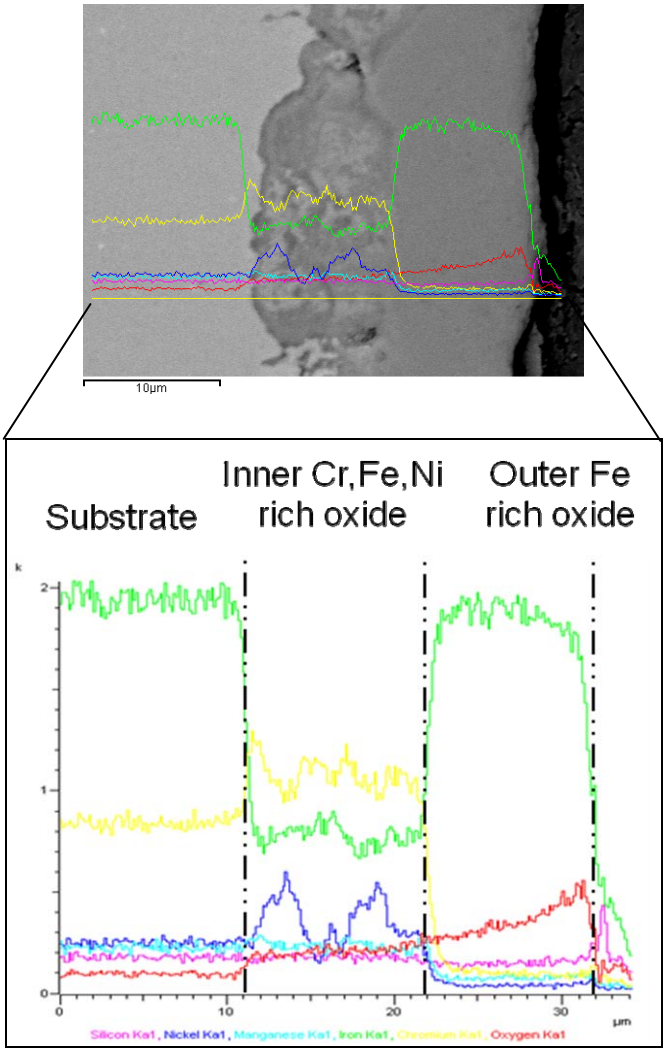

Figure 4.44. An elemental line scan across the oxide formed on 347H FG after 1000h at 600°C showing the site of interest and profiles for each element.

The EDS analysis from Figure 4.45 shows the inclusion of Ni in the Cr-rich inner layer also (Table 4.10).

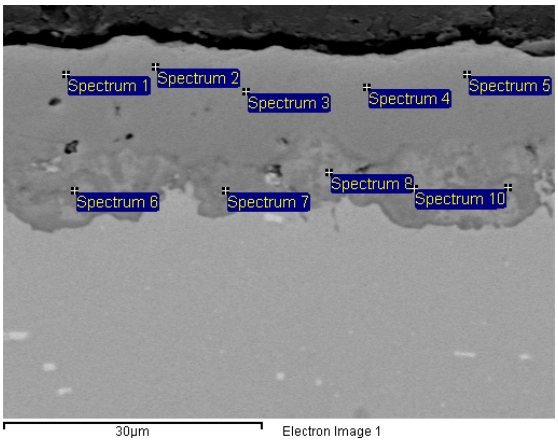

Figure 4.45. The site of interest for the EDX point scans completed on the 347H FG oxide layer after 1000h at 600°C.

Table 4.10. The average EDX point scan results of the 347H FG oxide after 1000h at 600°C in atomic %.

	O	**Si**	**Cr**	**Mn**	**Fe**	**Ni**
Outer Layer	32.5 ±2.2	-	0.8 ±0.1	0.5 ±0.1	66.1 ±2.2	0.1 ±0.2
Inner Layer	20.4 ±2.0	0.8 ±0.7	35.4 ±4.6	2.4 ±1.1	26.7 ±2.9	14.4 ±6.3

At 650 and 700°C the Cr-rich inner layer also appeared to have traces of Mn and enhancement of Ni in the substrate associated with the Cr depletion zone adjacent to the oxide (Figure 4.46). A peak in the Cr concentration in the inner oxide layer suggests the formation of a more concentrated Cr-oxide.

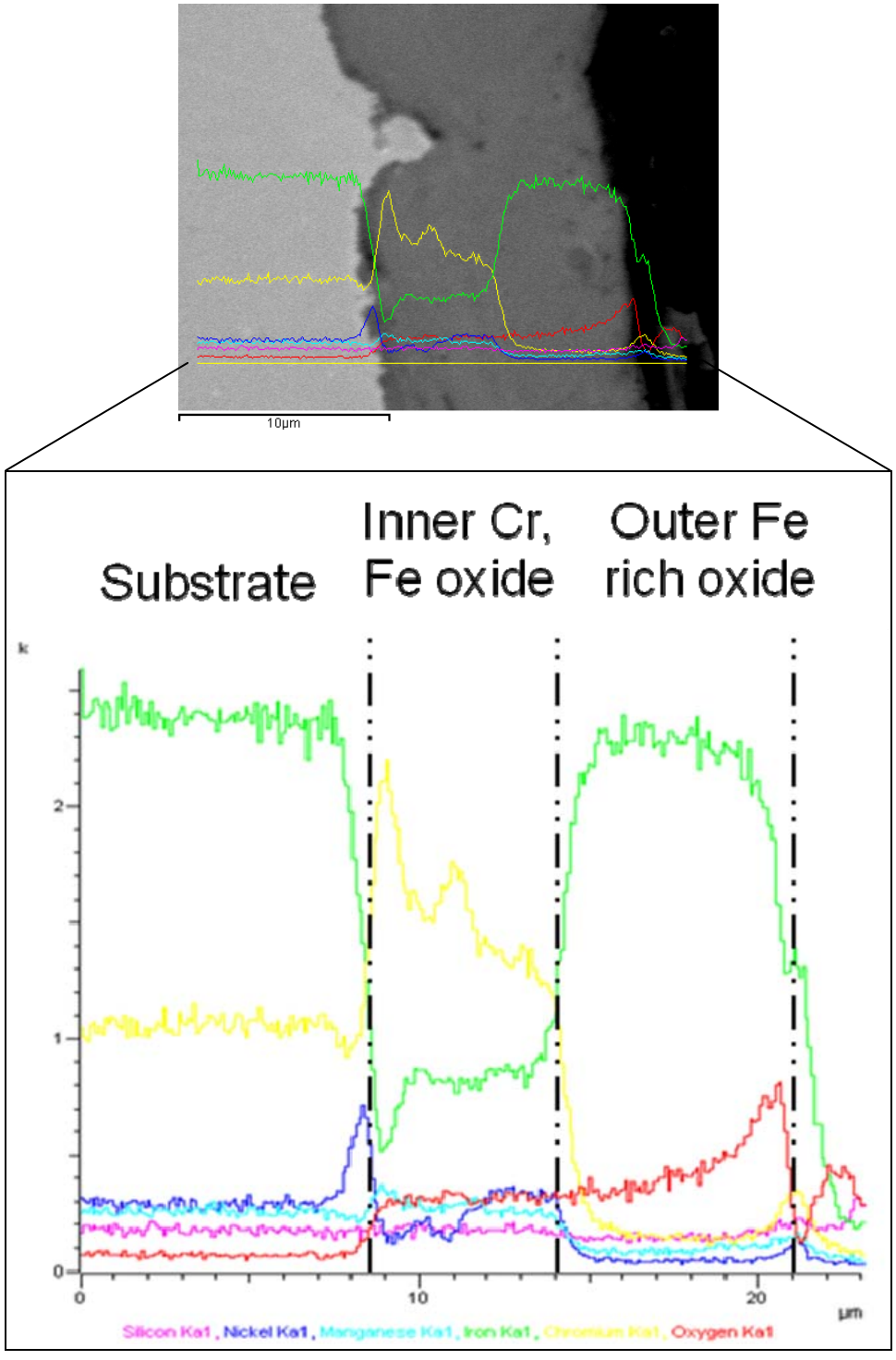

Figure 4.46. An elemental line scan through the oxide formed on 347H FG after 1000h at 650°C showing the site of interest and profiles for each element.

5. Discussion

5.1. The Current Martensitic Steels used In Plant

The T91 and the T92 tubes are both 9 wt-% Cr martensitic steels which are currently used in boiler tube applications in coal fired power plants. The T91 was a post service sample while the T92 tube was received as it would go into plant.

5.1.1. T91

The oxide formed on the T91 tube after 79000 hours in steam service at temperatures of 580^{o}C ±20^{o}C was analysed using both SEM and EDX (Figure 4.26). The double layered oxide formed was extremely thick (approximately 300μm) compared to the other samples. Evidently this was due to being at temperature for a much longer duration, however, the presence of steam was a highly influential factor also. Water vapour is known to increase the rate of oxidation compared to the same reaction in air [17] and its effect is described in more detail in Appendix A.1. Water adsorption and dissociation occurs on the surface of the growing oxides and results in a more permeable scale forming [42]. The pores that are formed in this scale assist fast inward diffusion of oxygen to form new oxide at the metal-oxide interface [42]. The effect of steam by increasing the oxidation kinetics and changing the morphology has been explained through several suggested mechanisms by Fry et al. [43]. These include volatilisation of the iron and chromia hydroxides, the penetration of gas through the oxide, the dissociation of iron oxides, and changes in the oxide defect structure.

Throughout the T91 post service oxide, cracking between the inner and outer scales was also apparent (Figure 4.27). This suggests that when spallation does occur, it will take place at these initiation sites. These cracks are more likely to form in steam, but due to controversy in the literature the exact mechanism is unclear. It is possible that the water vapour reduces the plasticity of the scales formed, which reduces their ability to relieve the induced thermal and growth stresses that can arise in service [9].

The EDX results revealed the outer layer to most probably be Fe_2O_3 iron oxide. The inner layer was Fe-rich but contained a small concentration of Cr forming an Fe,Cr spinel type oxide. Both of these formed oxides lack a significant Cr content, which would have helped to reduce the diffusion rates through the oxide, thus making them non-protective [31]. This is due to the faster cation diffusion through the iron oxides [9]. Therefore the fast growing Fe-rich oxides will increase in thickness rapidly in these aggressive steam environments and are more prone to spallation. The higher risk of spallation is due to the greater mis-match in thermal expansion coefficients of the iron oxide and substrate compared to Cr-rich oxides. The lack of Cr in the oxides formed is due to the relatively small concentrations of Cr in the alloy and the Fe ions being more mobile than the Cr ions [31]. Research has been carried out to recommend a Cr content of over 11 wt-% to enable a protective steam-side oxide to form [15].

5.1.2. T92

The as-received T92 already had a double layered oxide formed on the inner surface of the tube before it had even been exposed to the test temperatures in the laboratory furnaces (Figure 4.28). This could have been due to the prior manufacturing process such as normalising or tempering. The mass change and surface imaging data from the isothermal air oxidation testing showed mass spallation of the T92 samples on the non-abraded side at both 600 and 650^{o}C. However, at 700^{o}C the majority of T92 samples did not spall. When the non-abraded side did not spall, the mass gain on the sample was much greater than that of the austenitic steels (Figure 4.13), suggesting that the oxide growth of the T92 was much faster and consisted of scales with higher cation diffusion rates such as iron-rich oxides. The oxides grown on the abraded side were thinner and therefore less likely to spall. This thinner oxide is possibly due to the cold working occurring during abrasion, enabling a more protective Cr-rich oxide to form.

Some initial spallation of the T92 oxide was apparent upon immediate removal of the sample from the tube furnace before the sample had begun cooling. This type of spallation will be the result of growth stresses occurring within the oxide, causing the brittle oxide to fracture and spall. These stresses are caused by the volume change due to oxidation that is impeded by the geometry of the structure such as the concave inner surface and convex outer surface of the

tubing. The oxide will experience deformation due to the specific volume of the growing oxide not being the same as the volume of consumed metal in the reaction [31].

The majority of the spallation occurred on the non-abraded side during the cooling of the T92 samples. It is in this area that whole segments of oxide would crack and spall completely off when removed from the furnace (Figure 4.9.b). This type of spallation will result from thermal stresses in the oxide caused by differential thermal expansion or contraction in the oxide and the substrate during the temperature drop [31]. The extent of the thermally induced stresses is relative to the size of the temperature change. Therefore, it is assumed the stresses generated on cooling from 700^{o}C would be the largest in the T92 oxides and most likely to spall but this was not the case. The extent of these stresses is also dependent on the difference in thermal expansion coefficients of the oxide and the substrate [31]. These values are usually greater for the oxide and so on cooling of the sample its oxide will experience compressive stresses leading to fracture and spallation [18]. This means the less heating cycles (plant shut downs) the better, as thermal stresses can also cause the spallation of protective oxides.

The oxide on the non-abraded side of the T92 was very porous (Figure 4.34). This type of oxide morphology is non-protective and undesirable due to the fact that oxygen from the atmosphere can travel directly through these pores in the scale to the metal surface [43]. These pores are formed from the cation vacancies left from the diffusion of metal ions to the oxide surface; these vacancies become concentrated and so pores form.

EDX analysis was carried out on the inner surface of the T92 samples at sites of spallation and through the complete adherent oxide. On samples where the non-abraded side had not spalled, the line scans revealed an outer subscale consisting of an Fe-rich oxide and an inner Fe-oxide containing a small amount of Cr (Figure 4.33). This two-layered oxide was very similar in composition to the T91 oxide. The lack of Cr in these iron-rich oxides will enable faster cation diffusion through the scale causing further growth of the rapid growing iron oxide. These scales are less protective than the desired slow growing Cr-rich oxides.

The line scans through the spalled sites on the T92 samples revealed a remaining Cr-rich oxide (Figure 4.31). This could have possibly remained adherent to the surface whilst the Fe-rich oxides have spalled completely off due to the thermal stresses generated on cooling. Another possibility could be that the cracking at the substrate-scale interface has led to oxygen access to the depleted substrate and internal oxidation has occurred due to the inward diffusion of oxygen ions dominating. Several Cr peaks in this remaining oxide layer were observed to correspond with grain boundary-like structures in the scale (Figure 4.31). If so, this would fit the established theory that Cr ions diffuse faster along grain boundaries than through the bulk of the material [28].

5.2. The Proposed Austenitic Stainless Steels

New materials are now needed for the boiler tubes in coal fired power plants due to steam parameters (i.e., temperature and pressure) trending upwards. The proposed materials are austenitic stainless steels with an increased Cr content (18 wt-%) for improved oxidation resistance.

5.2.1. Super 304H

The super 304H samples exhibited a steady mass gain at each temperature. After 500 hours the mass gain consistently reached a plateau, or decreased (Figure 4.8, 4.11, 4.14). This would suggest that after 500 hours when the mass gain has started to level off, a protective oxide is forming which restricts further rapid growth of any non-protective oxides. Decreased mass gain after 500 hours could suggest possible spallation, however this cannot be confirmed as no evidence of spallation was found from visual inspection and microscopy. The mass gain data recorded would be difficult to extrapolate due to the short duration of the tests and the variable coverage of double-layered oxide forming. The thickness measurements also confirm the gradual growth in oxide but were less representative of the oxide due to the nodular discontinuous growth of the oxide. Oxide cross-sectional area mapping would show a more accurate representation of growth in this case.

The back-scattered electron micrographs of the sample cross-section after each duration revealed how the super 304H oxide formed and grew (Figure 4.20). The oxide initially formed in small nodules along the inner surface of the sample. These nodules grew both laterally and vertically until they coalesced to form a continuous oxide layer. Samples which showed initial nodular growth were etched (Figure 4.21). This provided evidence for the location of nodule growth which corresponded with the location of the grain matrix in between grain boundaries. At the grain boundaries there is the possibility of Cr-rich islands forming (that are beyond the resolution of the SEM used) due to the ease of transport of Cr ions. It was evident that different areas on the substrate surface oxidised at different rates. EDX point scans also showed the nodules to have a FeO composition containing no Cr. This pattern of growth has been observed in Ni-20Cr alloys at 600 and 900^{o}C [44]. This research demonstrated that two oxidation stages were occurring (Figure 5.1). The first stage involved the nucleation and growth of NiO on the outer grain surface. This continued to grow over a mixture of oxides (NiO, Cr_2O_3, $NiCr_2O_4$). Much smaller Cr_2O_3 islands formed at the grain boundaries in between the NiO oxides because of the high Cr diffusion rate through the grain boundaries [44]. The NiO continued to grow at 600^{o}C as long as the protective Cr_2O_3 oxide was not a continuous layer. At higher temperatures of 700 to 900^{o}C, the second stage occurred where the formation of a continuous chromia layer begins (Figure 5.1). This is associated with a protective parabolic growth rate behaviour. In this stage, the chromia islands coalesce to form the continuous layer, which then controls the growth by slower diffusion through this layer.

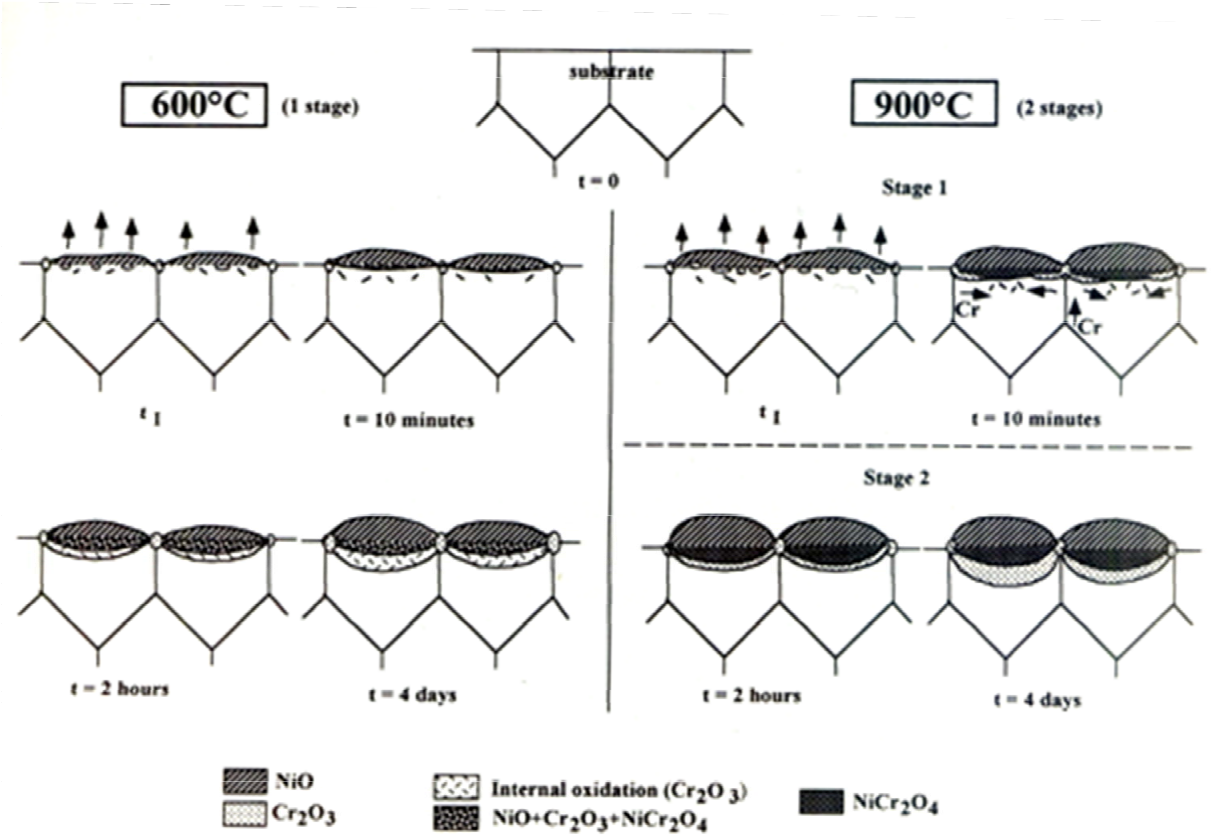

Figure 5.1. A schematic demonstrating the oxide mechanism for the nodular growth on Ni-20Cr alloy [44].

Nodular growth and Cr-rich oxides forming at the grain boundaries has also been demonstrated by Garrett et al. [45] on 18/8 austenitic steels oxidising in carbon dioxide.

This mechanism can be applied to the nodular oxide growth on the super 304H (Fe-Cr alloy), with FeO oxides growing between the grain boundaries on the grains themselves, and chromia forming islands at the grain boundaries due to the increased Cr diffusion along the boundaries. The variation in oxide produced on the surface is reliant on the availability of Cr at the alloy surface [45]. This would explain the different rates of oxidation on the surface and nodular morphology after shorter durations of 100 hours.

EDX line scans were performed on the samples after 500 and 1000 hour durations when the nodules had joined together to form a continuous oxide. The line scans revealed two regions of oxide forming; a single layer of oxide and a double (duplex) subscale region of oxide (Figure 4.35). The single Fe-oxide region (Figure 4.38) is possibly where the FeO nodules have developed into a larger continuous oxide. The double layered oxides formed had an inner Cr-rich layer containing Ni traces and an outer Fe-rich layer (Figure 4.36). This suggests that the fast growing Fe-rich oxide has grown over and engulfed the slower growing Cr-rich oxide nuclei. The Cr-rich inner layer with levels of 30 at-% Cr being detected is more protective. It is slow growing and blocks Fe^{2+} ions diffusing to the outer Fe-oxide and blocks inward diffusion of gaseous impurities [18]. This is due to the transport mechanisms through this scale being generally slow [19]. The Fe found in the inner subscale suggests pure chromia is not forming due to insufficient Cr diffusion to sustain growth of Cr_2O_3; although, a FeCr spinel type oxide has formed, which is still protective to a lesser extent due to the cation diffusion through it also being very slow. However, there still could be the suggestion of some chromia forming due to the significant peaks in Cr found directly adjacent to the substrate in the inner subscale. When the inner Cr-rich layers continue to grow laterally and finally join up to form a continuous inner layer beneath the Fe-oxide (Figure 5.2), the behaviour of the oxide should become more protective (parabolic) and reduce the growth and kinetics of the overlying iron oxide layer and overall oxide. This appears to be possibly starting after 500 hours when the mass gain of the samples starts to plateau. This duplex type oxide forming on the austenitic steels in this study has been reported before on other 18/8 steels [45].

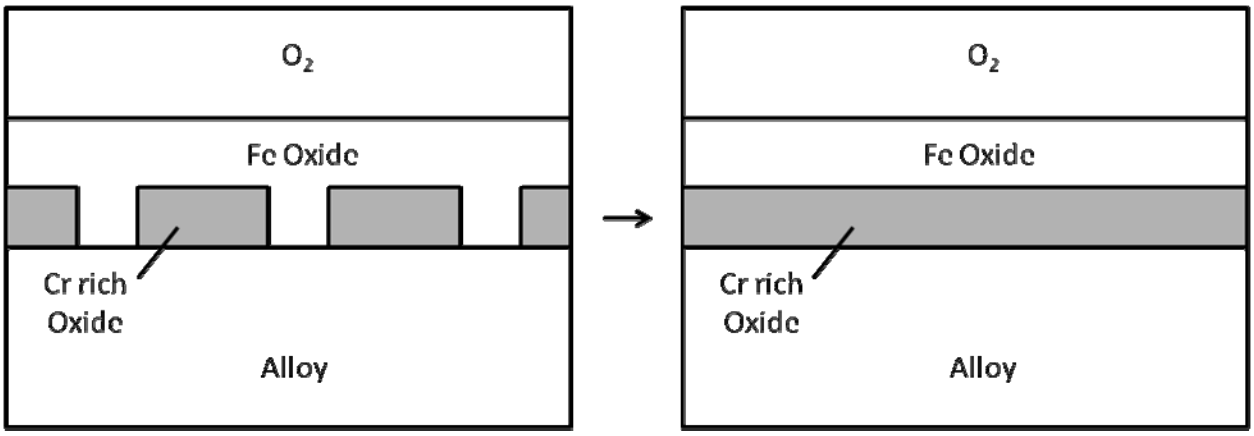

Figure 5.2. A schematic representing the change in morphology during oxide growth on the inner surface of the super 304H tubing.

5.2.2. Shot Peened Super 304H

The shot peened super 304H samples demonstrated the least mass gain at each temperature (Figure 4.8, 4.11, 4.14) and significantly thinner oxide scales on the inner surface of the tubing (Figure 4.17, 4.18). When considering mass gain, it is important to note that this measurement is from the whole six sided sample and not just the inner shot peened surface. However, if the specific mass gain of the isolated shot peened surface was recorded then this would be expected to be lower still, highlighting the strong effect of shot peening on oxidation. Visual inspection and microscopy analysis also revealed no apparent signs of spallation. These findings alone provide evidence that shot peening significantly improves the oxidation resistance of the super 304H steel tubing and these thinner oxides are less likely to spall due to a smaller volume change on cooling. The mechanism behind the improved oxidation resistance is due to the grain boundaries. The shot peening process involves cold working to the inner surface of the tube which introduces compressive stresses locally, reducing the chance of spallation. During this process, it also alters the microstructure of the surface grains of the metal (Figure 4.6) refining them into sub-micron to nano-sized grains [28]. These minute grains are formed from dislocation activities from the shot peening stress causing sub-grain boundaries (the short circuit paths) which form these nano-sized grains [46]. These ultra-fine grains created from the shot peening process increase the grain boundary density in the sub-surface region, which causes an increase in Cr diffusivity along these grain boundaries [28]. This promotes the formation of the slow growing protective chromia or Cr-rich oxides. These protective oxides prevent the growth of iron oxides such as Fe_3O_4, which have a greater mis-match in thermal expansion with the substrate, and so are more likely to spall [28].

This mechanism can be applied to the results from the shot peened 304H samples. The EDX analysis on the oxides that grew to a visible thickness at the higher temperatures demonstrated Cr-rich oxides forming with little Fe detected (Figure 4.42). This spinel oxide is protective and slow growing, with slow diffusivity of cations preventing the very fast growing iron oxides forming, and dominating the early transient oxidation stages [19]. Spallation of this Cr-rich oxide is also less likely to occur compared to iron oxides as the thermal expansion coefficient is a closer match to the substrate's [28].

Some regions of oxide were considerably thicker than the majority of the surface covered in ultra-thin scale. EDX analysis showed these regions to have a two-layer oxide forming (Figure 4.40) similar to the super 304H samples which had not been shot peened. There were also areas of the inner surface which appear to have experienced less effective shot peening where small cracks or crevices remained and the shot peening had not penetrated (Figure 4.24). These sites showed a pronounced increase in oxidation, forming large localised nodular scales, which provided further evidence that shot peening increases the oxidation resistance and reduces the likelihood of spallation.

5.2.3. 347H FG

The 347H FG samples were very similar to the super 304H samples in surface structure and grain size from SEM analysis (Figure 4.4). The mass gains were also similar at all temperatures showing a plateau after 500 hours which indicates either a protective slow growing layer forming after this time, or spallation. However, visual and SEM inspection did not show any signs of spallation on the 347H FG surface. Back scattered electron micrographs of the cross sectioned 347H FG demonstrate a degree of nodular oxide growth after 100 hours (Figure 4.25), but to a lesser extent compared to super 304H, as the oxide had already started to coalesce and form a continuous scale. Cross-sections would have to be made and then etched after a shorter duration to comment on whether the 347H FG exhibits the same uneven growth mechanism as the 304H samples, which was associated with grain boundaries.

The EDX results indicated an oxide layer similar to one formed on the super 304H steel with two subscales; an inner discontinuous Cr-rich Cr,Fe spinel and an outer surrounding Fe-oxide (Figure 4.44). The ratio of Cr to Fe in the inner layer was again greater than the martensitic steels due to a higher Cr concentration in the substrate, which will make this oxide more protective due to a lower permeability. As the discontinuous inner Cr layer grows laterally, it will form a continuous protective layer. This will reduce the overall oxide growth and help prevent further formation of fast growing Fe-oxides. However, one significant difference from the oxide formed on the super 304H was apparent; the inner oxide also contained peaks not only of Ni but also Mn, which is consistent with other reports [9]. The Ni also appears to

become concentrated in the Cr depletion zone in the substrate of several samples, due to the preferential oxidation of Cr and Fe [45].

To definitively observe the effect of the fine grained structure of the 347H FG, the standard 347H should also be studied, so that the difference can be tested. This is important as other work [24, 26] has shown grain refinement to improve oxidation resistance. This mechanism is very similar to the effect of shot peening and involves the quicker diffusion of Cr along grain boundaries. By refining the grain size, the grain boundary density will increase. The grain boundaries are denser, allowing easier movement of Cr ions, resulting in a lower activation energy for diffusion. The accelerated Cr diffusion will lead to a more protective, adherent Cr-rich oxide forming. A study by Trindade et al. [24] showed the coarse grained equivalent of the TP 347 fine grained to form non-protective Fe based oxides, which are undesirable.

6. Conclusions and Further Work

6.1. Conclusions

6.1.1. The Martensitic Steels

- The 9% Cr martensitic steels do not form Cr-rich oxide layers at 600 to 700^{o}C, making them less resistant to oxidation.
- Instead they formed Fe-rich oxides, which are more likely to spall and are non-protective.
- The T92 tube already had an as-received oxide formed on the inner surface prior to service. This Fe-rich oxide grew rapidly and spalled on cooling due to thermal stresses in the oxide induced by the large mismatch in thermal expansion coefficients of the substrate and Fe-rich oxide.
- This means the fewer cooling/heating cycles the better, in terms of spallation. This would also apply to the austenitic stainless steels and any other oxide forming alloy.

6.1.2. The Austenitic Stainless Steels

- The austenitic steels did not show any significant signs of spallation and experienced less mass gain compared to the T92 steel.
- Both the super 304H and 347H FG steels formed double-layered oxides, consisting of an inner Cr-rich spinel and an outer Fe-oxide. The Cr-rich inner subscale acts as a more protective, less permeable barrier to prevent fast growing Fe-oxide growth.
- The initial morphology of the oxide grown on the super 304H steel was composed of nodular and uneven Fe-rich oxides, which corresponded to the location of grain matrix. At the grain boundaries where Cr was diffusing fastest, protective Cr-rich islands were thought to form, inhibiting the formation of fast growing Fe-oxides.

- The beneficial effect of shot peening on oxidation was clear. The shot peened super 304H samples consistently formed significantly thinner oxides than the standard super 304H samples and showed less mass gain. The morphology of the oxides formed on the shot peened samples was also different. The oxide formed was a thin single layer that was very rich in Cr and contained little Fe. This spinel layer proved to be resistant to spallation and a very effective barrier to diffusion of cations, confirming its highly protective properties.

6.2. Further Work

- The transfer from testing in laboratory air to steam would be the main aspiration for the future work, as this would be more representative of the conditions faced in the boiler tubes in plant. The use of high pressure steam would be the most realistic testing but more difficult to execute. Steam is known to accelerate oxidation via several mechanisms and increases the risk of spallation. So, the associated results would be expected to differ and show a considerable increase in oxidation rate.

- Longer durations of testing to be more representative of the long service durations of the tubes. The longer testing durations would also then make it easier to extrapolate data such as the mass gain results.

- Possible isolation of the shot peened surface would make the mass gain representation of the shot peening effect more accurate, rather than collecting the mass gain data from both non-shot peened and shot peened surfaces all together. This may be possible by covering all the other surfaces in a protective coating, then removing after exposure, or by shot peening every surface of the sample.

- Inclusion of the standard 347H type alloy in the testing procedure would enable the fine grained 347H to be compared with its coarse grained equivalent to further observe the effect of grain size on oxidation.

- Cross-sectional and surface EDX mapping in conjunction with FIB sectioning and milling could be used as an alternative technique to measuring oxide growth in 3D as

opposed to thickness measurements. This is due to the thickness measurements being less representative due to the nodular, non-uniform oxides forming that exhibit variable coverage of the double-layered oxide. EDX mapping would help determine the growth of each individual subscale by enabling the area of each of these to be calculated.

- X-ray diffraction (XRD) techniques could also be applied to accurately determine the phase composition/crystal structure of each oxide to identify the specific oxide layer quantitatively rather than the previous EDX qualitative phase identifications.

A. Appendix

A.1. Oxidation in Water Vapour and Steam

Oxidation also occurs at high temperatures in water vapour and steam where the rate of reaction is greater than oxidation in just air [9, 17]. The morphology of the scales has also been found to differ from air oxidation. Water vapour has been shown to encourage a more porous scale to form, which is linked to an increased cation diffusion, resulting in vacancy condensation forming the pores [42]. Water vapour has also been found to reduce the plasticity of these scales, but due to controversy in the literature the exact mechanism is unclear. The reduction in plasticity would make them more prone to spallation as they cannot relieve the induced stresses [9]. Another major difference from oxidation in air is the formation of the scale hydroxides and oxyhydroxides which are more volatile than the actual oxide causing the oxide to shrink and lose its protective properties [42, 47]. Water vapour affects the oxide growth at all stages of the oxidation process such as adsorption, dissociation and diffusion. Adsorption and dissociation of the water vapour occurs on the surface of the growing oxides and results in a more permeable scale forming. The pores in the oxide structure assist the rapid inward diffusion of oxygen to form oxide at the metal-scale interface and so the pores gradually move outwards to the scale-gas interface [42]. The presence of water vapour can also affect the mechanical properties of the scale such as increasing the oxide adhesion in iron oxides and reducing it in alumina and chromia. The reduced scale adherence of alumina and chromia scales could be down to a change in growth processes or may just be down to increased scale thickness from the increased kinetics of oxidation [42]. Further understanding on steam oxidation is limited as the atmospheres produced in testing are very hard to maintain and reproduce and in-service conditions such as those in a power plant are very hard to replicate [43].

A.1.1. Water Vapour and Steam Oxidation Mechanisms

As already stated, the oxidation of alloys in steam varies significantly in both kinetics and morphology to alloy oxidation in just air or oxygen. The following mechanisms have been frequently used to explain the effect of water vapour on oxidation [43];

1. Dissociation mechanism
2. Oxidant-gas penetration mechanism
3. Formation and volatilisation of iron (II) hydroxide ($Fe(OH)_2$)
4. Formation and volatilisation of $CrO_2(OH)_2$
5. Proton dissolution induced changes in the oxide defect structure

However, any single mechanism alone cannot explain all of the observed metal oxidation behaviour in the presence of water vapour [43].

A.1.1.1. The Dissociation Mechanism

This mechanism of oxidation in steam was considered by Fujii and Meussner in 1964 [48]. Reactions occur at interfaces II and IV seen in Figure A.1, where metal ions are produced. Theses ions then diffuse to the outer interface between the oxide scale and wet atmosphere (I). Water vapour is adsorbed on the surface from the atmosphere and the resulting reactions with the metal ions produce wustite (FeO), absorbed hydrogen and defects in the oxide. Some of this hydrogen dissolves in the oxide but the majority desorbs [43].

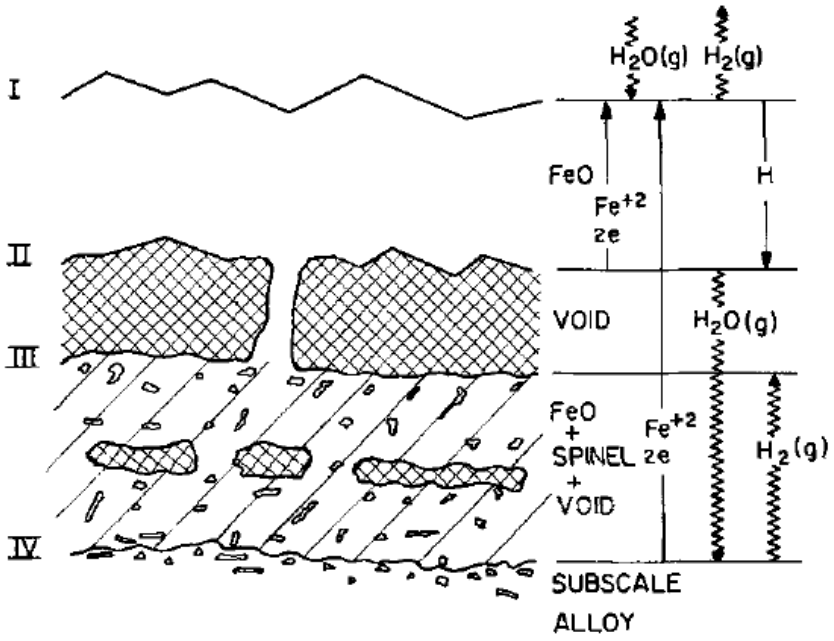

Figure A.1. The dissociation mechanism for oxidation of Fe-Cr alloys in water vapour [48].

The reactions from the adsorbed water vapour and metal ions at the oxide-atmosphere interface can be seen below

$$H_2O_{(g)} \rightarrow H_2O_{(ads)} \quad \text{(Eq. A.1)}$$

$$H_2O_{(ads)} + Fe^{2+} + 2e^- \rightarrow 'FeO' + Fe_{vac} + 2\oplus + H_{2(ads)} \quad \text{(Eq. A.2)}$$

$$H_{2(ads)} \rightarrow H_{2(g)} \quad \text{(Eq. A.3)}$$

$$H_{2(ads)} \rightarrow 2H^*_{(ox)} \quad \text{(Eq. A.4)}$$

where the symbols Fe_{vac} and $\oplus$ signify a vacant iron ion site and an electron defect respectively, and H* indicates a hydrogen atom dissolved within the oxide [48].

At interface two, the dissociation of iron oxide is thought to occur to produce an oxide ion as an absorbed species. The infusing hydrogen enables these adsorbed species to react to form the carrier gas for oxygen transport to the void [48]. This dissociation and gas formation is shown below;

$$FeO + Fe_{vac} + 2\oplus \rightarrow Fe^{2+} + O^{2-} \quad \text{(Eq. A.5)}$$

$$2H^*_{(ox)} \rightarrow H_{2(ads)} \quad \text{(Eq. A.6)}$$

$$H_{2(ads)} \rightarrow H_{2(gas)} \quad \text{(Eq. A.7)}$$

$$H_{2(ads)} + O^{2-}_{(ads)} \rightarrow H_2O_{(g)} + 2e^- \quad \text{(Eq. A.8)}$$

The resultant atmosphere and the reactions occurring at interfaces one and two cause wustite layers to form on the outer scale, Figure A.1. The wustite reacts with spinel changing the composition of the spinel phase as seen below;

$$FeCr_2O_4 + 4FeO \rightarrow 2Fe_2CrO_4 + Fe^{2+} + 2e^- \quad \text{(Eq. A.9)}$$

These observations and suggested mechanisms for the inner scale were made by Fujii and Meussner in 1964 from oxidation tests on iron-chromium alloys up to 25 wt% Cr in Ar10%H_2O at temperatures of 700-1000^oC [48]. Figure A.1 illustrates the multi-layered scale with the outer layer of wustite, a middle porous scale containing wustite and an iron chromium spinal oxide, and then an inner subscale of iron chromium spinel [43].

A.1.1.2. Oxidant-gas Penetration Mechanism

Another study compared the oxidation characteristics of iron-chromium alloys containing up to 30 wt% Cr, in dry and wet oxygen at 700^oC and 900^oC. Ikeda and Nii performed this study in 1982 [49] and found that the mass gain in wet oxygen was significantly greater than the mass gain in dry oxygen when the alloys had chromium contents of greater than 15 wt%. They compared the dissociation mechanism and the oxidant-gas penetration mechanism and showed via simple gas kinetics that the latter mechanism was more appropriate. This more appropriate mechanism involves the oxygen and water vapour passing directly to the metal surface due to the growth of microcracks and pores in the scale, assuming the cracks are numerous and large [43]. Oxidation begins with a chromia layer forming and covering the surface of the alloy. Cracks and pores in this oxide enable gas to penetrate into a void which could increase the partial pressure of oxygen within the void oxidising the iron. The produces a mixed oxide scale which is unable to prevent outward diffusion of iron ions, which enables a fast growing Fe-rich outer oxide to form [43]. Gas penetration was also found to be more common in wet oxygen conditions rather than dry, and water vapour was suggested to increase oxidation by causing more frequent scale cracking and preventing it from healing [50].

A.1.1.3. Formation and Volatilisation of $Fe(OH)_2$

An alternative mechanism for the increased oxidation of chromium steels in steam and water vapour environments was suggested by Surman and Castle in 1969 [51]. It involves the formation and volatilisation of $Fe(OH)_2$. They suggested that the rate determining process could be one of the following; 1.) the outward diffusion of iron cations to the oxide-gas interface, 2.) the inward diffusion of oxygen anions to the metal-oxide interface, or 3.) vapour-

phase diffusion of $Fe(OH)_2$ to the oxide-gas interface [43]. It was assumed that the phase boundary reactions, shown below, occur for the formation and dissociation of this volatile hydroxide. At the metal-oxide interface;

$$Fe_{(s)} + 2H_2O_{(g)} \rightarrow Fe(OH)_{2(g)} + H_{2(g)} \quad \text{(Eq. A.10)}$$

$$3Fe_{(s)} + 4H_2O_{(g)} \rightarrow Fe_3O_{4(s)} + 4H_{2(g)} \quad \text{(Eq. A.11)}$$

At the oxide-gas interface;

$$Fe(OH)_{2(g)} \rightarrow Fe_3O_{4(s)} + 2H_2O_{(g)} + H_{2(g)} \quad \text{(Eq. A.12)}$$

The experimental and theoretical values were compared for the temperature dependence of the parabolic rate constant for each of the suggested rate determining processes. The vapour model gave the closest comparison between theoretical and actual values and therefore considered as the most likely mechanism [43]. However, this iron (II) hydroxide volatilisation mechanism has caused some dispute over its validity due to similar work done on nickel and cobalt containing steels. Nickel and cobalt containing outer oxides were expected due to the volatility of these element hydroxides being close to that of iron hydroxide. However, no nickel or cobalt was found in these outer oxides [43].

A.1.1.4. Formation and Volatilisation of $CrO_2(OH)_2$

It is proposed in this mechanism that the cracking and spallation of oxide scales in water vapour is due to the evaporation of volatile chromium species mainly along the grain boundaries [43]. A study was performed on nickel-chromium alloys in air and wet air. In both conditions Ni-20Cr formed three oxides; Cr_2O_3, NiO and the spinal $NiCr_2O_4$. In air the NiO was gradually consumed in the reaction with chromia to form the spinel. In wet air the NiO remained without reacting and considerable cracking and spalling was observed. It is suggested that the oxide layer bursts because of compounds rich in chromium exerting an

over-pressure during volatilisation [43]. Compressive stresses occur when the chromia layer is continuous causing failure in the NiO and $NiCr_2O_4$ layers. The chromia layer will now be in contact with the atmosphere and volatilise to CrO_3 and $CrO_2(OH)$ which depletes the alloy of chromium and now re-oxidises as NiO and eventually spinel [43]. This process is continuous resulting in rapid oxidation. The following volatilisation reactions take place and deplete the alloy of chromium [43].

$$Cr_2O_3 + 3/2O_2 \rightarrow 2CrO_{3(g)} \quad \text{(Eq. A.13)}$$

$$Cr_2O_3 + O_2 + H_2O \rightarrow 2CrO_2(OH)_{(g)} \quad \text{(Eq. A.14)}$$

$$2CrO_3 + H_2O \rightarrow 2CrO_2(OH) + 1/2O_{2(g)} \quad \text{(Eq. A.15)}$$

A.1.1.5. Proton Dissolution Induced Changes in the Oxide Defect Structure

The presence of water vapour could also affect the defect structure and therefore properties of the oxide systems. Hydrogen from the water vapour dissolves as protons in the metal oxide. This affects such defect-dominated properties, such as diffusion-controlled transport of reactants in the oxide layer and creep [43].

A study by Galerie et al. in 2001 [52] also compared metals oxidised in air and water vapour, with the focus on the effect of major point defects and the effect that the acidity of the oxide surface had. Water vapour was again found to increases the metal oxidation when oxygen was the most mobile species in the oxide. Hydrogen solubility was also important as the metals most affected by water vapour had the greatest hydrogen solubility [52]. The rate determining process is the transport of oxygen through the scale via hydroxyl defects. In steam the oxide surface is covered in hydroxyl species but has few oxygen species. Oxygen species are formed from surface OH species which become disassociated at the O-H bond. For this to occur the surface needs acidic properties and this study has shown that pure metal species that did not have an acidic oxide had very slow oxidation rates in water vapour [43]. Therefore it has been suggested that the decomposition of OH species controls the oxidation rate. For acidic oxides

the rate of surface OH decomposition was high enough to provide oxide ions to the scale as fast as they were being used up so decomposition rate does not limit oxidation rate [43].

A.1.2. Steam Oxidation as a Function of Steel Composition and Alloy Type

The oxidation of steels and other alloys can vary a great deal depending on composition of the alloy. Increasing the chromium content of steel can improve the oxidation resistance by enabling a protective oxide scale to form. Carbon steels oxidise at high temperature to form layers of wustite, haematite and magnetite depending on the environment it is exposed to [43]. When chromium is added to the alloy, an Fe-Cr inner spinel layer is formed rather than an inner Fe-oxide layer. This occurs for ferritic (<3%Cr) and martensitic (9-12%Cr) steels. When the chromium content increases even further, such as austenitic stainless steels, an inner chromia layer is formed which is very protective against oxidation and reduces oxide growth [43]. However, the presence of water vapour slightly reduces this increased oxidation resistance effect of chromium additions. This reduction is due to the different morphology of the oxide scales produced in water vapour such as macroscopic defects like pores and cracks [43]. Studies have shown that if the chromium content is increased to 25 wt%Cr plus, then a inner chromia layer is formed at a fast rate, which slows the diffusion of iron through the scale to form magnetite at the gas-oxide interface [53]. However, it has been found that there is an upper limit for the amount of chromium additions that is favourable to oxidation resistance as the effect reaches a plateau with increasing chromium content [43].

A.1.2.1. Ferritic Steels

Low alloy ferritic steels have good tensile strength at lower temperatures (<450^{o}C), good creep strength at temperatures below 550^{o}C and outstanding weldability with no need for post heat treatment [43]. These properties make them useful for tubing alloys in pressurised applications such as boilers and heat recovery steam generators (HRSGs). They are used in the cooler regions of superheater and reheater pipes [43]. The main downfall in their material properties is the poor oxidation resistance in steam. Therefore, ferritic steels can only be used at lower temperatures reducing plant efficiency.

Steam oxidation of ferritic steels produces three oxide layers; a subscale region with internal oxide precipitates, a thick compact outer layer and a thin layer between the two [43]. Steam side oxidation of ferritic boiler tubes has produced multilayered scales on the inner piping. Scales consisting of magnetite (Fe_3O_4) and haematite (Fe_2O_3) form at temperatures below 560^{o}C. At increased temperatures wustite (FeO) is formed and when the steel is alloyed a spinel oxide will form (Fe, Cr, Mo)$_3O_4$ [43].

The flow rate of the steam is also found to affect the oxidation rate of the ferritic steels. When in contact with flowing steam a parabolic growth rate was observed at temperatures below 600^{o}C, but in stagnant steam the followed a cubic rate law [43]. The kinetics were also seen to vary with temperature. The growth rate obeys the parabolic law below 600^{o}C which show the steel is self protecting. When the temperature increases above this the scale is no longer protective as the oxidation rate turns linear [43], which is why this type of steel is not used at these temperatures. Another factor affecting the oxidation of these alloys is the method used to create the steam environment as it has been found to both increase and decrease the corrosion rate [43].

A.1.2.2. Martensitic Steels

Martensitic steels have a higher chromium content of 9-12wt% and are used in the tubing for superheaters and reheaters in fossil fuel boilers, and in the rotors and blading in steam turbines [43]. They are used in these high pressure steam applications in temperatures up to 620^{o}C and pressures and pressures up to 300 bar. The oxide morphology has been studied revealing an Fe-rich outer layer with an inner layer made up of Cr, Mo, Fe oxides [43].

Studies have also looked at the affect of the different alloying elements in martensitic steels have on oxidation resistance in steam [54]. 9wt%Cr steels were tested at 600^{o}C and 650^{o}C and Si additions were found to increase the resistance to steam oxidation dramatically, with further increases observed when trace amounts of Ti and Y (0.05wt%) were added. However, the silicon also caused an increase in carbide agglomeration which is undesirable [54]. The increased silicon content enables SiO_2 to form at the metal-oxide interface as an internal oxide

or continuous layer. This oxide prevents the diffusion of chromium ions which delays the onset of breakaway oxidation [43]. Sulphur is also thought to reduce the oxidation rate of these steels due the diffusion of sulphur ahead of the oxide-substrate interface becoming a rate limiting stage in the oxidation kinetics. But there is an increased risk of scale spallation with high sulphur contents during thermal cycling [43]. Small additions of Ni (<1wt%) have a detrimental effect on oxidation resistance but improve yield strength and toughness.

A.1.2.3. Austenitic Steels

The austenitic steels are more expensive than the steels just mentioned due to the increased alloying additions. They have poor thermal conductivity and larger thermal expansion coefficients which restricts their applications, and so they are mainly used in the hotter sections of the superheater and reheater tubes in the boiler [43]. Fatigue cracking can result from high thermal stresses and oxide scale spallation can occur due to their thermal expansion coefficients. They are also used to in areas where corrosion is problem to repair and provide protection for low alloy steels. The increased chromium in the matrix provides enhanced oxidation/corrosion resistance [43].

These steels have higher chromium contents which exhibit lower parabolic rate constants [43]. The calculations were made assuming that Cr_2O_3, Fe_3O_4 and FeO were all formed and then this theoretical data was compared with the actual experimental values. Environments with increased pressure cause increased oxidation rates as the reliability of the oxide is reduced due to voids and cavities forming. Similar to martensitic alloys, increased Si content enhances oxidation resistance by forming an inner silica layer which has a slow growth rate and reduces chromium diffusion and therefore chromium depletion in the substrate [43].

The influence of grain size of the steam oxidation of austenitic steels has also been investigated. Fine grained steels have enhanced oxidation resistance over the equivalent course grained steels. As stated previously, this effect is down to the faster diffusion of chromium ions along the grain boundaries to the surface which reduces local depletion below the scale [43].

A.2. Oxide Thickness Measurements

Tables A.1, A.2, and A.3 show the average inner surface oxide thickness measurements for each sample, with standard deviations. Some samples of the shot peened super 304H had no measurements recorded due to no visible oxide forming on the inner surface after those durations.

Table A.1. The average oxide thickness measurements (in μm) for the inner surface of the austenitic stainless steels after selected durations at 600^{o}C exposure.

	100h	250h	500h	1000h
Super 304H	3.12 ±2.66	2.25 ±2.13	4.03 ±3.39	6.87 ±3.59
Shot peened super 304H	-	-	-	-
347H FG	7.22 ±3.46	5.95 ±4.30	9.62 ±5.69	11.26 ±5.63

Table A.2. The average oxide thickness measurements (in μm) for the inner surface of the austenitic stainless steels after selected durations at 650^{o}C exposure.

	100h	250h	500h	1000h
Super 304H	5.46 ±3.08	7.93 ±2.53	7.89 ±3.22	9.09 ±3.20
Shot peened super 304H	-	-	-	0.28 ±0.20
347H FG	5.50 ±2.98	9.33 ±2.48	5.76 ±2.17	7.59 ±2.38

Table A.3. The average oxide thickness measurements (in μm) for the inner surface of the austenitic stainless steels after selected durations at 700^{o}C exposure.

	100h	250h	500h	1000h
Super 304H	8.02 ±2.21	7.46 ±2.70	7.73 ±2.92	9.09 ±3.54
Shot peened super 304H	-	-	1.00 ±0.57	0.96 ±0.57
347H FG	5.64 ±1.89	6.13 ±1.40	6.15 ±1.60	6.43 ±1.89

References

1. Osgerby, S. *Materials R&D Requirements for Fossil Fuelled Steam Plant*. in *Energy Materials – Meeting the Challenge*. 2008. Loughborough, UK.
2. Viswanathan, R. and W. Bakker, *Materials for ultrasupercritical coal power plants-boiler materials: Part 1.* Journal of Materials Engineering and Performance, 2001. **10**(1): p. 81-95.
3. Ehlers, J., D.J. Young, E.J. Smaardijk, A.K. Tyagi, H.J. Penkalla, L. Singheiser, and W.J. Quadakkers, *Enhanced oxidation of the 9%Cr steel P91 in water vapour containing environments.* Corrosion Science, 2006. **48**(11): p. 3428-3454.
4. Powell, C.A. and B.D. Morreale, *Materials challenges in advanced coal conversion technologies.* Mrs Bulletin, 2008. **33**(4): p. 309-315.
5. Viswanathan, R., J.F. Henry, J. Tanzosh, G. Stanko, J. Shingledecker, B. Vitalis, and R. Purgert, *US program on materials technology for ultra-supercritical coal power plants.* Journal of Materials Engineering and Performance, 2005. **14**(3): p. 281-292.
6. Asbury, F.E. and S. Brooks. *Superheater Tubes for Advanced Coal-fired Power Plant in the UK*. in *Proceedings of an International Conference on Advances in Material Technology for Fossil Power Plants*. 1987. Chicago, Illinois, USA: ASM International.
7. (ed.)), B.E.S.A.C.J.W. *Technology and Applied R&D Needs for Materials under Extreme Environments*. in *Proceedings of Basic Research Needs to Assure a Secure Energy Future*. 2007.
8. Rehn, I.M. *Long-Term Performance of Chromate-Treated Superheater and Reheater Tubes*. in *Proceedings of an International Conference on Advances in Material Technology for Fossil Power Plants*. 1987. Chicago, Illanois, USA: ASM International.
9. Sedriks, A.J., *Corrosion of Stainless Steels*. 2nd ed. 1996, Canada: John Wiley and Sons, Inc.
10. Osgerby, S. *Oxide scale damage and spallation in P92 martensitic steel*. in *4th International Conference on the Microscopy of Oxidation*. 1999. Cambridge, England: Science & Technology Letters.
11. Weizhong, F., *Comprehensive Prevention of Steam-Side Scaling and Solid Particle Erosion of Ultra Supercritical Unit*, in *Proceedings of Supercritical Coal: Operating Experience and Technology Developments, I Mech E*. 2007.
12. Honeycombe, R.W.K., *Steels - Microstructure and Properties*. 1981, London: Edward Arnold (Publishers) Ltd.
13. Klueh, R.L., *Elevated temperature ferritic and martensitic steels and their application to future nuclear reactors.* International Materials Reviews, 2005. **50**(5): p. 287-310.
14. Mannesmann, S., *DMV 304 HCu, Boiler Grade DMV 304 HCu*, in *Salzgitter Mannesmann Stainless Tubes*.
15. Lepingle, V., G. Louis, D. Allue, B. Lefebvre, and B. Vandenberghe, *Steam oxidation resistance of new 12%Cr steels: Comparison with some other ferritic steels.* Corrosion Science, 2008. **50**(4): p. 1011-1019.
16. Schaffer, J.P., A. Saxena, S.D. Antolovich, T.H. Sanders, and S.B. Warner, *The Science and Design of Engineering Materials*. 1995, United States of America: Richard D. Irwin, Inc.
17. West, J.M., *Basic Corrosion and Oxidation*. 2nd ed. 1986, Chichester: Ellis Horwood Limited.
18. Young, D., *High Temperature Oxidation and Corrosion of Metals*. 1st ed. 2008, Oxford: Elsevier Ltd.
19. Stott, F.H., G.C. Wood, and J. Stringer, *THE INFLUENCE OF ALLOYING ELEMENTS ON THE DEVELOPMENT AND MAINTENANCE OF PROTECTIVE SCALES.* Oxidation of Metals, 1995. **44**(1-2): p. 113-145.
20. Hussey, R.J., D.F. Mitchell, and M.J. Graham, *THE GROWTH AND STRUCTURE OF OXIDE-FILMS FORMED ON SINGLE-CRYSTAL (100) AND POLYCRYSTALLINE CR BETWEEN 550 AND 900-DEGREES-C.* Werkstoffe Und Korrosion-Materials and Corrosion, 1987. **38**(10): p. 575-583.

21. Zurek, J., L.N. Hierro, J. Piron-Abellan, L. Niewolak, L. Singheiser, W.J. Quadakkers, and p. trans tech. *Effect of alloying additions in ferritic 9-12%Cr steels on the temperature dependence of the steam oxidation resistance*. in *6th International Symposium on High Temperature Corrosion and Protection of Materials*. 2004. Les Embiez, FRANCE: Trans Tech Publications Ltd.
22. Gray, S., K. Berriche-Bouhanek, H.E. Evans, and p. trans tech. *Oxide growth stresses in an austenitic stainless steel determined by creep extension*. in *6th International Symposium on High Temperature Corrosion and Protection of Materials*. 2004. Les Embiez, FRANCE: Trans Tech Publications Ltd.
23. Francis, J.M., *INFLUENCE OF MINOR ALLOYING ELEMENTS ON STRUCTURE OF SURFACE OXIDES FORMED DURING HIGH-TEMPERATURE OXIDATION OF AN AUSTENITIC STEEL.* Journal of the Iron and Steel Institute, 1966. **204**: p. 910-&.
24. Trindade, V.B., U. Krupp, P.E.G. Wagenhuber, and H.J. Christ. *Oxidation mechanisms of Cr-containing steels and Ni-base alloys at high-temperatures - Part I: The different role of alloy grain boundaries*. in *Workshop on Novel Approaches to the Improvement of High Temperature Corrosion Resistance*. 2004. Frankfurt, GERMANY: Wiley-V C H Verlag Gmbh.
25. Huntz, A.M., S.C. Tsai, J. Balmain, K. Messaoudi, B. Lesage, and C. Dolin. *Atomic transport in Cr2O3 and Al2O3 scales: Growth mechanism and effect of yttrium*. in *4th International Symposium on High Temperature Corrosion and Protection of Materials*. 1996. Les Embiez, France: Transtec Publications Ltd.
26. Peng, X., J. Yan, Y. Zhou, and F. Wang, *Effect of grain refinement on the resistance of 304 stainless steel to breakaway oxidation in wet air.* Acta Materialia, 2005. **53**(19): p. 5079-5088.
27. Piehl, C., Z. Toekei, and H.J. Grabke. *Influence of chromium diffusion and different surface finishes on the oxidation behaviour of chromium steels*. in *4th International Conference on the Microscopy of Oxidation*. 1999. Cambridge, England: Science & Technology Letters.
28. Tan, L., X. Ren, K. Sridharan, and T.R. Allen, *Effect of shot-peening on the oxidation of alloy 800H exposed to supercritical water and cyclic oxidation.* Corrosion Science, 2008. **50**(7): p. 2040-2046.
29. Grabke, H.J., W. Auer, M.J. Bennett, F. Bregani, F. Gesmundo, D.J. Hall, D.B. Meadowcroft, S. Mrowec, J.F. Norton, W.J. Quadakkers, S.R.J. Saunders, and Z. Zurek, *POINTS TO BE CONSIDERED IN THERMOGRAVIMETRY.* Werkstoffe Und Korrosion-Materials and Corrosion, 1993. **44**(8): p. 345-350.
30. Kofstad, P., *High-Temperature Oxidation Of Metals*. 1966, New York: John Wiley and Sons, Inc.
31. Birks , N., G.H. Meier, and F.S. Pettit, *Introduction To The High-Temperature Oxidation of Metals*. 2nd ed. 2006, New York: Cambridge University Press.
32. Sarrazin, P., A. Galerie, and J. Fouletier, *Mechanisms Of High Temperature Corrosion: A Kinetic Approach*. 2008, Switzerland: Trans Tech Publications Ltd.
33. Gaskell, D.R., *Introduction To The Thermodynamics Of Materials* 4th ed. 2003, London: Taylor & Francis Books, Inc.
34. Osgerby, S. *Development of de-alloyed zones during oxidation: effects on microstructure and spallation behaviour*. in *Conference on Quantitative Microscopy of High Temperature Materials*. 1999. Sheffield, England: I O M Communications Ltd Inst Materials.
35. Vossen, J.P.T., P. Gawenda, K. Rahts, M. Rohrig, M. Schorr, and M. Schutze, *Limits of the oxidation resistance of several heat-resistant steels under isothermal and cyclic oxidation as well as under creep in air at 650 degrees C.* Materials at High Temperatures, 1997. **14**(4): p. 387-401.
36. Stringer, J., *STRESS GENERATION AND RELIEF IN GROWING OXIDE FILMS.* Corrosion Science, 1970. **10**(7): p. 513-&.

37. Stott, F.H. and A. Atkinson. *THE MODELING OF GROWTH STRESSES DURING HIGH-TEMPERATURE OXIDATION*. in *Workshop on Mechanical Properties of Protective Oxide Scales*. 1994. Teddington, England: Butterworth-Heinemann Ltd.
38. Hancock, P. and R.C. Hurst, *Advances in Corrosion Science and Technology*, ed. R.W. Staehle and M.G. Fontana. Vol. 4. 1974, New York: Plenum Press
39. Oxx, G.D., Prod. Eng, 1958. **29**: p. 61-70.
40. Evans, H.E. and R.C. Lobb, *CONDITIONS FOR THE INITIATION OF OXIDE SCALE CRACKING AND SPALLATION.* Corrosion Science, 1984. **24**(3): p. 209-222.
41. Schutze, M., *MECHANICAL-PROPERTIES OF OXIDE SCALES.* Oxidation of Metals, 1995. **44**(1-2): p. 29-61.
42. Saunders, S.R.J., M. Monteiro, and F. Rizzo, *The oxidation behaviour of metals and alloys at high temperatures in atmospheres containing water vapour: A review.* Progress in Materials Science, 2008. **53**(5): p. 775-837.
43. Fry, A., S. Osgerby, and M. Wright, *Oxidation of Alloys in Steam Environments – A Review*, in *NPL Report MATC(A)90*. 2002.
44. Calvarin, G., A.M. Huntz, and R. Molins. *Oxidation mechanism of Ni-20Cr thin strips and effect of a mechanical loading*. in *4th International Conference on the Microscopy of Oxidation*. 1999. Cambridge, England: Science & Technology Letters.
45. Garrett, J.C.P., S.K. Lister, P.J. Nolan, and J.T. Crook. *Some Factors in the Oxidation of Austenitic Stainless Steels*. in *Corrosion of Steels in CO2, Proceedings of the British Nuclear Energy Society International Conference*. 1974. Reading University: The British Nuclear Energy Society.
46. Tao, N.R., Z.B. Wang, W.P. Tong, M.L. Sui, J. Lu, and K. Lu, *An investigation of surface nanocrystallization mechanism in Fe induced by surface mechanical attrition treatment.* Acta Materialia, 2002. **50**(18): p. 4603-4616.
47. Opila, E.J. and p. trans tech. *Volatility of common protective oxides in high-temperature water vapor: Current understanding and unanswered questions*. in *6th International Symposium on High Temperature Corrosion and Protection of Materials*. 2004. Les Embiez, FRANCE: Trans Tech Publications Ltd.
48. Fujii, C.T. and R.A. Meussner, *THE MECHANISM OF THE HIGH-TEMPERATURE OXIDATION OF IRON-CHROMIUM ALLOYS IN WATER VAPOR.* Journal of the Electrochemical Society, 1964. **111**(11): p. 1215-1221.
49. Ikeda, Y. and K. Nii, *MECHANISM OF ACCELERATED OXIDATION OF FE-CR ALLOYS IN WATER-VAPOR CONTAINING ATMOSPHERE.* Transactions of National Research Institute for Metals, 1984. **26**(1): p. 52-62.
50. Ikeda, Y. and K. Nii, *MICROCRACK GENERATION AND ITS HEALING IN THE OXIDE SCALE FORMED ON FE-CR ALLOYS.* Oxidation of Metals, 1978. **12**(6): p. 487-502.
51. Surman, P.L. and J.E. Castle, *GAS PHASE TRANSPORT IN OXIDATION OF FE AND STEEL.* Corrosion Science, 1969. **9**(10): p. 771-&.
52. Galerie, A., Y. Wouters, and M. Caillet. *The kinetic behaviour of metals in water vapour at high temperatures: Can general rules be proposed?* in *5th International Symposium on High Temperature Corrosion and Protection of Materials*. 2000. Les Embiez, France.
53. Otsuka, N. and H. Fujikawa, *SCALING OF AUSTENITIC STAINLESS-STEELS AND NICKEL-BASE ALLOYS IN HIGH-TEMPERATURE STEAM AT 973-K.* Corrosion, 1991. **47**(4): p. 240-248.
54. Abe, F., M. Igarashi, S. Wanikawa, M. Tabuchi, T. Itagaki, K. Kamura, and K. Yamaguchi. *R & D of advanced Ferritic steels of 650^{o}C USC Boilers*. in *Proceedings of the 5th International Charles Parsons Turbine Conference* 2000.